CP violation measurements using $B^{\pm} \to DK^{*\pm}$ decays at LHCb

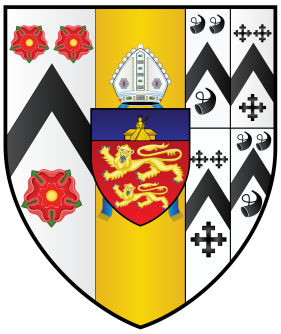

Anita K Nandi

Brasenose College

University of Oxford

A thesis submitted for the degree of

Doctor of Philosophy

Trinity 2018

Acknowledgements

There are many people that I would like to thank for a rewarding and enjoyable DPhil.

First and foremost, my thanks go to my supervisors Sneha Malde and Neville Harnew. Sneha for her guidance and support throughout the DPhil and teaching me so much about both physics and life. I thank Neville for being there for advice whenever I needed it. I would also like to thank Malcolm John, for his enthusiasm and encouragement throughout my DPhil.

My thanks go to my many fellow Oxford LHCb students throughout the years, for their helpful discussions, office companionship and willingness to answer my many questions. Also, I would also like to thank my friends and colleagues both in Oxford and CERN for the many and varied stimulating, and often downright strange, discussions.

I am very grateful to have had the continued support of my friends and family throughout the last three and a half years. Especially my parents, whose wise words never fail to put things in perspective, and Jacob, who has been there throughout my whole DPhil, making me laugh and keeping me sane. I would also like to thank those people who made the change from Cambridge to Oxford; their friendship and support, as well as the many dinners, pub trips and tea sessions, has made my time in Oxford an extremely happy one.

I would like to extend my gratitude to the Science and Technology Facilities Council (STFC) for providing my funding, as well as Brasenose College; the people, formal dinners and second desserts have helped to make my time at Oxford more enjoyable.

CP violation measurements using $B^{\pm} \to DK^{*\pm}$ decays at LHCb

Anita K Nandi

Brasenose College, University of Oxford

A thesis submitted for the degree of Doctor of Philosophy

Trinity 2018

Abstract

Measurements of *CP* violation in $B^- \to DK^{*-}$ decays, including the sensitivity to the CKM angle γ, are presented in this thesis. Decays of the D^0 meson to $K^-\pi^+$, K^-K^+, $\pi^-\pi^+$, π^-K^+, $K^-\pi^+\pi^-\pi^+$, $\pi^-\pi^+\pi^-\pi^+$, and $\pi^-K^+\pi^-\pi^+$ are investigated. Observables are measured that are sensitive to the CKM angle γ and the hadronic parameters of the decay r_B and δ_B. These measurements are performed using proton-proton collision data collected by the Large Hadron Collider beauty (LHCb) experiment from 2011 to 2016. These data correspond to the largest yields observed in these modes. The world's first *CP* violation measurements in four-body D^0 decay modes using the $B^- \to DK^{*-}$ channel are presented. The first evidence of the $B^- \to DK^{*-}$ mode, where the D^0 decays to π^-K^+, is also obtained with a signal significance of 4.2σ. A value of $\gamma = 40.9^\circ$ is measured with a 1σ confidence interval of $[25, 58]^\circ$, and 2σ confidence intervals of $[10, 87]^\circ$ and $[97, 167]^\circ$, which is consistent with the world average measurement of γ. The world's most precise value of $r_B = 0.113^{+0.017}_{-0.019}$ for $B^- \to DK^{*-}$ decays is measured.

Contents

x

1 Introduction

The field of particle physics has arisen from curiosity and desire to understand the world around us. Throughout the last century a greater understanding of the most fundamental particles that constitute matter and the interactions between them has been developed, which has culminated in the Standard Model (SM) of particle physics. This elegant and well-tested model represents our current best understanding of the Universe.

CP violation enters the SM through a single phase in the CKM quark mixing matrix. The unitarity constraints of this matrix can be graphically represented by a triangle in the complex plane. One of the angles in this triangle, conventionally labelled γ, is a very useful parameterisation of *CP* violation, due to the fact that it can be measured in purely tree-level processes. While processes that contain loops are expected to have sensitivity to physics beyond the SM, a tree-level measurement acts as a SM "benchmark". Therefore, by comparing tree-level SM measurements of γ to indirect, loop-level measurements, any deviation observed indicates new physics. Hence the uncertainties on direct measurements of γ must be minimised in order to make such comparisons meaningful.

This thesis investigates *CP* violation in $B^- \to DK^{*-}$ decays, where D is a superposition of D^0 and $\overline{D}^0$ decaying to two- and four-body final states containing charged pions and kaons. The sensitivity of these decays to the CKM angle γ is

studied. The measurement involves isolating the $B^- \to DK^{*-}$ families of decays before measuring various observables relating to the yields, which are sensitive to *CP* violation. Information on the CKM angle γ is extracted, along with other hadronic parameters of the decay.

The data used in this thesis are collected by the LHCb detector, located at the CERN Large Hadron Collider (LHC). The experiment specialises in *CP* violation measurements of b and c hadrons. In total the data used in this thesis consists of 1 fb^{-1} and 2 fb^{-1} of proton-proton collisions at $\sqrt{s} = 7$ TeV and 8 TeV collected in 2011 and 2012 respectively, and 1.8 fb^{-1} at $\sqrt{s} = 13$ TeV collected in 2015 and 2016.

Chapter 2 covers the background theory behind *CP* violation in the Standard Model. The unitarity triangle and CKM angle γ are discussed, followed by the methods to extract *CP* violation measurements from $B^- \to DK^{*-}$ decays. Previous γ measurements using these decays are also summarised.

In Chapter 3 an overview of the LHCb detector is presented, covering each of the sub-detectors: VELO, tracking systems, dipole magnet, RICH sub-detectors, electromagnetic and hadronic calorimeters and muon system. This chapter also introduces the trigger system and reconstruction, as well as discussing the process of creating simulated event samples in the LHCb detector.

The original research performed by the author is primarily documented in Chapters 4 - 6. Chapter 4 presents a discussion of the selection requirements of the analysis including reconstruction, particle identification, reducing so-called peaking backgrounds and the multivariate analysis techniques used. This chapter also presents the mass parameterisation of the favoured modes, covering the shapes of each model component, before revealing the full mass fits.

Chapter 5 covers the simultaneous fit that is used to extract the *CP* observables. The setup of the simultaneous fit is discussed in detail, before moving onto the results obtained from the fit and the systematic uncertainties. Finally, the results are interpreted in terms of the parameters of interest, r_B, δ_B and γ, in Chapter 6, where r_B and δ_B are the hadronic parameters of the B^--meson decay. Here the external inputs used in the interpretation are discussed, before providing results on

the sensitivity to r_B, δ_B and γ in the $B^- \to DK^{*-}$ decay channel. Additionally, the expected future sensitivity to these parameters in $B^- \to DK^{*-}$ decays is discussed.

The work presented in this thesis was published in a single article in the *Journal of High Energy Physics* **11** (2017) 156 [1].

2

CP violation and measurements of CKM angle γ

2.1 The Standard Model

The Standard Model (SM) of particle physics describes all known fundamental particles and their interactions. Its predictions have been rigorously tested over several decades and have been found to be consistent with our observations to remarkable levels of precision [2]. Although the SM has proven to be extremely accurate it has several limitations, for example the model does not incorporate gravitational interactions, provide a dark matter candidate, or explain the huge asymmetry observed between matter and antimatter. These problems suggest that the SM is an incomplete theory, hence experimental particle physics is driven by the search for direct or indirect signs of New Physics.

The SM contains twelve spin-1/2 fermions in three generations, which are grouped into quarks and leptons, listed in Table 2.1. All these elementary particles have corresponding antiparticles. The fermions interact via the electromagnetic, weak and strong forces, which are mediated by gauge bosons listed in Table 2.2. The Higgs boson (H), which is not a gauge boson, is the only elementary scalar particle, and it couples to all particles with mass. The Higgs mechanism explains why weak gauge bosons have mass, while the photon is massless.

	Quarks		Leptons	
	Flavour	Charge	Flavour	Charge
First generation	up (u)	$+2/3$	electron (e)	-1
	down (d)	$-1/3$	electron neutrino (ν_e)	0
Second generation	charm (c)	$+2/3$	muon (μ)	-1
	strange (s)	$-1/3$	muon neutrino (ν_μ)	0
Third generation	top (t)	$+2/3$	tau (τ)	-1
	bottom (b)	$-1/3$	tau neutrino (ν_τ)	0

Table 2.1: Quarks and leptons in the Standard Model.

Gauge boson	Force	Charge
photon (γ)	Electromagnetic	0
Z	Weak	0
$W^\pm$	Weak	±1
gluon (g)	Strong	0
H (scalar)	-	0

Table 2.2: Gauge and Higgs bosons in the Standard Model.

Quarks do not exist as free particles, but always exist in bound states with other quarks, referred to as hadrons. There are different types of hadrons: most commonly mesons and baryons, in addition to the recently discovered pentaquarks and tetraquarks [3–5]. Mesons are two-particle bound states composed of a quark and an antiquark, and baryons are three-particle bound states composed of three quarks. Examples of mesons include B mesons, containing a b or $\overline{b}$ quark (*e.g.* B^-, B^+, B^0), and D mesons, containing a c or $\overline{c}$ quark (*e.g.* D^-, D^+, D^0). Examples of baryons include protons, which are composed of uud quarks, and Λ baryons, which are composed of uds quarks. Tetraquarks consist of two quarks and two antiquarks, and pentaquarks consist of four quarks and one antiquark.

2.2 *CP* violation

One of the key problems with the SM is that it does not explain why our universe consists almost entirely of matter, with hardly any antimatter present. This asymmetry is commonly quantified by the baryon-antibaryon asymmetry, $\frac{n_B - n_{\bar{B}}}{n_\gamma} \approx \frac{n_B}{n_\gamma}$, where n_B, $n_{\bar{B}}$ and n_γ are the baryon, anti-baryon and photon number densities respectively. Astrophysical observations have measured the baryon-antibaryon

asymmetry to be of the order of 10^{-10} [6]. The requirements for this asymmetry to be generated from a symmetrical initial state, known as baryogenesis, were first proposed by Andrei Sakharov in 1967 [7]. The three Sakharov conditions are: baryon number violation, the violation of charge (C) symmetry and charge-parity (CP) symmetry, and departure from thermal equilibrium. These components are required in all baryogenesis models. The definitions of the C and P symmetries are given by their operators:

- The charge conjugation operator, $\hat{C}$, converts particles into their antiparticles,
- The parity operator, $\hat{P}$, reverses the spatial axes so all vectors change sign.

CP symmetry is violated if the system changes under the combined $\hat{C}\hat{P}$ transformation.

The SM satisfies the CP violation condition for baryogenesis, however the amount of asymmetry that can be generated from CP violation in the SM is many orders of magnitude smaller than the asymmetry observed from astrophysical observations [8]. New Physics models that can introduce new sources of CP violation [9], such as supersymmetric models, can be developed by theorists and tested at the LHC and other experiments. However, it is also necessary to make precise measurements of CP violation in the SM to improve our understanding of matter-antimatter asymmetry and search for indirect signs of New Physics.

CP violation is probed using many different processes. The different types of CP violation in the SM can be split into three categories:

- **Direct CP violation in decay**: this is when the rate of decay of a particle is not equal to the rate of the decay of the corresponding antiparticle *e.g.*

$$\Gamma\left(B^- \to DK^-\right) \neq \Gamma\left(B^+ \to DK^+\right) \ ,$$

  where D represents a superposition of D^0 and $\overline{D}^0$ mesons.

- **Indirect *CP* violation in mixing**: Neutral mesons can oscillate between their particle and antiparticle states, $B^0 \leftrightarrow \overline{B}^0$, as shown in Fig. 2.1. Indirect *CP* violation occurs when $B^0 \to \overline{B}^0$ and $\overline{B}^0 \to B^0$ proceed at different rates, *e.g.*

$$\Gamma\left(B^0 \to \overline{B}^0 \to X\right) \neq \Gamma\left(\overline{B}^0 \to B^0 \to \bar{X}\right) \ ,$$

where X is some measured final state accessible to both B^0 and $\overline{B}^0$.

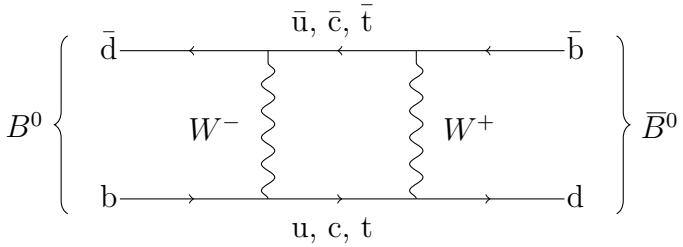

Figure 2.1: Feynman diagram of mixing between B^0 and $\overline{B}^0$.

- ***CP* violation from the interference of mixing and decay**: This is best illustrated by an example. A B_s^0 meson (containing a b quark and s antiquark) can decay to a $D_s^- K^+$ or $D_s^+ K^-$ final state. However, this process can also proceed via $B_s^0 \to \overline{B}_s^0$ mixing, where the $\overline{B}_s^0$ decays to $D_s^- K^+$ or $D_s^+ K^-$. These decay paths to the same final state interfere with each other, which results in the third form of *CP* violation, illustrated by

$$\Gamma\left(B_s^0 \to D_s^- K^+\right) \neq \Gamma\left(B_s^0 \to \overline{B}_s^0 \to D_s^- K^+\right)$$

Each of these three types of *CP* violation can be investigated. This thesis focuses on measurements of direct *CP* violation within the Standard Model.

2.3 The CKM matrix

Quarks in the Standard Model can interact via the strong, weak or electromagnetic interactions. The weak interaction couples to a rotation of the flavour eigenstates. Therefore, the eigenstates that take part in the weak interaction (weak eigenstates) are a mixture of the flavour eigenstates that hadronise to produce the observable

meson states. The Cabibbo-Kobayashi-Maskawa (CKM) matrix, V_{CKM}, given in Eq. 2.1, describes the relationship between the weak eigenstates (d', s', b') and flavour eigenstates (d, s, b) of the quarks.

$$\begin{pmatrix} d' \\ s' \\ b' \end{pmatrix} = \begin{pmatrix} V_{ud} & V_{us} & V_{ub} \\ V_{cd} & V_{cs} & V_{cb} \\ V_{td} & V_{ts} & V_{tb} \end{pmatrix} \begin{pmatrix} d \\ s \\ b \end{pmatrix} = V_{CKM} \begin{pmatrix} d \\ s \\ b \end{pmatrix} \tag{2.1}$$

A given element of this matrix, V_{ij}, defines the coupling of a $j \to i$ quark transition. Similarly V_{ij}^* defines the coupling of a $\bar{j} \to \bar{i}$ antiquark transition. By definition the CKM matrix is unitary, i.e. $V_{CKM}V_{CKM}^* = \mathbb{1}$, assuming there are only three generations of quarks. The CKM matrix is a complex 3×3 matrix, which yields 18 parameters. The unitarity requirement, corresponding to nine complex equations, reduces the number of free parameters, and five strong phases can be absorbed into the quark fields as they are not physically observable. This leaves four independent free parameters to describe the CKM matrix: three amplitudes and one phase. This free phase parameter is the source of *CP* violation in the SM.

A standard representation of the CKM matrix uses 3 angles, θ_{12}, θ_{23} and θ_{13}, and one *CP* violating phase, δ, as shown in Eq. 2.2. These angles are defined and labelled in a way which relates to the mixing of two specific generations; couplings between the quark generation i and j vanish if $\theta_{ij} = 0$, and s_{ij} and c_{ij} represent $\sin\theta_{ij}$ and $\cos\theta_{ij}$ respectively.

$$V_{CKM} = \begin{pmatrix} 1 & 0 & 0 \\ 0 & c_{23} & s_{23} \\ 0 & -s_{23} & c_{23} \end{pmatrix} \begin{pmatrix} c_{13} & 0 & s_{13}e^{-i\delta_{13}} \\ 0 & 1 & 0 \\ -s_{13}e^{i\delta_{13}} & 0 & c_{13} \end{pmatrix} \begin{pmatrix} c_{12} & s_{12} & 0 \\ -s_{12} & c_{12} & 0 \\ 0 & 0 & 1 \end{pmatrix} \tag{2.2}$$

If the CKM matrix was equivalent to the identity matrix there would be no cross-generation weak interaction of the quarks *e.g.* a u quark transition mediated by a W boson could only result in a d, not a s or b quark. From empirical determination, the magnitude of the elements in the CKM matrix are [10]:

$$|V_{CKM}| = \begin{pmatrix} 0.97434^{+0.00011}_{0.00012} & 0.22506 \pm 0.00050 & 0.00357 \pm 0.00015 \\ 0.22492 \pm 0.00050 & 0.97351 \pm 0.00013 & 0.0411 \pm 0.0013 \\ 0.00875^{+0.00032}_{-0.00033} & 0.0403 \pm 0.0013 & 0.99915 \pm 0.00005 \end{pmatrix} . \tag{2.3}$$

It can be seen that quark transitions within the same generation are highly favoured; these are known as Cabibbo-favoured decays. Quark transitions across

one generation are suppressed, and the suppression is even stronger across two generations. These are known as Cabibbo-suppressed transitions.

The structure in the CKM matrix can be illustrated by the Wolfenstein parameterisation, given in Eq. 2.4, which uses parameters A, λ, ρ and η.

$$V_{CKM} = \begin{pmatrix} 1-\lambda^2/2 & \lambda & A\lambda^3(\rho - i\eta) \\ -\lambda & 1-\lambda^2/2 & A\lambda^2 \\ A\lambda^3(1-\rho-i\eta) & -A\lambda^2 & 1 \end{pmatrix} . \tag{2.4}$$

This is an approximation of the standard parameterisation given in Eq. 2.2, expanded in powers of the relatively small parameter $\lambda = \sin\theta_{12} = 0.22$. The other parameters are defined by $A\lambda^2 = s_{23}$ and $A\lambda^3(\rho - i\eta) = s_{13}e^{-i\delta}$. The *CP* violation can be determined by measuring $\rho - i\eta$.

2.4 The CKM unitarity triangle

Verifying the unitarity of the CKM matrix is of the utmost importance since non-unitarity is a clear sign of physics Beyond the Standard Model [11]. The unitarity of the CKM matrix leads to nine unitarity conditions, for example $V_{ud}V_{ub}^* + V_{cd}V_{cb}^* + V_{td}V_{tb}^* = 0$, which is the most readily applicable to B physics. These relations can be represented as a triangle in the complex plane, as shown in Fig. 2.2. The triangle representing the condition $V_{ud}V_{ub}^* + V_{cd}V_{cb}^* + V_{td}V_{tb}^* = 0$ is the most interesting as all the quantities are experimentally measurable and are of reasonable relative size. The angles are defined as α, β and γ, and the area of the triangle is proportional to the amount of *CP* violation in the quark sector of the SM [11].

The values of α, β and γ can be accessed by looking at various B meson decays. The current best measurements for these values are $\alpha = \left(87.6^{+3.5}_{-3.3}\right)^\circ$, $\beta = 21.85^{+0.68}_{-0.67}$ and $\gamma = \left(72.2^{+6.8}_{-7.3}\right)^\circ$ [10, 12]. Overconstraining this unitarity triangle allows verification as to whether or not the triangle closes, i.e. whether it truly is a triangle. Obtaining inconsistent results from overconstraining would suggest that the CKM matrix is not unitary, which would be incompatible with the SM.

The CKM angle $\gamma \equiv \arg\left(-\frac{V_{ud}V_{ub}^*}{V_{cd}V_{cb}^*}\right)$ is the angle with the largest uncertainty. This angle is measured using the LHCb detector from the rates of charged and

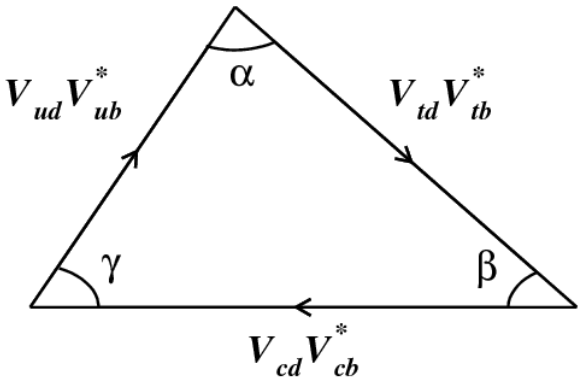

Figure 2.2: Graphical representation, in the complex plane, of the unitarity condition $V_{ud}V_{ub}^* + V_{cd}V_{cb}^* + V_{td}V_{tb}^* = 0$, forming the CKM triangle with angles α, β and γ.

neutral B decays to a D meson (reconstructed in one of a variety of final states) and kaons or pions. These are known as direct measurements. In order to obtain the most precise direct measurement of γ, the individual measurements from each of these γ-sensitive decays are combined to produce a single value with a lower uncertainty. The latest published LHCb combination is $\gamma = \left(72.2^{+6.8}_{-7.3}\right)^\circ$ [12]. This is the most precise determination of γ from direct measurements from a single experiment; other experiments are consistent, but less precise [13, 14]. These measurements involve only tree level process, making them theoretically clean. New particles that are not predicted in the SM can only contribute at higher order, and are therefore highly suppressed.

A global fit to the CKM triangle from CKMfitter [15], shown in Fig. 2.3, uses the current best measurements of various quantities, such as β, Δm_d and Δm_s, as inputs, where Δm_d and Δm_s are the mass differences between the mass eigenstates of B^0-$\overline{B}^0$ and B_s^0-$\overline{B}_s^0$ respectively. When performing this fit any information on γ from direct measurements can be ignored. Assuming the SM, i.e. unitarity of CKM matrix, γ can be extracted from the global fit. This is known as an indirect measurement. The measurements for the inputs used include loop processes. The presence of loops in the corresponding Feynman diagrams allows additional Beyond the Standard Model diagrams, where new particles appear in the loop contributing to the amplitude at the same order. Therefore, these loop processes, and by extension the extracted indirect measurement of γ, are sensitive to New Physics. This method

obtains a γ measurement of $(65.3^{+1.0}_{-2.5})^{\circ}$, where this determination of γ excludes all direct measurements and assumes the SM. The leading theoretical uncertainties on the indirect measurement are from lattice QCD, therefore these uncertainties are expected to decrease as lattice QCD calculations become more accurate.

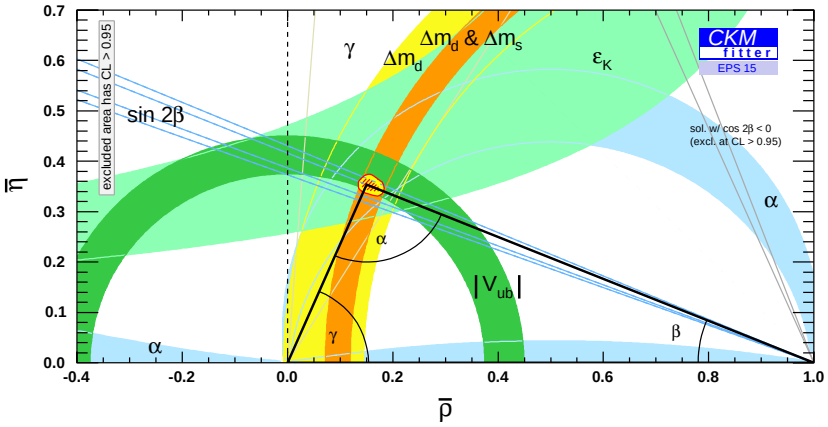

Figure 2.3: Diagram showing the current state of measurements of the unitarity triangle [15]. The black line shows the best fit obtained by CKMfitter. The axes $\bar{\rho}$ and $\bar{\eta}$ are the normalised versions of the ρ and η parameters in the Wolfenstein parameterisation of the CKM matrix, shown in Eq. 2.4.

The direct and indirect measurements of γ are currently consistent with each other, however, the result of γ from direct measurements has a relatively large uncertainty and higher central value. Therefore, improving the precision of the direct measurement of γ is necessary to verify whether or not the direct and indirect measurements are consistent, thereby testing the consistency of the SM. Improvements in the precision can be achieved through a combination of methods and measurements of various B decays that are sensitive to γ; those relevant to this thesis are outlined below.

2.5 Tree-level determination of γ using $B^{\pm} \to DK^{(*)\pm}$ decays

Direct measurements of γ can be made by exploiting the interference between $b \to c\bar{u}s$ and $b \to u\bar{c}s$ transitions. These transitions are present at tree-level in $B^{\pm} \to DK^{*\pm}$ decays, represented by the Feynman diagrams shown in Fig. 2.4,

showing the $B^- \to D^0 K^{*-}$ decay (left) and the $B^- \to \overline{D}^0 K^{*-}$ decay (right). Here, as previously mentioned, D represents the superposition of D^0 and $\overline{D}^0$ mesons. The branching fraction is of similar order to $B^- \to \overline{D}^0 K^-$ which has been extensively analysed [16–18].

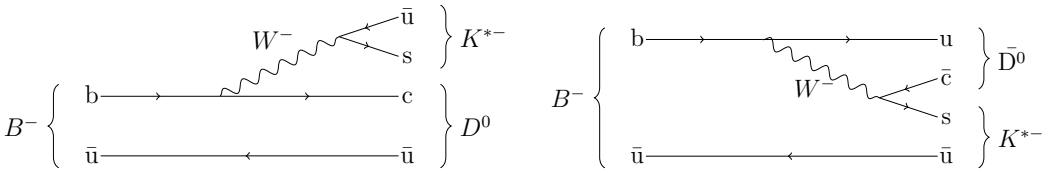

Figure 2.4: Leading order Feynman diagrams for $B^- \to D^0 K^{*-}$ (left) and $B^- \to \overline{D}^0 K^{*-}$ (right).

The ratio of the amplitudes between the $B^- \to \overline{D}^0 K^{*-}$ decay and the $B^- \to D^0 K^{*-}$ decay, and their charge conjugates are given by,

$$\frac{\mathcal{A}\left(B^- \to \overline{D}^0 K^{*-}\right)}{\mathcal{A}\left(B^- \to D^0 K^{*-}\right)} = r_B^{DK^*} e^{i(\delta_B^{DK^*} - \gamma)} \ , \ \frac{\mathcal{A}\left(B^+ \to D^0 K^{*+}\right)}{\mathcal{A}\left(B^+ \to \overline{D}^0 K^{*+}\right)} = r_B^{DK^*} e^{i(\delta_B^{DK^*} + \gamma)} \ . \tag{2.5}$$

There are three parameters in Eq. 2.5: $r_B^{DK^*}$, $\delta_B^{DK^*}$ and γ. Here $r_B^{DK^*}$ is the magnitude of the ratio of the amplitudes and $\delta_B^{DK^*}$ is difference in strong phase between the $B^- \to D^0 K^{*-}$ and $B^- \to \overline{D}^0 K^{*-}$ decays. When the D meson is reconstructed in a final state accessible to both D^0 and $\overline{D}^0$ meson states, $f(D)$, interference occurs, as shown in Fig. 2.5. This interference gives sensitivity to the weak phase γ.

In the following description we assume CP violation in the charm sector is negligible, and effects of D mixing are neglected [19, 20]. The partial widths for

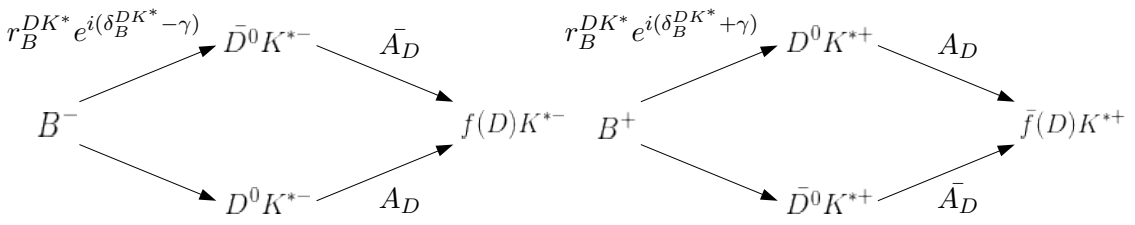

Figure 2.5: Diagram of the interfering amplitudes of $B^- \to DK^{*-}$ (left) and $B^+ \to DK^{*+}$ (right), where A_D is the amplitude of $D^0 \to f(D)$ and $\bar{A}_D$ is the amplitude of $\overline{D}^0 \to f(D)$.

the B^- and B^+ decays are given by Eqs. 2.6 and 2.7, where A_D is the amplitude of $D^0 \to f(D)$ and $\bar{A_D}$ is the amplitude of $\overline{D}^0 \to f(D)$.

$$\Gamma\left(B^- \to [f(D)]K^{*-}\right) \propto |A_D|^2 + (r_B^{DK^*})^2|\bar{A_D}|^2 + 2r_B^{DK^*} Re\left[A_D \bar{A_D} e^{-i(\delta_B^{DK^*} - \gamma)}\right] \tag{2.6}$$

$$\Gamma\left(B^+ \to [f(D)]K^{*+}\right) \propto |A_D|^2 + (r_B^{DK^*})^2|\bar{A_D}|^2 + 2r_B^{DK^*} Re\left[A_D \bar{A_D} e^{-i(\delta_B^{DK^*} + \gamma)}\right] \tag{2.7}$$

The values of the complex amplitudes, A_D and $\bar{A_D}$, depend on the D meson final state chosen. The sensitivity to γ can therefore be maximised by a judicious choice of D^0 decay mode, through the dependencies of A_D and $\bar{A_D}$.

2.5.1 The GLW and quasi-GLW methods

The theorists Gronau, London and Wyler proposed the study of $B^- \to DK^-$ modes with the D decays into a *CP* eigenstate, referred to as the GLW method [21, 22], such as the eigenstates $D^0 \to K^+K^-$ and $D^0 \to \pi^+\pi^-$. A *CP* eigenstate is a state which is preserved under a *CP* transformation. As these final states are *CP*-even, $A_D = \bar{A_D}$, and hence the expressions from Eqs. 2.6 and 2.7 can be simplified to

$$\Gamma\left(B^- \to [f_{GLW}]K^{*-}\right) \propto 1 + (r_B^{DK^*})^2 + 2r_B^{DK^*}\cos(\delta_B^{DK^*} - \gamma) \tag{2.8}$$

$$\Gamma\left(B^+ \to [f_{GLW}]K^{*+}\right) \propto 1 + (r_B^{DK^*})^2 + 2r_B^{DK^*}\cos(\delta_B^{DK^*} + \gamma)\ , \tag{2.9}$$

assuming that *CP* violation in D decays is negligible and $\mathcal{A}(B^- \to D^0K^{*-}) = \mathcal{A}\left(B^+ \to \overline{D}^0K^{*+}\right)$.

The four-body D decay mode $D \to \pi^+\pi^-\pi^+\pi^-$ is a self-conjugate decay mode, containing a mixture of *CP*-even and *CP*-odd states, which can be used to measure γ via the GLW method provided the fractional *CP*-even content is known [23]. As this mode is not a pure *CP* eigenstate, it is referred to as a quasi-GLW (qGLW) mode, and its sensitivity to γ is reduced. The *CP*-even fraction, $F_{4\pi}$, measured to be 0.737 ± 0.028 [24], accounts for the dilution effect. The partial widths for this self-conjugate qGLW mode [23, 24], corresponding to Eqs. 2.8 and 2.9, are

$$\Gamma\left(B^- \to [f_{qGLW}]K^{*-}\right) \propto 1 + (r_B^{DK^*})^2 + 2r_B^{DK^*}(2F_{4\pi} - 1)\cos(\delta_B^{DK^*} - \gamma) \tag{2.10}$$

$$\Gamma\left(B^+ \to [f_{GLW}]K^{*+}\right) \propto 1 + (r_B^{DK^*})^2 + 2r_B^{DK^*}(2F_{4\pi} - 1)\cos(\delta_B^{DK^*} + \gamma)\ . \tag{2.11}$$

In Eqs. 2.10 and 2.11, it can be seen that the expression $2F_{4\pi} - 1$ governs the size of the γ-sensitive interference term.

2.5.2 The ADS method

The theorists Atwood, Dunietz and Soni proposed looking at D decay modes where $f(D)$ is a non-*CP* eigenstate, *e.g.* $D \to K^-\pi^+$, referred to as the ADS method [25, 26]. A key feature of this method is that although the D^0 and $\overline{D}^0$ decay to the same final state, they proceed by very different amplitudes. The Feynman diagrams for the doubly Cabibbo-favoured $D^0 \to K^-\pi^+$ decay and the doubly Cabibbo-suppressed $D^0 \to K^+\pi^-$ decay are shown in Fig. 2.6.

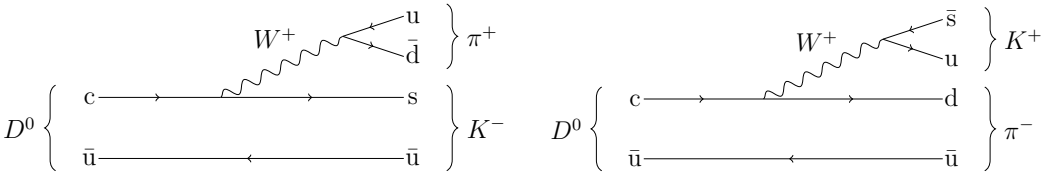

Figure 2.6: Leading order Feynman diagrams for $D^0 \to K^-\pi^+$ (left) and $D^0 \to K^+\pi^-$ (right).

The ratio of the amplitudes of $\overline{D}^0 \to K^-\pi^+$ and $D^0 \to K^-\pi^+$ is given by[1]

$$\frac{\mathcal{A}\left(\overline{D}^0 \to K^-\pi^+\right)}{\mathcal{A}\left(D^0 \to K^-\pi^+\right)} = r_D^{K\pi} e^{-i\delta_D^{K\pi}} \ , \tag{2.12}$$

where the parameter $r_D^{K\pi}$ is the magnitude of the ratio of amplitudes and $\delta_D^{K\pi}$ is the difference in strong phase between the suppressed and favoured decays. These parameters have been previously measured to be $r_D^{K\pi} = 0.0591 \pm 0.0003$ and $\delta_D^{K\pi} = (191.8 \pm 12.1)^\circ$ [28].

Equation 2.12 can be expressed as $\bar{A_D}/A_D = r_D^{K\pi} e^{-i\delta_D^{K\pi}}$ for the case where $f(D)$ is $K^-\pi^+$, and similarly, $A_D/\bar{A_D} = r_D^{K\pi} e^{-i\delta_D^{K\pi}}$ for the case where $f(D)$ is $K^+\pi^-$.

[1]The *CP* operator acting on the state $|D^0\rangle$ can result in either $CP|D^0\rangle = |\overline{D}^0\rangle$ or $CP|D^0\rangle = -|\overline{D}^0\rangle$. This has consequences for the definition of the strong phase difference. In the ADS formalism, which is used here, the definition $CP|D^0\rangle = |\overline{D}^0\rangle$ is used, resulting in Eq. 2.12. The alternative definition, $CP|D^0\rangle = -|\overline{D}^0\rangle$, used by HFLAV and in the CLEO-c analysis in Ref [27], would result in $r_D^{K\pi} e^{-i(\pi+\delta_D^{K\pi})}$. The consequence of this is that the measured value of the strong phase difference taken from Ref. [27] must be offset by 180° when used in the analysis presented in this thesis.

Using these expressions, the partial widths from Eqs. 2.6 and 2.7 for the various $B^{\pm} \to DK^{*\pm}$ ADS decay modes are given by

$$\Gamma\left(B^- \to [K^+\pi^-]K^{*-}\right) \propto (r_B^{DK^*})^2 + (r_D^{K\pi})^2 + 2r_B^{DK^*} r_D^{K\pi} \cos(\delta_B^{DK^*} + \delta_D^{K\pi} - \gamma) \tag{2.13}$$

$$\Gamma\left(B^+ \to [K^-\pi^+]K^{*+}\right) \propto (r_B^{DK^*})^2 + (r_D^{K\pi})^2 + 2r_B^{DK^*} r_D^{K\pi} \cos(\delta_B^{DK^*} + \delta_D^{K\pi} + \gamma) \tag{2.14}$$

$$\Gamma\left(B^- \to [K^-\pi^+]K^{*-}\right) \propto 1 + (r_B^{DK^*})^2 (r_D^{K\pi})^2 + 2r_B^{DK^*} r_D^{K\pi} \cos(\delta_B^{DK^*} + \delta_D^{K\pi} + \gamma) \tag{2.15}$$

$$\Gamma\left(B^+ \to [K^+\pi^-]K^{*+}\right) \propto 1 + (r_B^{DK^*})^2 (r_D^{K\pi})^2 + 2r_B^{DK^*} r_D^{K\pi} \cos(\delta_B^{DK^*} + \delta_D^{K\pi} - \gamma). \tag{2.16}$$

For the analysis considered in this thesis, the favoured decay contains a K^{*-} meson and pion from the D meson of opposite charge, while in the suppressed decay the K^{*-} meson and the pion from the D meson have the same charge. The ADS decay mode is a combination of a CKM-favoured $B^- \to D^0 K^{*-}$ decay (Fig. 2.4, left), followed by a doubly Cabibbo-suppressed $D^0 \to K^+\pi^-$ decay (Fig. 2.6, right), and a CKM- and colour-suppressed $B^- \to \overline{D}^0 K^{*-}$ decay (Fig. 2.4, right), followed by a Cabibbo-favoured $\overline{D}^0 \to K^+\pi^-$ decay (Fig. 2.6, left). Both paths to the same final state have amplitudes of similar size, and interference effects are therefore magnified in comparison to the GLW decay modes, where the decay path via the CKM-favoured $B^- \to D^0 K^{*-}$ decay dominates.

Two-body $D \to K^{\mp}\pi^{\pm}$ decays are characterised by two parameters, an amplitude ratio and a single strong phase, as illustrated in Eq. 2.12. However for multibody $D \to K^{\mp}\pi^{\pm}\pi^{\mp}\pi^{\pm}$ decays, the strong phase varies over the phase space. Therefore, the amplitude at each point in phase space, p, must be considered for both the $D^0 \to K^-\pi^+\pi^-\pi^+$ favoured and $D^0 \to K^+\pi^-\pi^+\pi^-$ suppressed decays, referred to as $A_{fav}(p)$ and $A_{sup}(p)$ respectively. The three hadronic parameters that describe the $D \to K^-\pi^+\pi^-\pi^+$ decay [29–31] are defined by

$$\left(r_D^{K3\pi}\right)^2 = \frac{\int \mathrm{d}p\, |A_{sup}(p)|^2}{\int \mathrm{d}p\, |A_{fav}(p)|^2} \tag{2.17}$$

and

$$R_{K3\pi}e^{i\delta_D^{K3\pi}} = \frac{\int \mathrm{d}p A_{fav}(p) A_{sup}(p)}{\sqrt{\int \mathrm{d}p \left|A_{fav}(p)\right|^2 \int \mathrm{d}p \left|A_{sup}(p)\right|^2}} , \tag{2.18}$$

where $r_D^{K3\pi}$ is the amplitude ratio between suppressed and favoured $D \to K^-\pi^+\pi^-\pi^+$ decays (analogous to $r_D^{K\pi}$), $R_{K3\pi}$ is a coherence factor to account for the dilution of the interference effects due to averaging over phase space, and $\delta_D^{K3\pi}$ is the strong phase difference (analogous to $\delta_D^{K\pi}$). These parameters have been measured to be $r_D^{K3\pi} = 0.0549 \pm 0.0006$, $R_{K3\pi} = 0.43 \pm 0.17$ and $\delta_D^{K3\pi} = (128 \pm 28)^\circ$ [29–31]. Based on the definitions in Eqs. 2.17 and 2.18, the partial widths are given by

$$\Gamma\left(B^- \to [K^+\pi^-]K^{*-}\right) \propto (r_B^{DK^*})^2 + (r_D^{K3\pi})^2 + 2r_B^{DK^*} R_{K3\pi} r_D^{K3\pi} \cos(\delta_B^{DK^*} + \delta_D^{K3\pi} - \gamma) \tag{2.19}$$

$$\Gamma\left(B^+ \to [K^-\pi^+]K^{*+}\right) \propto (r_B^{DK^*})^2 + (r_D^{K3\pi})^2 + 2r_B^{DK^*} R_{K3\pi} r_D^{K3\pi} \cos(\delta_B^{DK^*} + \delta_D^{K3\pi} + \gamma) \tag{2.20}$$

$$\Gamma\left(B^- \to [K^-\pi^+]K^{*-}\right) \propto 1 + (r_B^{DK^*})^2 (r_D^{K3\pi})^2 + 2r_B^{DK^*} R_{K3\pi} r_D^{K3\pi} \cos(\delta_B^{DK^*} + \delta_D^{K3\pi} + \gamma) \tag{2.21}$$

$$\Gamma\left(B^+ \to [K^+\pi^-]K^{*+}\right) \propto 1 + (r_B^{DK^*})^2 (r_D^{K3\pi})^2 + 2r_B^{DK^*} R_{K3\pi} r_D^{K3\pi} \cos(\delta_B^{DK^*} + \delta_D^{K3\pi} - \gamma) \, . \tag{2.22}$$

It can be seen from these equations that the four-body coherence factor, $R_{K3\pi}$, governs the size of the interference term that carries the dependence on γ.

2.5.3 Physical observables

This thesis aims to measure γ as well as the hadronic parameters of $B^- \to DK^{*-}$ decays, with the K^{*-} meson decaying to $K^0_S\pi^-$, using the methods and equations discussed in Secs. 2.5.1 and 2.5.2. However, experimental considerations must be taken into account when developing the strategy to measure these parameters. For example, the use of the parameters $r_B^{DK^*}$ and $\delta_B^{DK^*}$ discussed in Sec. 2.5 assumes that a pure sample of $B^- \to DK^{*-}$ decays is available. This section introduces the $B^- \to DK^{*-}$ coherence factor, κ, which deals with the contamination from other $B^- \to DK^0_S\pi^-$ processes in order to extract the parameters of interest. This section also describes the experimental quantities that are measured in this analysis in order to gain maximum sensitivity to γ.

Coherence factor

As discussed earlier in this chapter, this thesis considers $B^- \to DK^{*-}$, $K^{*-} \to K^0_S\pi^-$ decays. The K^{*-} meson could be reconstructed in either of the $K^0_S\pi^-$ or $K^-\pi^0$ final states, however, due to the higher reconstruction efficiency of the K^0_S meson compared to the π^0 meson, the $K^0_S\pi^-$ final state is pursued. As the K^{*-} meson has a large natural width (about 50 MeV/c^2 [10]), it is necessary to consider the effect of other resonant and non-resonant $B^- \to DK^0_S\pi^-$ decays on the experimental measurements of the physics parameters, $r_B^{DK^*}$, $r_B^{DK^*}$ and γ. The amplitudes and phases of the different decays will vary at each point in $B^- \to DK^0_S\pi^-$ phase space, as given by

$$A(B^- \to D^0X^-) = A_c(p)e^{i\delta_c(p)}$$
$$A(B^- \to \bar{D}^0X^-) = A_u(p)e^{i(\delta_u(p)-\gamma)} \ ,$$

where p is the point in $(m^2(K^0_S\pi^-), m^2(D\pi^-))$ space, where $m^2(K^0_S\pi^-) = (p_{K^0_S} + p_{\pi^-})^2$, and $m^2(D\pi^-) = (p_D + p_{\pi^-})^2$. Here p_X is the four-momentum of particle X, the expressions $A_u(p)$ and $A_c(p)$ are the moduli of the $b\to u$ and $b\to c$ amplitudes respectively, while $\delta_c(p)$ and $\delta_u(p)$ represent the strong phases of the relevant decay amplitudes. The symbol X^- represents a resonant or non-resonant $K^0_S\pi^-$ pair, which could be produced by the decay of the K^{*-} meson or by other contributions to the $B^-\to DK^0_S\pi^-$ final state. The amplitudes of the B^+ decays can be expressed as

$$A(B^+\to \overline{D}^0X^+) = A_c(p)e^{i\delta_c(p)}$$
$$A(B^+\to D^0X^+) = A_u(p)e^{i(\delta_u(p)+\gamma)} \ .$$

Due to the large natural width of the K^{*-} meson, interference may occur in the region near the K^{*-} mass between the signal K^{*-} decay amplitude and amplitudes due to other $B^- \to DK^0_S\pi^-$ contributions, for example higher $K^0_S\pi^-$ resonances and non-resonant decays. The interfering contributions dilute the sensitivity to γ, which is quantified by the $B^- \to DK^{*-}$ coherence factor, κ, where $0 \leq \kappa \leq 1$,

and $\kappa = 1$ denotes a pure K^{*-} contribution giving maximum sensitivity to γ. The parameters r_B, δ_B and κ are then defined for $B^- \to DK^{*-}$ decays as

$$r_B^2 = \frac{\Gamma(B^- \to \bar{D}^0 X^-)}{\Gamma(B^- \to D^0 X^-)} = \frac{\int |A_u(p)|^2 \, \mathrm{d}p}{\int |A_c(p)|^2 \, \mathrm{d}p} \tag{2.23}$$

$$\kappa e^{i\delta_B} = \frac{\int \mathrm{d}p A_c(p) A_u(p) e^{i\delta(p)}}{\sqrt{\int \mathrm{d}p \, |A_u(p)|^2 \int \mathrm{d}p \, |A_c(p)|^2}} \, , \tag{2.24}$$

where p represents a point in phase space, $0 \leq \delta(p) \leq 2\pi$, and the integration is performed over a defined K^{*-} region. In Eqs. 2.23 and 2.24, the parameters r_B, δ_B and κ depend on the region of the $B^- \to DK^0_S\pi^-$ phase space that is integrated over. In order to maximise sensitivity to γ an integration region should be chosen that finds the optimal working point between maximising the coherence factor and maximising the size of the data sample available.

As before, it is assumed that *CP* violation in the charm sector is negligible, and effects of D mixing are neglected [19, 20]. The partial widths for the B^- and B^+ decays are then given by Eqs. 2.25 and 2.26, where A_D is the amplitude of $D^0 \to f(D)$ and $\bar{A_D}$ is the amplitude of $\overline{D}^0 \to f(D)$.

$$\frac{d\Gamma\left(B^- \to [f(D)]X^-\right)}{dp} \propto |A_c(p) e^{i\delta_c(p)} A_D + A_u(p) e^{i(\delta_u(p)-\gamma)} \bar{A_D}|^2 \tag{2.25}$$

$$\frac{d\Gamma\left(B^+ \to [f(D)]X^-\right)}{dp} \propto |A_u(p) e^{i(\delta_u(p)+\gamma)} \bar{A_D} + A_c(p) e^{i\delta_c(p)} A_D|^2 \tag{2.26}$$

Expanding and integrating over the defined K^* region gives

$$\Gamma\left(B^- \to [f(D)]X^-\right) \propto |A_D|^2 + r_B^2 |\bar{A_D}|^2 + 2\kappa r_B Re\left[A_D \bar{A_D} e^{-i(\delta_B - \gamma)}\right] \tag{2.27}$$

$$\Gamma\left(B^+ \to [f(D)]X^-\right) \propto |A_D|^2 + r_B^2 |\bar{A_D}|^2 + 2\kappa r_B Re\left[A_D \bar{A_D} e^{-i(\delta_B + \gamma)}\right] \tag{2.28}$$

A comparison between Eqs. 2.6 and 2.7 and Eqs. 2.27 and 2.28 shows that in order to account for the fact that the $B^- \to DK^{*-}$ sample contains small contributions from other resonant and non-resonant $B^- \to DK^0_S\pi^-$ decays, the substitutions $(r_B^{DK^*})^2 \to r_B^2$, $r_B^{DK^*} \to \kappa r_B$ and $\delta_B^{DK^*} \to \delta_B$, are evident. In particular for $\kappa = 1$, Eqs. 2.6 and 2.7 are recovered. The coherence factor, κ, that accounts for contributions from other resonant and non-resonant $B^- \to DK^0_S\pi^-$ decays, governs the size of the interference term that carries the dependence on γ.

CP observables

Using the GLW, qGLW and ADS methods, discussed in Secs. 2.5.1 and 2.5.2, observable quantities are constructed that can be used to extract r_B, δ_B and γ. The decay rates for the GLW modes, in Eqs. 2.8 - 2.11, the two-body ADS modes, in Eqs. 2.13 - 2.16, and the four-body ADS modes, in Eqs. 2.19 - 2.22, can be measured directly by counting the number of observed events. However, by constructing ratios of these decay rates many experimental uncertainties will cancel, thus improving the precision of the results.

The observables used in this thesis are the asymmetries between the B^- and B^+ decay rates, as well as ratios of decay rates in comparison to the favoured modes for the different D^0 final states. No *CP* asymmetry is expected in the two- and four-body favoured D^0 decay modes. The twelve quantities, collectively referred to as *CP* observables, that are measured in this analysis are:

- The *CP* asymmetry for the favoured decay mode

$$A_{K\pi} = \frac{\Gamma\left(B^- \to D(K^-\pi^+)K^{*-}\right) - \Gamma\left(B^+ \to D(K^+\pi^-)K^{*+}\right)}{\Gamma\left(B^- \to D(K^-\pi^+)K^{*-}\right) + \Gamma\left(B^+ \to D(K^+\pi^-)K^{*+}\right)} \,. \tag{2.29}$$

- The *CP* asymmetry for the $D \to K^+K^-$ decay mode

$$A_{KK} = \frac{\Gamma\left(B^- \to D(K^+K^-)K^{*-}\right) - \Gamma\left(B^+ \to D(K^+K^-)K^{*+}\right)}{\Gamma\left(B^- \to D(K^+K^-)K^{*-}\right) + \Gamma\left(B^+ \to D(K^+K^-)K^{*+}\right)} \,. \tag{2.30}$$

- The *CP* asymmetry for the $D \to \pi^+\pi^-$ decay mode

$$A_{\pi\pi} = \frac{\Gamma\left(B^- \to D(\pi^+\pi^-)K^{*-}\right) - \Gamma\left(B^+ \to D(\pi^+\pi^-)K^{*+}\right)}{\Gamma\left(B^- \to D(\pi^+\pi^-)K^{*-}\right) + \Gamma\left(B^+ \to D(\pi^+\pi^-)K^{*+}\right)} \,. \tag{2.31}$$

- The ratio of the rate for the $D \to K^+K^-$ decay mode to that of the favoured decay mode, scaled by the branching fractions

$$R_{KK} = \frac{\Gamma\left(B^- \to D(K^+K^-)K^{*-}\right) + \Gamma\left(B^+ \to D(K^+K^-)K^{*+}\right)}{\Gamma\left(B^- \to D(K^-\pi^+)K^{*-}\right) + \Gamma\left(B^+ \to D(K^+\pi^-)K^{*+}\right)} \times \frac{\mathcal{B}(D^0 \to K^-\pi^+)}{\mathcal{B}(D^0 \to K^+K^-)} \,. \tag{2.32}$$

- The ratio of the rate for the $D \to \pi^+\pi^-$ decay mode to that of the favoured decay mode, scaled by the branching fractions

$$R_{\pi\pi} = \frac{\Gamma\left(B^- \to D(\pi^+\pi^-)K^{*-}\right) + \Gamma\left(B^+ \to D(\pi^+\pi^-)K^{*+}\right)}{\Gamma\left(B^- \to D(K^-\pi^+)K^{*-}\right) + \Gamma\left(B^+ \to D(K^+\pi^-)K^{*+}\right)} \times \frac{\mathcal{B}(D^0 \to K^-\pi^+)}{\mathcal{B}(D^0 \to \pi^+\pi^-)} \,. \quad (2.33)$$

- The ratio of the rate for the ADS decay mode to that of the favoured decay mode for B^+ decays

$$R^+_{K\pi} = \frac{\Gamma\left(B^+ \to D(K^-\pi^+)K^{*+}\right)}{\Gamma\left(B^+ \to D(K^+\pi^-)K^{*+}\right)} \,. \quad (2.34)$$

- The ratio of the rate for the ADS decay mode to that of the favoured decay mode for B^- decays

$$R^-_{K\pi} = \frac{\Gamma\left(B^- \to D(K^+\pi^-)K^{*-}\right)}{\Gamma\left(B^- \to D(K^-\pi^+)K^{*-}\right)} \,. \quad (2.35)$$

- The *CP* asymmetry for the favoured $D^0 \to K^-\pi^+\pi^-\pi^+$ decay mode

$$A_{K\pi\pi\pi} = \frac{\Gamma\left(B^- \to D(K^-\pi^+\pi^-\pi^+)K^{*-}\right) - \Gamma\left(B^+ \to D(K^+\pi^-\pi^+\pi^-)K^{*+}\right)}{\Gamma\left(B^- \to D(K^-\pi^+\pi^-\pi^+)K^{*-}\right) + \Gamma\left(B^+ \to D(K^+\pi^-\pi^+\pi^-)K^{*+}\right)} \,. \quad (2.36)$$

- The *CP* asymmetry for the $D \to \pi^+\pi^-\pi^+\pi^-$ decay mode

$$A_{\pi\pi\pi\pi} = \frac{\Gamma\left(B^- \to D(\pi^+\pi^-\pi^+\pi^-)K^{*-}\right) - \Gamma\left(B^+ \to D(\pi^+\pi^-\pi^+\pi^-)K^{*+}\right)}{\Gamma\left(B^- \to D(\pi^+\pi^-\pi^+\pi^-)K^{*-}\right) + \Gamma\left(B^+ \to D(\pi^+\pi^-\pi^+\pi^-)K^{*+}\right)} \,. \quad (2.37)$$

- The ratio of the rate for the $D \to \pi^+\pi^-\pi^+\pi^-$ decay mode to that of the favoured decay mode, scaled by the branching fractions

$$R_{\pi\pi\pi\pi} = \frac{\Gamma\left(B^- \to D(\pi^+\pi^-\pi^+\pi^-)K^{*-}\right) + \Gamma\left(B^+ \to D(\pi^+\pi^-\pi^+\pi^-)K^{*+}\right)}{\Gamma\left(B^- \to D(K^-\pi^+\pi^-\pi^+)K^{*-}\right) + \Gamma\left(B^+ \to D(K^+\pi^-\pi^+\pi^-)K^{*+}\right)} \times \frac{\mathcal{B}(D^0 \to K^-\pi^+\pi^-\pi^+)}{\mathcal{B}(D^0 \to \pi^+\pi^-\pi^+\pi^-)} \,. \quad (2.38)$$

- The ratio of the rate for the four-body ADS decay mode to that of the four-body favoured decay mode for B^+ decays

$$R^+_{K\pi\pi\pi} = \frac{\Gamma\left(B^+ \to D(K^-\pi^+\pi^-\pi^+)K^{*+}\right)}{\Gamma\left(B^+ \to D(K^+\pi^-\pi^+\pi^-)K^{*+}\right)} \,. \quad (2.39)$$

- The ratio of the rate of the four-body ADS decay mode to that of the four-body favoured decay mode for B^- decays

$$R^-_{K\pi\pi\pi} = \frac{\Gamma\left(B^- \to D(K^+\pi^-\pi^+\pi^-)K^{*-}\right)}{\Gamma\left(B^- \to D(K^-\pi^+\pi^-\pi^+)K^{*-}\right)} \ . \tag{2.40}$$

The asymmetries $A_{K\pi}$ and $A_{K\pi\pi\pi}$ should be essentially zero due to the very small interference expected in the configuration of B and D decays. Due to negligible direct *CP* violation in D decays [19], the observables A_{KK} and $A_{\pi\pi}$ should be equal and are often labelled together as A_{CP+}; similarly the observables R_{KK} and $R_{\pi\pi}$ should be equal and are labelled R_{CP+}.[2] The observables R_{KK}, $R_{\pi\pi}$ and $R_{\pi\pi\pi\pi}$ are scaled by the relevant branching fraction ratio, as can be seen from Eqs. 2.32, 2.33 and 2.38 respectively. This is done in order to construct a *CP* observable that is independent of final state, i.e. only depends on hadronic parameters of the B^- decay.

The *CP* observables measured in this analysis can be related to the physics parameters to be determined, namely γ, r_B and δ_B. Given there is a negligible effect from both charm mixing [20] and *CP* violation in D decays [19], the relationships between the *CP* observables and physics parameters are summarised by the following equations:

$$A_{CP+} = \frac{2\kappa r_B \sin\delta_B \sin\gamma}{1 + r_B^2 + 2\kappa r_B \cos\delta_B \cos\gamma} \ , \tag{2.41}$$

$$R_{CP+} = 1 + r_B^2 + 2\kappa r_B \cos\delta_B \cos\gamma \ , \tag{2.42}$$

$$R^{\pm}_{K\pi} = \frac{r_B^2 + \left(r_D^{K\pi}\right)^2 + 2\kappa r_B r_D^{K\pi} \cos(\delta_B + \delta_D^{K\pi} \pm \gamma)}{1 + r_B^2 \left(r_D^{K\pi}\right)^2 + 2\kappa r_B r_D^{K\pi} \cos(\delta_B - \delta_D^{K\pi} \pm \gamma)} \ , \tag{2.43}$$

$$A_{\pi\pi\pi\pi} = \frac{2\kappa \left(2F_{4\pi} - 1\right) r_B \sin\delta_B \sin\gamma}{1 + r_B^2 + 2\kappa \left(2F_{4\pi} - 1\right) r_B \cos\delta_B \cos\gamma} \ , \tag{2.44}$$

$$R_{\pi\pi\pi\pi} = 1 + r_B^2 + 2\kappa \left(2F_{4\pi} - 1\right) r_B \cos\delta_B \cos\gamma \ , \tag{2.45}$$

$$R^{\pm}_{K\pi\pi\pi} = \frac{r_B^2 + \left(r_D^{K3\pi}\right)^2 + 2\kappa r_B \kappa_{K3\pi} r_D^{K3\pi} \cos(\delta_B + \delta_D^{K3\pi} \pm \gamma)}{1 + \left(r_B r_D^{K3\pi}\right)^2 + 2\kappa r_B \kappa_{K3\pi} r_D^{K3\pi} \cos(\delta_B - \delta_D^{K3\pi} \pm \gamma)} \ . \tag{2.46}$$

[2]The analogous observables to R_{CP+} and A_{CP+} for the ADS mode are R_{ADS} and A_{ADS}. However, R_{ADS} and A_{ADS} are not used here for the ADS decay mode, instead the ratios are measured separately for the positive and negative charges. The reason for this choice is that the uncertainty in A_{ADS} depends on the value of R_{ADS}, therefore these observables are statistically dependent, raising problems for the low yields expected in the ADS mode. Hence the statistically independent observables $R^+_{K\pi}$ and $R^-_{K\pi}$ are preferred.

These six relationships contain 10 unknown parameters: the three parameters of interest, namely r_B, δ_B and γ, the coherence factor relating to the B^- decay, κ, which has a value specific for this analysis, and six parameters, namely $r_D^{K\pi}$, $\delta_D^{K\pi}$, $r_D^{K3\pi}$, $\delta_D^{K3\pi}$, $R_{K3\pi}$ and $F_{4\pi}$ describing the various D^0 decays, which have all been measured with relatively small uncertainties [24, 29–31]. Therefore, the strategy taken in this thesis to extract r_B, δ_B and γ is to constrain the six parameters describing the various D^0 decays directly from existing measurements, which allows a more precise determination of the parameters of interest.

The angles δ_B and γ relate to the *CP* observables via the trigonometric functions sin and cos, as shown in Eqs. 2.41 - 2.46. These relationships result in a two-fold ambiguity in the interpretation of the angles between θ or $180° - \theta$, where θ corresponds to δ_B or γ. Therefore, the results are expected to have multiple solutions.

2.6 Previous γ measurements with $B^\pm \to DK^{(*)\pm}$ decays

The $B^- \to DK^-$ channel is a very important mode for tree level γ measurements, as it is straightforward to reconstruct and has a fairly high branching fraction of 3.7×10^{-4} [10]. This $B^- \to DK^-$ channel is thoroughly exploited at LHCb, having yielded many γ-sensitive measurements using an extensive range of D meson final states:

- $D \to K^+\pi^-$, K^+K^-, $\pi^+\pi^-$ [32],
- $D \to K^+\pi^-\pi^+\pi^-$, $\pi^+\pi^-\pi^+\pi^-$ [16],
- $D \to K^+\pi^-\pi^0$, $K^+K^-\pi^0$, $\pi^+\pi^-\pi^0$ [18],
- $D \to K^0_S K^+K^-$, $K^0_S\pi^+\pi^-$ [17],
- $D \to K^0_S K^+\pi^-$ [33].

A combination of these γ-sensitive *CP* violation measurements performed by LHCb, in addition to other modes, has yielded a combined result of $\gamma = \left(72.2^{+6.8}_{-7.3}\right)^\circ$ [12], which is the most precise direct determination of γ to date.

Other modes used to constrain γ at LHCb include, $B^0 \to DK^{*0}$ decays and the time-dependent $B_s^0 \to D_s^{\pm}K^{\mp}$ decays yielding individual measurements of $\gamma = (71 \pm 20)^\circ$ and $\gamma = (115^{+28}_{-43})^\circ$ (mod 180°) respectively [34, 35]. Previous B-factory experiments, namely the BaBar and Belle experiments, have also produced constraints on the CKM angle γ from charged and neutral B decays. For example, decays of $B^- \to DK^-$, D^*K^-, DK^{*-} and neutral B decays to $D^{(*)}K^{(*)}$ have been reported [36–43]. A combination of measurements from BaBar and Belle experiments separately obtained results of $\gamma = (69^{+17}_{-16})^\circ$ and $\gamma = (68^{+15}_{-14})^\circ$ respectively [13, 14].

The $B^- \to DK^{*-}$ channel is analogous to the frequently used $B^- \to DK^-$ decay in its physical properties, as well as having a comparable branching fraction of 5.3×10^{-4} [10]. However, prior to the work presented in this thesis, the $B^- \to DK^{*-}$ channel had not been investigated at LHCb. The K^{*-} decays almost exclusively to $K^0\pi^-$ and $K^-\pi^0$ final states, both of which involve a neutral particle. This makes $B^- \to DK^{*-}$ decays much more difficult to reconstruct at LHCb than $B^- \to DK^-$ decays, resulting in the $B^- \to DK^{*-}$ channel having a lower sensitivity to γ. However, the $B^- \to DK^{*-}$ channel contains fewer problematic backgrounds, and the unknown hadronic parameters of the $B^- \to DK^{*-}$ decay, r_B and δ_B, can be accessed. Furthermore, by measuring γ in as many different channels as possible, the uncertainty on the combined measurement of γ will be reduced, and the consistency of the result between channels can be verified.

The $B^- \to DK^{*-}$ channel has previously been investigated by the BaBar collaboration using a variety of *CP*-even, *CP*-odd and non-*CP* two-body D decay modes, namely K^-K^+, $\pi^-\pi^+$, $K^0_S\pi^0$, $K^0_S\phi$, $K^0_S\omega$ and $K^-\pi^+$ [44]. Their study produced confidence levels for γ, excluding $[85, 99]^\circ$ at the two sigma level. Also, both the BaBar and Belle collaborations have performed studies on $B^- \to DK^{*-}$ with $D \to K^0_S\pi^+\pi^-$, obtaining results of $\gamma = (76 \pm 22 \pm 5 \pm 5)^\circ$ and $\gamma = (53^{+15}_{-18} \pm 3 \pm 9)^\circ$ respectively, where the first uncertainty is statistical, the second is systematic and the third is model uncertainty [39, 43]. In all these measurements the K^{*-} meson is reconstructed in the $K^0_S\pi^-$ mode, with $K^0_S \to \pi^+\pi^-$.

In this analysis, the $B^- \to DK^{*-}$ channel is investigated, with $K^{*-} \to K^0_S\pi^-$ and $K^0_S \to \pi^-\pi^+$, where the D^0 meson in reconstructed in its decay to $K^-\pi^+$, K^+K^-, $\pi^+\pi^-$, $K^+\pi^-$, $K^-\pi^+\pi^-\pi^+$, $\pi^+\pi^-\pi^+\pi^-$ and $K^+\pi^-\pi^+\pi^-$ final states. The K^{*-} meson could be reconstructed from its decay to $K^-\pi^0$, however, the π^0 meson decays almost exclusively to two photons, which are difficult to reconstruct, and therefore the π^0 meson has a much poorer reconstruction efficiency and larger uncertainty than the K^0_S meson. Therefore the $K^-\pi^0$ mode is not pursued in this thesis.

2.7 Analysis overview

The work presented in this thesis measures the *CP* observables in $B^- \to DK^{*-}$ decays as well as considering the interpretation of these observables in terms of r_B, δ_B and γ. The analysis strategy is first to develop a procedure, based on our understanding of the data, to select $B^- \to D(K^-\pi^+)K^{*-}$ and $B^- \to D(K^-\pi^+\pi^-\pi^+)K^{*-}$ signal decays while removing unwanted background events, discussed in Sec. 4.1. The same selection with a few adjustments can subsequently be applied to the other two- and four-body D decay modes. After applying this selection, a fit model is developed to describe the B mass distribution of the remaining $B^- \to D(K^-\pi^+)K^{*-}$ and $B^- \to D(K^-\pi^+\pi^-\pi^+)K^{*-}$ candidates, detailed in Sec. 4.2. Using the fit model developed based on these modes, a simultaneous fit is then performed to all seven D modes, separated by B charge, to extract the *CP* observables, detailed in Chapter 5. Chapter 6 discusses a determination of κ using Eq. 2.24 as well as the interpretation of the *CP* observables, using Eqs. 2.41 - 2.46, in terms of the physics parameters r_B, δ_B and γ.

3
The LHCb detector

The Large Hadron Collider (LHC) is the world's largest and most powerful particle accelerator, located near Geneva, Switzerland. The LHC ring is 27 km in circumference, located 100 m underground and consists of a series of superconducting magnets and accelerating modules to boost the particle energy. Two high energy proton or heavy ion beams travel in opposite directions at centre-of-mass energies up to $\sqrt{s} = 13$ TeV. The protons are obtained by ionising hydrogen atoms. These protons are accelerated in stages through various parts of the LHC accelerator complex, as shown in Fig. 3.1. Firstly, the protons are accelerated in Linac 2 to energies of 50 MeV, followed by the Proton Synchrotron Booster (PSB), the Proton Synchrotron (PS) and the Super Proton Synchrotron (SPS), accelerating the protons to 1.4 GeV, 25 GeV and 450 GeV respectively. Finally, the protons are injected into the LHC. Two proton beams are injected in opposite directions, reaching centre-of-mass energies of up to $\sqrt{s} = 13$ TeV, and focused to collide at four locations around the LHC ring. These locations are where the four main particle physics detectors are located: the Large Hadron Collider beauty (LHCb) experiment as well as ATLAS, CMS and ALICE.

There have been two major data taking periods of the LHC, named Run 1 and Run 2. Run 1 occurred between 2010 and 2012, where the centre of mass energy was $\sqrt{s}$ =7 TeV (2010 and 2011) and 8 TeV (2012). Data collection for Run 2 began in

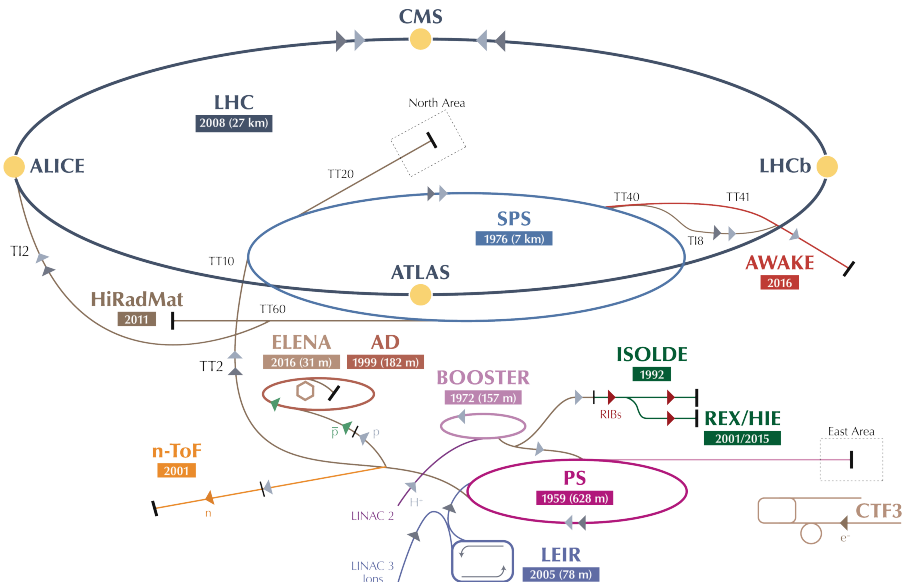

Figure 3.1: Diagram of the LHC accelerator complex.

2015 and is due to end in 2018, with $\sqrt{s}$ =13 TeV. At LHCb the collision conditions are designed to have roughly one proton-proton (pp) interaction per bunch crossing in order to allow effective primary vertex selection, necessary for the study of B and D meson decays, efficient track finding, and reduced radiation damage and detector occupancy. The low luminosity running is achieved by a process called *luminosity levelling*, which involves reducing the transverse overlap of the two beams in order to reduce the area available for interactions. This allows the peak luminosity and number of pp interactions per bunch crossing to be optimal, while maximising the integrated luminosity. Most of the LHCb data were recorded at an instantaneous luminosity of $4 \times 10^{32}\text{cm}^{-2}\text{s}^{-1}$, with an average of 1.7 pp collisions per bunch crossing for Run 1 and 1.1 for Run 2. In Run 1 collisions occurred at a frequency of 20 MHz, corresponding to collisions every 50 ns, which increased to a bunch crossing rate of 40 MHz in Run 2.

This thesis uses the complete 3 fb^{-1} Run 1 dataset corresponding to 1 fb^{-1} of $\sqrt{s}$ =7 TeV data recorded in 2011 and 2 fb^{-1} of $\sqrt{s}$ =8 TeV data recorded in 2012, as well as 1.8 fb^{-1} of the Run 2 dataset, corresponding to all of the data recorded in 2015 and 2016 at $\sqrt{s}$ =13 TeV.

The LHCb detector is designed to study particles containing b and c quarks.

These quarks are produced dominantly via gluon interactions. The gluons typically have highly asymmetric momenta, therefore the $b\bar{b}$ quark pair is produced predominantly in the forward (or backward) direction, illustrated in Fig. 3.2. For this reason, the LHCb detector [45, 46] was designed as a single-arm forward spectrometer, as shown in Fig. 3.3. It covers the pseudorapidity range $2 < \eta < 5$, where the pseudorapidity, η, is defined as

$$\eta \equiv -\ln\left[\tan\left(\frac{\theta}{2}\right)\right] , \tag{3.1}$$

where θ is the angle between the particle's momentum vector and the beam axis. This angular region captures 25% of all $b\bar{b}$ pairs produced. The detector is described using a right-handed coordinate system, where z represents the direction of the beam into the spectrometer, x points outwards from the centre of the ring and y points upwards. The LHCb spectrometer has an angular acceptance up to 300 mrad in the horizontal plane, and 250 mrad in the vertical plane. It is composed of many sub-detectors that are each specialised for a specific role. These are the Vertex Locator (VELO), the Ring Imaging Cherenkov detectors (RICH1 and RICH2), the Tracker Turicensis (TT), the dipole magnet, the tracking stations T1-T3, the calorimeter system (SPD/PS, ECAL, HCAL) and the muon stations M1-M5. In Secs. 3.1 to 3.5, individual descriptions of these sub-detectors are presented.

3.1 The Vertex Locator

The Vertex Locator (VELO) [47] provides precise tracking close to the LHCb interaction region to identify primary and secondary vertices from heavy-flavour decays, which is essential for studies of long-lived particles such as B and D mesons. The VELO is a silicon microstrip detector situated around the pp interaction point, referred to as the primary vertex (PV). It consists of 42 silicon modules arranged along the beam, each providing a measurement of the radial coordinate, r, and azimuthal coordinate, ϕ, using so-called R sensors and Φ sensors respectively, shown in Fig. 3.4. The sensors are located 7 mm from the LHC beams at their closest points. The VELO modules are retracted 29 mm in the horizontal direction

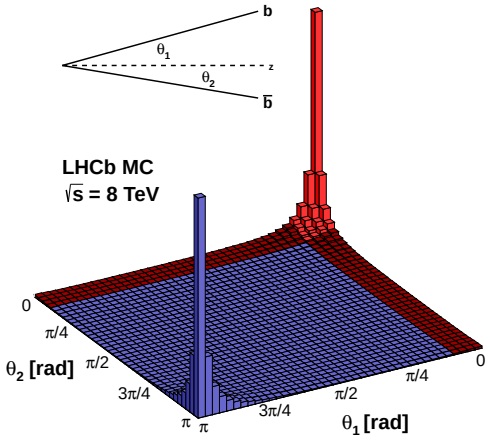

Figure 3.2: The distribution of $b\bar{b}$ quark pair productions in simulated pp collisions at 8 TeV as a function of the polar angles θ_1 and θ_2 with respect to the beam axis, z. The red shading indicates the region covered by the LHCb detector.

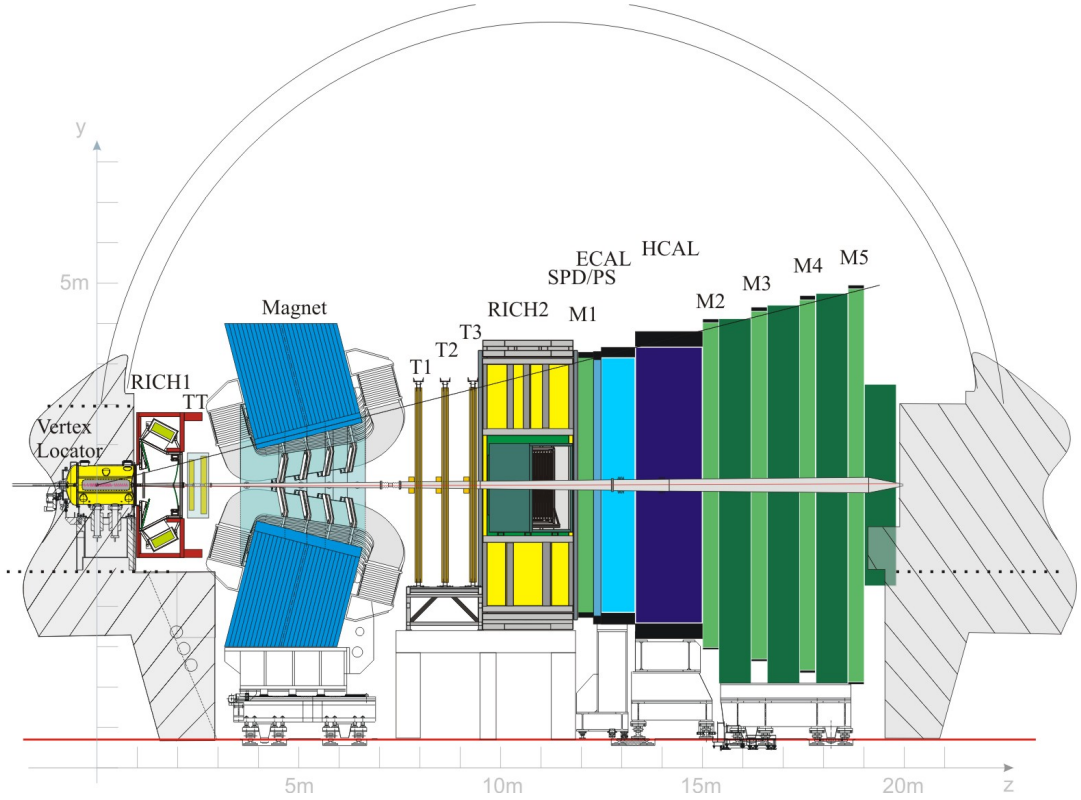

Figure 3.3: Diagram of the LHCb detector. The various sub-detectors are the Vertex Locator (VELO), the Ring Imaging Cherenkov detectors (RICH1 and RICH2), the Tracker Turicensis (TT), the dipole magnet, the tracking stations T1-T3, the calorimeter system (SPD/PS, ECAL, HCAL) and the muon stations M1-M5.

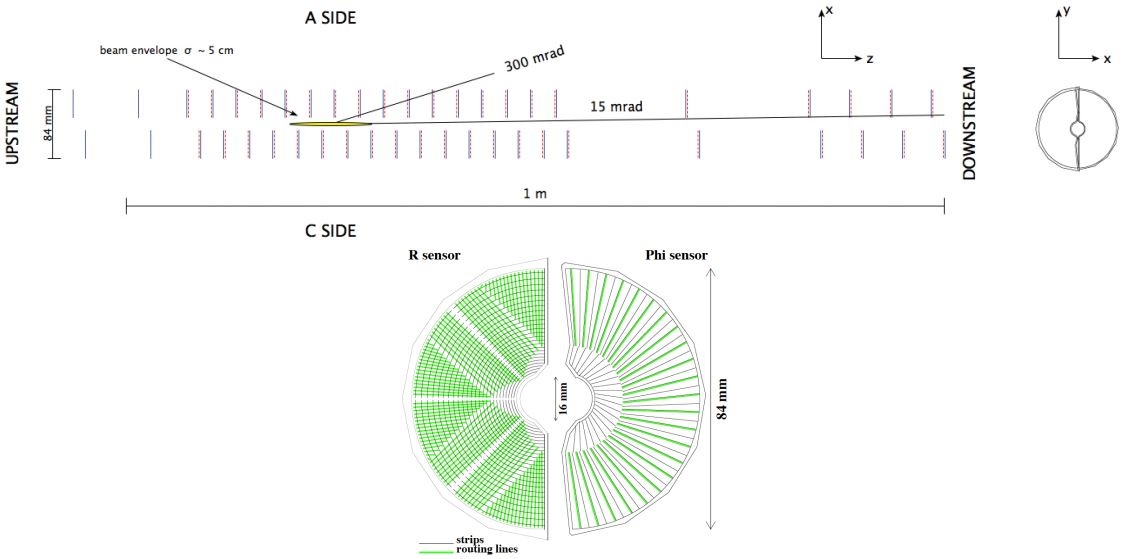

Figure 3.4: Layout of the VELO detector (top). Schematic diagram showing the R and Φ sensors (bottom). Reproduced from Ref. [46].

during injection of the LHC beams in order to reduce radiation damage and returned to their nominal position during stable beams. The sensors are enclosed in a secondary vacuum envelope which is separated from the LHC vacuum by corrugated foil sheets designed to protect the VELO modules against electromagnetic interference from the LHC beams.

The VELO has a high spatial resolution, enabling precise determination of a particle's flight direction close to the primary interaction point. The impact parameter (IP) of a track is defined as the distance between the track and the PV at the track's point of closest approach to the PV. Long-lived B and D mesons studied in this thesis have their decay vertices displaced from the PV and as such tend to have a large IP. Therefore, the performance of the VELO can be quantified by the IP resolution, which, determined from 2012 data, is less than 35 μm for particles with transverse momentum greater than 1 GeV/c [47]. The IP resolution in the x and y directions as a function of track momentum is shown in Fig. 3.5. The vertex resolution of the VELO is 13 μm in the transverse plane and 71 μm along the beam axis for vertices with 25 tracks [47].

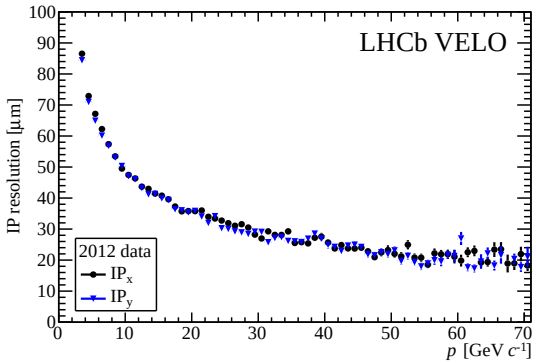

Figure 3.5: IP resolution as a function of momentum in both the x and y directions. Reproduced from Ref. [47].

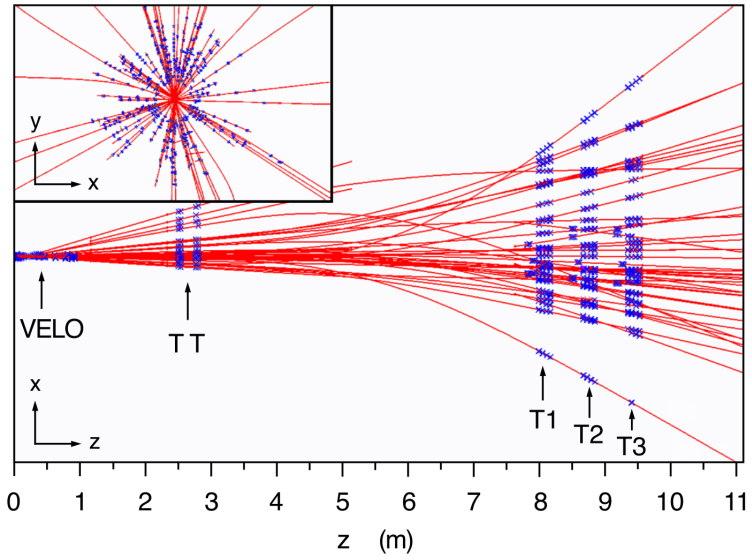

Figure 3.6: Display of the reconstructed tracks (red) and assigned hits (blue) in an event in the $x - z$ plane. The insert shows a zoom into the VELO region in the $x - y$ plane. Reproduced from Ref [46].

3.2 Tracking and magnet

The LHCb tracking system consists of the VELO and four planar tracking stations further downstream: the Tracker Turicensis (TT), made of silicon microstrips, upstream of the dipole magnet and tracking stations T1-T3 downstream of the magnet, as shown in Fig. 3.6. The tracking stations T1-T3 have an inner region (Inner Tracker, IT) consisting of the same silicon microstrips as the TT and an outer region (Outer Tracker, OT) consisting of straw tubes. Charged particles require a minimum momentum of 1.5 GeV/c to reach the tracking stations T1-T3.

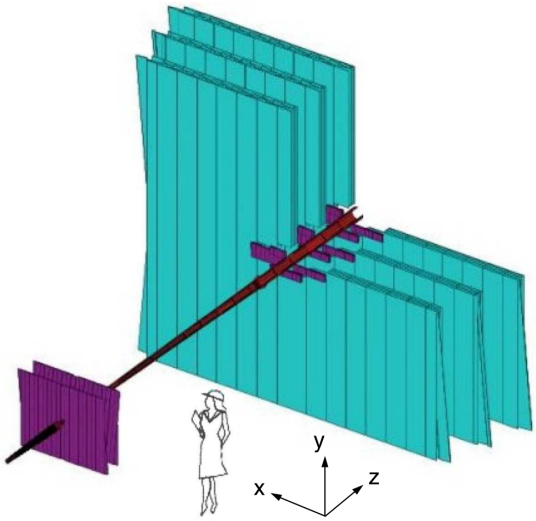

Figure 3.7: Arrangement of the layers of the IT and OT. Reproduced from Ref. [48].

The TT and IT are constructed from silicon microstrip detectors, arranged as shown in Fig. 3.7. The TT is a planar detector 150 cm wide and 130 cm high, located upstream of the dipole magnet, covering the full detector acceptance. At the centre of each of the three T-stations downstream of the magnet, the IT is arranged in a cross shape, 120 cm wide and 40 cm high, around the beam pipe. Each of the four planar tracking stations are composed of four layers of modules with the first and fourth layers mounted vertically and the second and third layers mounted at $+5^\circ$ and -5° from the vertical (rotated around the z-axis), respectively. The TT has an active area of $8.4\,\mathrm{m}^2$ and the IT has an active area of $4.0\,\mathrm{m}^2$, and both use silicon microstrip sensors with a strip pitch of about 200 µm, giving a single hit resolution of around 50 µm.

The OT is a straw drift tube detector for the tracking of charged particles and the measurement of their momentum over the full detector acceptance. The straw tubes in each station are arranged in four modules, with the same rotation of modules as in the TT and IT. Each module contains two staggered layers of drift-tubes. The total active area is approximately 6×5 mm^2 and contains approximately 55,000 single straw-tube channels, with inner diameters of 4.9 mm. The straw tubes are filled with a gas mixture containing 70% argon and 30% carbon dioxide, which guarantees a drift time below 50 ns and sufficient drift-coordinate resolution of 200 µm.

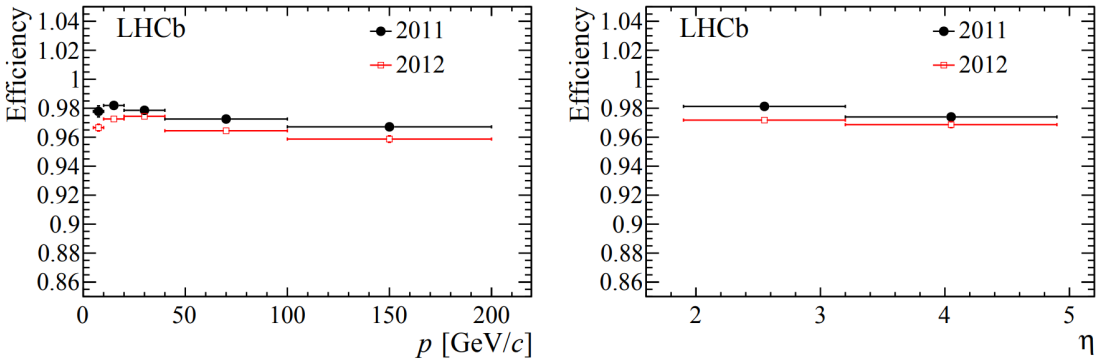

Figure 3.8: Tracking efficiency as a function of momentum, p, and pseudorapidity, η. The error bars indicate the statistical uncertainty. Reproduced from Ref. [49].

The dipole magnet, with an integrated magnetic field of about 4 Tm, enables the momentum of charged particles to be measured by bending the trajectory of charged particles in the horizontal plane. In order to achieve the required momentum resolution, the integrated magnetic field, $B = \int \mathcal{B} dl$, is measured to a precision corresponding to $\delta B/B \sim 10^{-4}$, where $\mathcal{B}$ is the magnetic field density. Since positively and negatively charged particles will bend in opposite directions, a charge detection asymmetry can result if the left and right halves of the detector have different tracking efficiencies. This would affect *CP* violation studies, such as the one described in this thesis, which involve the measurements of charge asymmetries. Hence, to minimise systematics, the magnetic field direction is reversed regularly during data-taking.

The tracking efficiency is defined as the probability that the trajectory of a charged particle that passes through the full tracking system is reconstructed. The measured tracking efficiency as a function of momentum and pseudorapidity is shown in Fig. 3.8. The average efficiency is above 96% over the momentum range 5 - 200 GeV/c and pseudorapidity range, $2 < \eta < 5$. Figure 3.9 shows the momentum resolution of reconstructed tracks, which is about 0.5% for particles below 20 GeV/c, rising to about 0.8% for particles around 100 GeV/c.

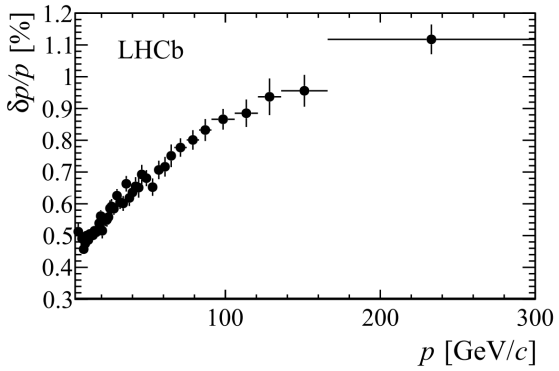

Figure 3.9: Momentum resolution as a function of momentum for tracks that have traversed the entire tracking system. Reproduced from Ref [46].

3.3 The RICH detectors

The RICH detectors (RICH 1 and RICH 2) [50] are required for the identification of charged hadrons, specifically pions, kaons and protons. The decay modes of b- and c-flavoured hadrons involve hadronic multibody final states, therefore good particle identification of hadrons over the momentum range 2 - 100 GeV/c is vital for reducing the combinatorial backgrounds. The RICH detectors utilise the idea that Cherenkov radiation is produced whenever a charged particle of velocity v, travelling through a dielectric medium of refractive index n, exceeds the speed of light in that medium, c/n. The particle produces a cone of light with an opening angle of θ_{CK} relative to the direction of the particle's propagation, given by

$$\cos\left(\theta_{CK}\right) = \frac{1}{n\beta} \text{ , where } \beta = v/c \text{ .} \tag{3.2}$$

By measuring θ_{CK} using the RICH detectors and the momentum from the magnet and tracking systems, a mass hypothesis can be determined, which provides discrimination between particle species. The relationship between Cherenkov angle and momentum for different particle species is shown in Fig. 3.10. It can be seen that the separation tends to zero as the momentum increases, as expected from Eq. 3.2, since as $\beta \to 1$, the Cherenkov angle becomes independent of particle momentum and mass. For a given dielectric medium, there is a low momentum threshold, defined when $\beta = 1/n$, where below this value of β no Cherenkov light is

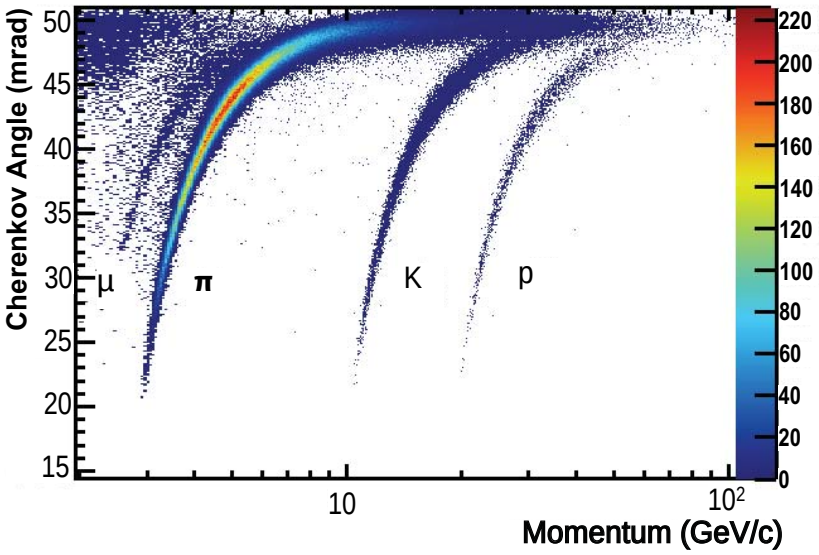

Figure 3.10: Cherenkov angle measured as a function of momentum in the RICH1 C_4F_{10} radiator for isolated tracks. The Cherenkov bands for muons, pions, kaons and protons are clearly visible. Reproduced from Ref [50].

emitted. Discrimination of lower momentum (higher mass) particles is then only possible with a dielectric medium of higher refractive index.

Two RICH detectors are used to cover the full LHCb momentum range; RICH 1 is positioned upstream of the magnet covering the momentum range 2 to 60 GeV/c, using two radiators: C_4F_{10} ($n = 1.0014$) and Aerogel ($n = 1.03$) in Run 1, although the Aerogel radiator was subsequently removed for Run 2. RICH 2 is located downstream of the magnet and covers the higher momentum range, 15 to 100 GeV/c, utilising a CF_4 radiator ($n = 1.0005$). While RICH 1 covers the full detector acceptance, RICH 2 covers a limited angular acceptance of $\sim \pm 15$ mrad to ± 120 mrad in the horizontal direction and ± 100 mrad in the vertical direction. In each RICH detector the cone of Cherenkov radiation that radiates from the charged particle is reflected by spherical focusing primary mirrors and planar secondary mirrors to project a ring onto the focal plane containing an array of Hybrid Photon Detectors (HPDs). The HPDs contain pixels of area 2×2 mm^2, which detect the single photons.

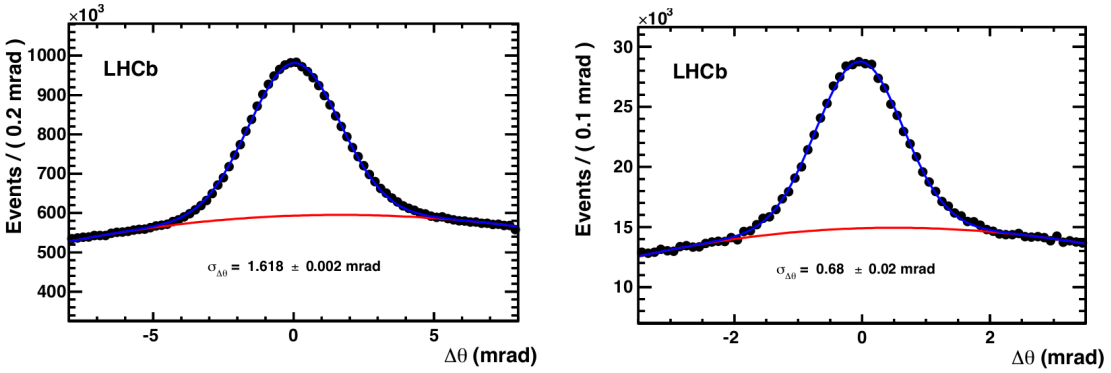

Figure 3.11: Cherenkov angle resolution using 2011 data for the RICH 1 gas (left) and RICH 2 gas (right). Reproduced from Ref [50].

One of the main measures of the RICH performance is the resolution of the Cherenkov angle from which the hit positions of the photons can be reconstructed. This is measured from the distribution of the difference between the measured and expected Cherenkov angle for each photon, $\Delta\theta$, given by $\theta_{CK} - \theta_0$, where θ_0 is the expected Cherenkov angle calculated from the momentum of the track and the refractive index of the radiator. Figure 3.11 shows an example of the distributions of $\Delta\theta$, and from these plots the Cherenkov angle resolution is determined to be (1.618 ± 0.002) mrad for C_4F_{10} in RICH1 and (0.68 ± 0.02) mrad for CF_4 in RICH2.

Although the RICH system is designed primarily to provide separation between charged hadrons (π, K and p), it can also provide some information on leptons. Similarly, the calorimeters and muon systems, described below, can provide some hadron identification. A global likelihood hypothesis for each particle type (π, K, p, e, μ) is formed by combining the particle likelihood hypotheses as determined by each sub-detector, $\mathcal{L}_X$, for particle hypothesis X. Since the most abundant particles from a pp interaction are pions, the pion hypothesis is initially assumed. For each track the differences between the log-likelihood of a particle hypothesis, X, compared to the log-likelihood of the pion hypothesis is computed:

$$DLLX = \log \mathcal{L}_X - \log \mathcal{L}_\pi \ . \tag{3.3}$$

The PID performance of hadrons can be directly determined from background-free calibration samples of protons, kaons and pions, for example, those produced in

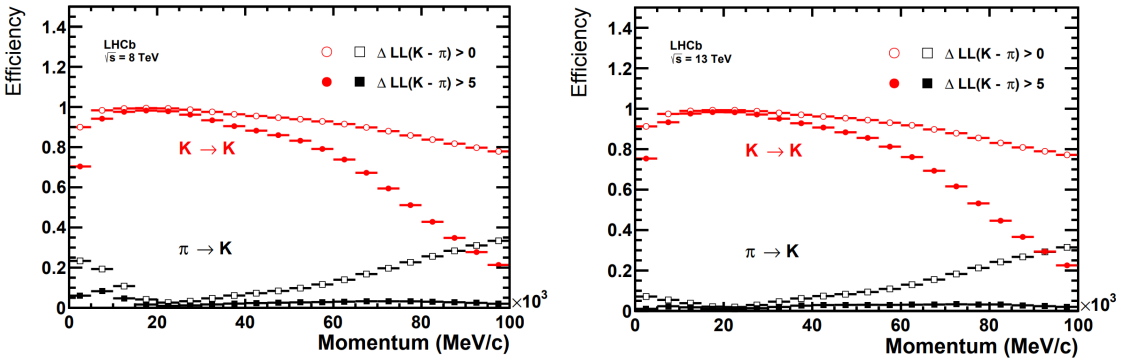

Figure 3.12: Kaon PID performance of the RICH system as a function of momentum in both Run 1 (left) and Run 2 (right), showing the efficiency to correctly identify kaons (red points) and the corresponding pion misidentification probability (black points). The expression $\Delta\mathrm{LL}(K-\pi)$ is equivalent to $\log\mathcal{L}_K - \log\mathcal{L}_\pi$, described in the text. Reproduced from Ref [51].

Λ, D^{*-} and K^0_S decays respectively. The typical kaon PID performance of the LHCb detector for both Run 1 and Run 2 is shown in Fig. 3.12. It can be seen that the overall performance of the RICH system has improved in Run 2. These improvements from Run 1 to Run 2 are both due to changes in the running conditions, for example the increase in beam energy and the change in trigger conditions, and the intrinsic performance of the RICH system, mainly from the removal of the aerogel radiator.

3.4 Calorimeters

The LHCb calorimeter system provides energy measurements and is essential for the first level of the trigger to select particles with high transverse energy. It consists of four sub-systems: the scintillating-pad (SPD) and pre-shower (PS) detectors, the electromagnetic calorimeter (ECAL) and the hadronic calorimeter (HCAL) [52]. All subsystem components provide energy measurements using the mechanism of detecting scintillation light using photomultiplier tubes (PMTs). The calorimeter system is located downstream of RICH 2, between the first two muon stations, as shown in Fig. 3.3. The ECAL is required to measure electrons and photons and the HCAL to measure charged and neutral hadrons. The SPD/PS detectors are nearest the interaction point and designed to help the ECAL with electron

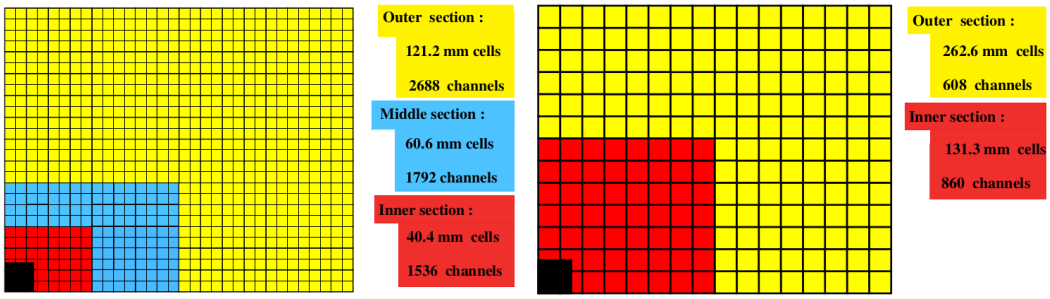

Figure 3.13: Segmentation of the SPD/PS and ECAL (left) and the HCAL (right). One quarter of the detector face is shown. Reproduced from Ref. [48].

identification. Between the SPD and PS is a 15 mm lead converter, 2.5 radiation lengths thick, to initiate showering before the PS.

The ECAL is composed of 4 mm thick alternating lead absorber and polystyrene scintillator layers with an acceptance of 300 mrad horizontally and 250 mrad vertically. The thickness of the ECAL corresponds to 25 radiation lengths, chosen to fully contain high energy photon showers for optimum energy resolution. The energy resolution of the ECAL is parameterised by $\sigma E/E = (8.5 - 9.5\%)/\sqrt{E} \oplus 0.8\%$, for energy, E, in GeV [53].

The HCAL has its scintillating tiles mounted parallel to the beam axis to increase the contact area between the scintillator tiles and optical fibres, maximising the amount of scintillation light collected. The tiles are separated by 100 mm thick iron absorber plates. Due to space limitations, the HCAL has a thickness limited to 5.6 nuclear interaction lengths. The measured energy resolution is $\sigma_E/E = (69 \pm 5)\%/\sqrt{E} \oplus (9 \pm 2)\%$ for energy, E, in GeV [53].

All four components of the calorimeter system are composed of scintillator pads with a cell granularity that decreases when moving outwards from the beam pipe, as shown in Fig. 3.13. The SPD/PS and ECAL have variable segmentation split into three sections, whereas the HCAL is split into two zones with larger cell sizes due to the larger size of hadronic showers.

3.5 Muon system

The muon system [54, 55] is designed, together with the calorimeter system, to provide initial information on whether to accept or reject the event to the first level of hardware trigger, described in Sec. 3.6. The muon system is composed of five stations, labelled M1 through to M5, each containing 276 multi-wire proportional chambers (MWPCs), except the inner-most region of M1. This region is subject to the highest level of radiation and as such contains 12 gas electron multiplier (GEM) detectors. Station M1 is located upstream from the calorimeters and is only used in the first level of trigger. Stations M2 - M5, located downstream from the calorimeters, are interleaved with 80 cm thick iron absorbers and are designed to identify and trace penetrating muons. For each muon station the segmentation size increases moving outwards from the beam pipe in four distinct regions, such that each region is subject to the same particle flux. The total active area of the muon system is 435 m^2. Muons with momenta greater than 6 GeV/c will typically traverse all five stations. The five stations together have a depth corresponding to 20 interaction lengths.

Part of the first level of trigger involves performing a stand-alone muon track reconstruction, which requires hits in all 5 muon stations and a calculation of the transverse momentum, p_{T}, of the tracks. Stations M1 to M3 have the best spatial resolution, which is used to find a rough, fast measurement of the muon p_{T} for use in the first level of the trigger. Stations M1 to M3 measure muon transverse momentum with a resolution of $\sim$20%. The muon system provides muon identification for trigger and offline reconstruction with an efficiency larger than 95% [46].

3.6 Trigger system

The LHC bunch crossing rate is nominally 40MHz, however there is insufficient processing power to read out the full detector and write every event to storage at this frequency. A dedicated trigger system [56] is therefore implemented to retain interesting events while discarding background events. Triggering occurs in two

stages: the low-level hardware trigger using momentum and transverse momentum discrimination, called the Level-0 (L0) trigger, and the high-level software trigger reconstructing the full event, including tracks, called the High Level trigger (HLT). The L0 trigger operates at the bunch crossing rate of 40MHz, reducing the event rate to 1MHz. The HLT only processes events that have passed L0, accepting events at a rate of 5kHz in 2012 (3kHz in 2011). The increase in computing resources in Run 2 meant that events pass HLT and are read out to storage at a rate of 12.5kHz.

A sequence of reconstruction algorithms and thresholds defined in the trigger to select a specific decay is called a trigger line, which returns an accept or reject decision. An event is retained only if it passes at least one trigger line in both L0 and HLT.

3.6.1 Level-0 trigger

The L0 trigger only uses information that can be quickly read out from the calorimeter or muon systems, reducing the event rate from 40MHz to 1MHz, and on an L0 accept the full detector is read out. The L0 trigger relies on the fact that the decay products of B mesons typically have high transverse momenta due to the large B mass. The L0 trigger selects high transverse energy clusters in the calorimeters resulting from hadrons, photons and electrons, and high transverse momentum muons in the muon system. The trigger also requires a maximum number of SPD hits to reject high multiplicity events which would use excessive processing time in the HLT.

The trigger creates `L0Hadron`, `L0Photon` or `L0Electron` candidates depending on which calorimeter subsystem the energy has been deposited in. Events containing at least one candidate above a fixed threshold in transverse energy (`L0Global` candidates) are accepted by the L0 trigger. The hadron trigger selects events with transverse energy, $E_{\mathrm{T}} > 3.68\,\mathrm{GeV}$ deposited in the hadronic calorimeter, whereas the electron and photon trigger selects events with $E_{\mathrm{T}} > 3\,\mathrm{GeV}$ deposited in the electromagnetic calorimeter. Candidates for `L0Muon` or `L0DiMuon` are created based on the hits in the muon systems and the transverse momentum of the candidate.

For a single muon, the muon candidate must have $p_{\mathrm{T}} > 1.76\,\mathrm{GeV}$, and for a pair of muons, the product of their transverse momentum must be above $1.6\,\mathrm{GeV}^2$ [57].

3.6.2 High Level Trigger

Events accepted by the L0 trigger are held in a buffer to be processed by the HLT, which has two stages: HLT1, performing partial event reconstruction, and HLT2, performing full event reconstruction.

For HLT1, the event rate has been reduced by the L0 trigger to 1MHz, allowing latency for the full detector then to be read out. Tracks in the VELO are reconstructed and are then used to form primary vertices using at least five tracks. VELO tracks are identified that either have a large IP, or tracks that match to hits in the muon chamber. Poor quality VELO tracks are rejected. The muon candidates have the additional requirements of high momentum (above $6\,\mathrm{GeV}/c$) and reasonable track quality (χ^2/ndf below 25). VELO tracks that are selected by their IP or as a muon candidate are reconstructed using information from the OT and IT-stations in order to determine their momentum. This process is known as forward tracking. Minimum momentum and transverse momentum constraints are applied to reduce processing time when fitting each reconstructed track using a Kalman-filter-based track fit. Successfully extended VELO tracks selected by their large IP are required to have a track χ^2 less than three [57].

In HLT2, the further reduction in event rate by HLT1 allows forward tracking to be performed on all VELO tracks with $p > 5\,\mathrm{GeV}/c$ and $p_{\mathrm{T}} > 0.5\,\mathrm{GeV}/c$. The HLT2 trigger includes lines for selecting b-hadron decays, prompt charm decays and muonic decays. A large proportion of the HLT2 bandwidth goes to topological trigger lines, which are specifically designed to target partially reconstructed b-hadron decays. Tracks are combined one-by-one requiring the distance of closest approach (DOCA) to be less than 2mm, reaching a total of two, three or four tracks, resulting in the `HLT2Topo(N)BodyBDTDecision` trigger lines, with $N = 2, 3, 4$ particles forming the secondary vertex. Selection requirements are imposed on these lines based on a multivariate Boosted Decision Tree (BDT) classifier, which

uses the sum of transverse momenta, minimum transverse momenta, invariant mass, corrected mass, DOCA, impact parameter significance and flight distance χ^2. Here corrected mass, m_{corr}, is defined as

$$m_{corr} \equiv \sqrt{m^2 + |{p_{\mathrm{T}}}^{miss}|^2} + {p_{\mathrm{T}}}^{miss} \ , \tag{3.4}$$

where ${p_{\mathrm{T}}}^{miss}$ represents the missing momentum in the transverse direction. This quantity allows for the case where not all final state particles are reconstructed. This multivariate selection is where most of the rejection power is achieved.

Events that pass HLT2 are written to storage at an event rate of 3kHz (2011), 5kHz (2012) or 12.5kHz (2015 and 2016). These events subsequently undergo the full alignment, calibration and reconstruction processing.

3.7 Reconstruction

3.7.1 Track reconstruction

Track reconstruction algorithms combine information from all hits from different sub-detectors, e.g. VELO, TT, IT and OT, to form tracks. There are five categories for track classification, shown in Fig. 3.14:

- **Long tracks** traverse the entire tracking system from the VELO to the T-stations. These tracks have the most precise momentum measurement as they have traversed all detector planes and the full magnetic field.
- **Downstream tracks** only traverse the TT and T-stations. These tracks are usually a result of long-lived particles, such as K^0_{S} mesons, decaying after the VELO.
- **Upstream tracks** traverse the VELO and TT stations before being bent out of the detector by the magnetic field due to their lower momentum.
- **VELO tracks** leave the LHCb acceptance after traversing part of the VELO. No momentum information can be obtained from these tracks due to the absence of a magnetic field in this region.

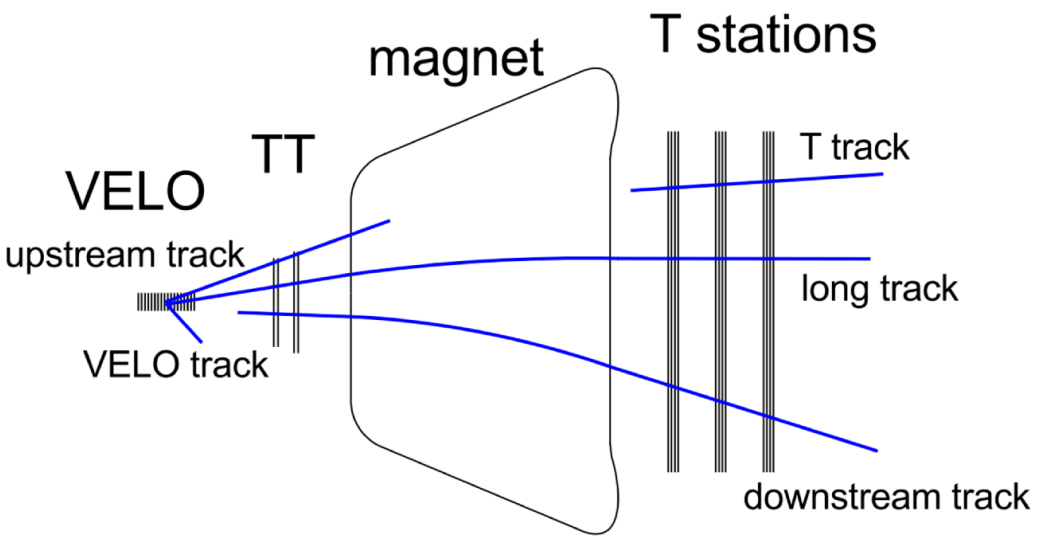

Figure 3.14: Schematic diagram of the different tracking sub-detectors (VELO, TT, T-stations) and the different categories of reconstructed tracks (long, downstream, upstream, VELO, T tracks). Reproduced from Ref. [49].

- **T tracks** are ones that only have hits in the T-stations. These are typically produced in secondary interactions.

Track reconstruction starts with the reconstruction of VELO tracks, which are then propagated through to the TT to determine the particle trajectory. To define a long track, additional hits are searched for in the T-stations that match the particle trajectory. This process finds combinations of clusters in different sub-detectors that are likely to have been formed by a single charged particle travelling though the detector. The sequence of clusters are then fit using a χ^2 minimisation procedure with a third order polynomial. Downstream tracks are reconstructed by first searching for T tracks and then finding corresponding hits upstream in the TT by extrapolating the track trajectory back through the magnetic field.

Once the tracks have been identified they are fitted to obtain a best estimate of the track parameters accounting for multiple scattering and energy lost through ionisation. The χ^2 of this fit and a neural network classifier are used to reduce the number of fake tracks that are formed by wrongly matching clusters in different sub-detectors, and therefore do not correspond to the passage of a real charged particle.

3.7.2 Stripping

The events accepted by the HLT are written to storage. All processing that occurs after this point is known as "offline" processing. The events written to storage are processed with more accurate alignment and calibration of the sub-detectors and more sophisticated reconstruction software than HLT. This offline processing stage is referred to in this thesis as "stripping". Each family of decays has its own stripping line, which refers to the reconstruction and selection of specified particles in the decay chain of interest. Various loose selection requirements are applied to remove background events to later reduce the processing time and storage requirements. An analysis initially involves taking events returned by the relevant stripping line and developing a more sophisticated selection procedure to further remove background events.

3.8 Simulation

Various simulated samples used in this thesis were generated for signal and background studies. The simulated samples are generated using the LHCb application Gauss and Boole, which are written using the Gaudi framework [58, 59]. Gauss generates particles and their decays as well as simulating the transport of charged and neutral tracks through the detector. Boole is then used to simulate the detector response [59].

In the production of simulation samples used for analysis, the first step is the production of $b\bar{b}$ pairs from pp collisions using Pythia 8 [60]. One quark in the $b\bar{b}$ pair is chosen at random to decay via user-specified process and its decay is simulated using EvtGen [61], with Photos [62] modelling any final state radiation. The transport of the decay through the detector is modelled using Geant4. Boole then returns the output in the format of real data coming from the front-end electronics. The simulated data are then processed by the trigger, reconstruction and stripping as for real data.

Both magnet polarities, and 2011, 2012, 2015 and 2016 samples are generated, with all daughter products inside the LHCb acceptance. Signal samples are simulated $B^- \to DK^{*-}$ decays to various D final states, and with the K^{*-} forced to decay to $K^0_S\,\pi^-$. For the four-body D final states, the simulated samples are produced assuming the D decay is uniform over the whole phase space. Various other samples are generated to investigate possible background decays, described in Sec. 4.1.3.

4

Selection and mass parameterisation of $B^- \to DK^{*-}$ decays

4.1 Selection of $B^- \to DK^{*-}$ candidates

In this chapter, the reconstruction and selection procedure for the signal mode $B^- \to DK^{*-}$ $(K^0_S\pi^-)$ is described, where the particles in brackets refers to the decay products of the preceding particle. The symbol D refers to a superposition of D^0 and $\overline{D}^0$ mesons. In this thesis the D^0 meson final states investigated are $K^-\pi^+$, K^+K^-, $\pi^+\pi^-$, $K^+\pi^-$, $K^-\pi^+\pi^-\pi^+$, $\pi^+\pi^-\pi^+\pi^-$, and $K^+\pi^-\pi^+\pi^-$. The π^- from the K^{*-} decay is referred to as the bachelor particle. The selection is developed for the favoured $B^- \to D(K^-\pi^+)K^{*-}$ mode and then applied with minor alterations to the other D decay modes. The data analysed correspond to 1 fb^{-1} and 2 fb^{-1} of pp collisions at $\sqrt{s} = 7$ TeV and 8 TeV collected in 2011 and 2012 (referred to as Run 1), and 1.8 fb^{-1} at $\sqrt{s} = 13$ TeV collected in 2015 and 2016 (referred to as Run 2).

4.1.1 Reconstruction and trigger requirements

$B^- \to DK^{*-}$ $(K^0_S\pi^-)$ decays are reconstructed offline and stored in a centrally produced dataset in a stage known as stripping, described in Sec. 3.7.2. At this point of the data-processing chain some loose requirements have been made in order to reduce the dataset to a reasonable size for storage. However, the amount of

combinatorial background, originating from reconstructing random pion and kaon tracks to form fake B^-, D^0, K^0_S or K^{*-} candidates, is still very high. Therefore further offline selection is applied to candidates passing the stripping and trigger requirements in order to reduce the level of combinatorial background, as well as to target specific peaking backgrounds.

The decay is reconstructed starting from the final state particles, and proceeding up the decay chain. In this case, the reconstruction proceeds with $K^0_S \to \pi^+\pi^-$, $K^{*-} \to K^0_S\pi^-$, $D^0 \to K^-\pi^+$ and finally $B^- \to DK^{*-}$; at each stage a fit is performed to the parent candidate.

The K^0_S meson is reconstructed through its decay to two charged pions. Reconstructed tracks can be classified into different types as described in Sec. 3.7.1. If the pions from the K^0_S decay leave sufficient hits in the VELO to be included in the track reconstruction they are called long tracks and the reconstructed K^0_S meson is referred to as LL. Due to the high boost from the pp collision many K^0_S particles decay outside the VELO. If the pions from the K^0_S decay do not leave sufficient hits in the VELO, they are called downstream tracks and the reconstructed K^0_S meson is referred to as DD, with the first hits being recorded in the TT, which typically results in poorer mass resolution. The LL K^0_S mesons tend to have higher combinatorial background levels as there are many more tracks in the VELO to be misreconstructed compared to further downstream. Due to these differences, the K^0_S reconstruction types, LL and DD, are treated as separate data samples and a slightly different selection is applied to each.

The K^0_S candidates are required to have a reconstructed mass within 15 MeV/c^2 of the world-average mass for LL K^0_S candidates and within 20 MeV/c^2 for DD K^0_S candidates. The K^0_S candidate is also required to have a good quality vertex that is well separated from the primary vertex. The K^{*-} candidate is formed from a reconstructed K^0_S candidate and a π^- candidate, and is required to have a reconstructed mass within 75 MeV/c^2 of the world-average K^{*-} mass. Similarly the D^0 candidate is reconstructed from the relevant kaon and pion candidates, *e.g.*, in the case of $B^- \to D(K^-\pi^+)K^{*-}$, a K^- and π^+ are reconstructed to form a D^0

candidate, which is required to form a good quality vertex, with a reconstructed mass within 25 MeV/c^2 of the world-average D^0 mass. The B^- candidate is reconstructed from a D^0 and a K^{*-} candidate forming a good quality vertex. The resulting reconstructed B^- candidate is required to have a mass in the range 4750 - 5800 MeV/c^2 and a $\chi^2_{\rm IP} < 25$, where $\chi^2_{\rm IP}$ is the difference in the vertex fit χ^2 of the PV with and without the particle under consideration. Additionally, there are loose p and $p_{\rm T}$ threshold requirements on all charged tracks.

The trigger decision for each candidate is categorised as `TOS` (Trigger On Signal) if the particles associated with the signal candidate triggered the event or `TIS` (Trigger Independent of Signal) if other particles produced in the pp interaction, that are not associated with the signal candidate, triggered the event. At the hardware trigger, the B^- candidates are required to satisfy `L0Hadron TOS` or `L0Global TIS`. At the software trigger level, B^- candidates are required to satisfy `Hlt2TopoNBodyBBDT TOS`, where $N = 2, 3$ or 4. These trigger classifications are described in Sec. 3.6.

This analysis uses variables constructed after the entire decay chain has been refitted for all the reconstructed tracks in the decay for each B^- candidate passing the stripping requirements, with one or more constraints imposed [63]. During this refit, the best fit value of the four-momenta for each particle is found under the given constraints. This procedure improves the resolution of the B^- mass peak compared to the original variables constructed without the refit performed. The B^- mass used in this analysis is constructed for each B^- candidate by fitting the tracks in the decay with requirements that the D^0 and $K^0_{\rm S}$ mass are constrained to their known values and the B^- momentum vector direction is constrained to be parallel to the vector joining the primary vertex (PV) to the B^- decay vertex.

The offline selection involves imposing requirements on individual variables, such as the reconstructed masses of the intermediate meson states, as well as using a multivariate classifier, and particle identification requirements. The requirements on the masses of the intermediate states reduce the probability of the sample containing D^0, $K^0_{\rm S}$ or K^* candidates that do not correspond to a true D^0, $K^0_{\rm S}$ or K^* meson state. However, the requirements cannot be too close to the true meson mass

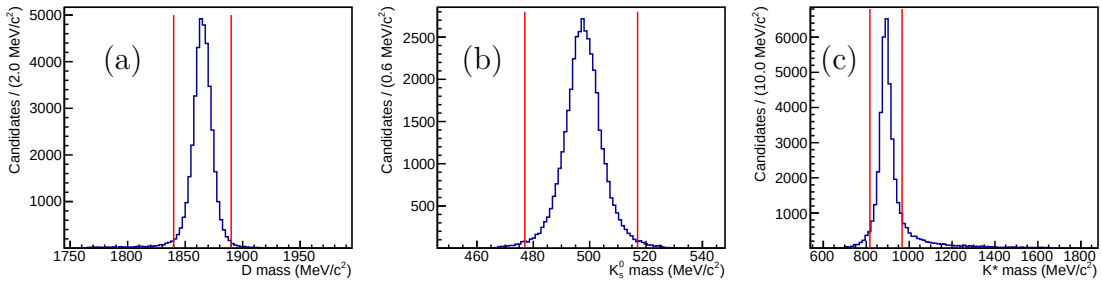

Figure 4.1: Distributions of the reconstructed masses from a simulated sample of $B^- \to D(K^-\pi^+)K^{*-}$ DD events for (a) D^0, (b) K^0_S, and (c) K^* candidates. The red lines represent the regions accepted as signal in the selection.

as this would result in the removal of a significant proportion of the signal. The signal efficiencies of the D^0, K^0_S and K^* mass requirements, shown graphically in Fig. 4.1, are 96%, 98% and 82% respectively.

After the selection described in this section has been applied, the resulting refitted B^- mass distribution is shown for Run 2 data in Fig. 4.2. The signal B^- mass peak can be clearly observed, however, in order to make accurate measurements of the signal yield in each of the D^0 modes, it is necessary to significantly reduce the combinatorial background while retaining signal events. This requires more sophisticated classification techniques. Additionally, specific backgrounds must be reduced, and particle identification requirements must be made to reduce the fraction of misidentified particles.

4.1.2 Particle identification requirements

The selection requirements are almost identical for each of the different D^0 decay modes, therefore, in order to distinguish the different modes it is essential to apply PID selection that efficiently distinguishes between pions and kaons. For both the two- and four-body D^0 decays, the suppressed D^0 decay modes may have contamination from the most favoured mode, with one or more of the D^0 daughter particles incorrectly identified. These backgrounds are called crossfeed backgrounds. The ratios of branching fractions for two- and four-body D^0 decay modes are given in Table 4.1. The contamination of the most favoured mode is considered as it

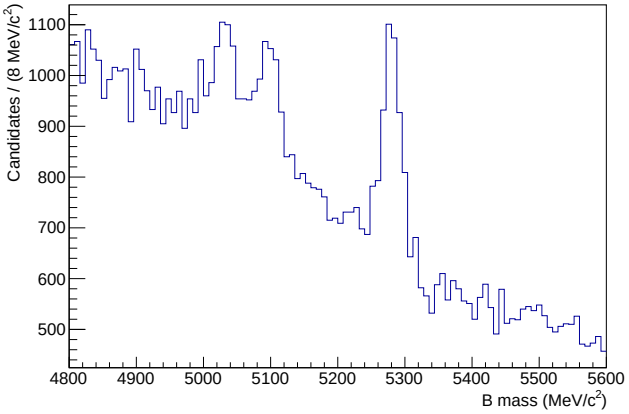

Figure 4.2: The refitted B^- mass distribution for $B^- \to D(K^-\pi^+)K^{*-}$ DD candidates in Run 2 after the stripping and mass requirements on the intermediate states. The equivalent plot for LL candidates looks similar. The B^- signal peak can be seen at the known B^- mass (5279 MeV/c^2) and the peaks at lower reconstructed B^- mass are discussed in Sec. 4.1.3.

has the largest branching fraction and therefore would have the largest crossfeed contribution in the disfavoured D^0 modes.

Mode	Branching fraction ratio
$B^- \to D(K^-\pi^+)K^{*-}$	1
$B^- \to D(K^-K^+)K^{*-}$	0.10
$B^- \to D(\pi^-\pi^+)K^{*-}$	0.036
$B^- \to D(\pi^-K^+)K^{*-}$	0.0036
$B^- \to D(K^-\pi^+\pi^-\pi^+)K^{*-}$	1
$B^- \to D(\pi^-\pi^+\pi^-\pi^+)K^{*-}$	0.092
$B^- \to D(K^+\pi^-\pi^+\pi^-)K^{*-}$	0.0036

Table 4.1: Branching fractions of the different D^0 decay modes relative to the favoured $B^- \to D(K^-\pi^+)K^{*-}$ mode [10]. The ratio given for $B^- \to D(K^+\pi^-\pi^+\pi^-)K^{*-}$ is approximate as the branching fraction has not been measured. Here it has been estimated to be the same as the ratio between the two-body favoured and suppressed modes as $r_D^{K\pi} \approx r_D^{K3\pi}$.

Consider first the two-body D^0 decay modes. The suppressed modes may all contain a background from the favoured $B^- \to D(K^-\pi^+)K^{*-}$ mode, where one or more of the D^0 daughters has been incorrectly identified. Examples can be seen in Fig. 4.3, which shows the D^0 mass spectrum for the $B^- \to D(K^-K^+)K^{*-}$ and $B^- \to D(\pi^-\pi^+)K^{*-}$ data samples both without and with PID requirements applied. Figure 4.3a (left) contains a D^0 mass peak, but to the right of this there is a second,

larger peak, which corresponds to the crossfeed from $B^- \to D(K^-\pi^+)K^{*-}$ events. This peak occurs at higher reconstructed D^0 mass due to the misidentification of the pion as a kaon, which is then added to the invariant mass sum. However, the low mass tail of this large distribution enters into the selected region of D^0 mass, with the selected region illustrated by the red lines. By applying PID requirements on the two D^0 daughter kaons, this crossfeed background can be reduced such that there is negligible contribution within the D^0 mass region, as shown in Fig. 4.3a (right).

The same effect is seen in the $B^- \to D(\pi^-\pi^+)K^{*-}$ mode, illustrated in Fig. 4.3b. In this case, the crossfeed peak is lower in invariant mass, as a pion is misidentified as a kaon. Also, the crossfeed peak in Fig. 4.3b (left) is significantly higher than in Fig. 4.3a (left), due to a much lower $D^0 \to \pi^+\pi^-$ branching fraction, as seen in Table 4.1.

The PID requirements on the daughters of the D^0 meson are designed so that no $D^0 \to hh'$ candidate can appear in more than one category with a change in mass hypothesis. A simple optimisation procedure is performed considering both the signal efficiencies and probabilities of mis-identification. For the two-body D^0 modes the requirements on the D^0 daughters are: kaons must satisfy DLLK > 2 and pions must satisfy DLLK < -2, where DLLK is defined in Sec. 3.3. These requirements have a signal efficiency of 80% on the $B^- \to D(K^-\pi^+)K^{*-}$ mode, and the probability of incorrect identification of both the kaon and the pion is 0.13%, ensuring negligible crossfeed background. Crossfeed from $B^- \to D(K^-\pi^+)K^{*-}$ events entering the $B^- \to D(\pi^-K^+)K^{*-}$ mass spectrum would require both D^0 daughters to be misidentified, therefore the resulting reconstructed D^0 mass would not be shifted overall, so fall under the signal D^0 mass peak. This is called the doubly misidentified crossfeed background. In order to reduce this background to negligible levels, the PID requirement cannot be tightened further as this would result in an unacceptable loss of signal. Therefore, a further requirement is applied to the $B^- \to D(\pi^-K^+)K^{*-}$ mode, discussed in detail in Sec. 4.1.3.

The same arguments for the two-body D^0 decays modes also apply to the four-body modes. Crossfeed backgrounds may occur in the suppressed D^0 modes

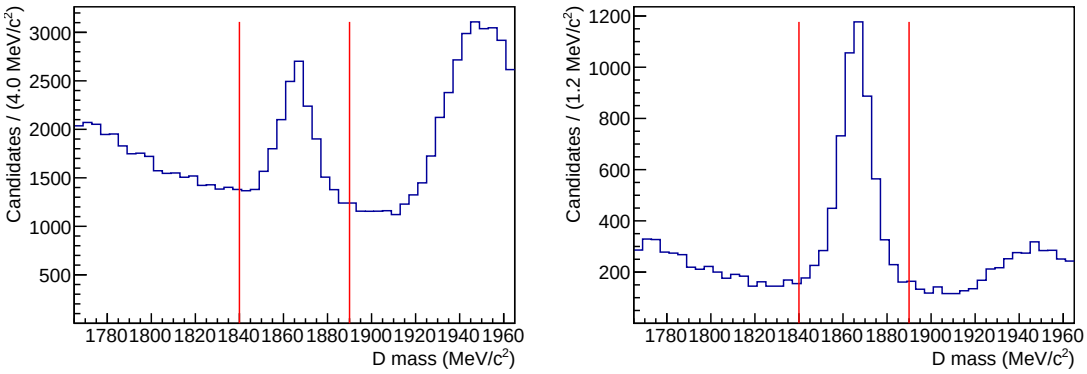

(a) $B^- \to D(K^-K^+)K^{*-}$

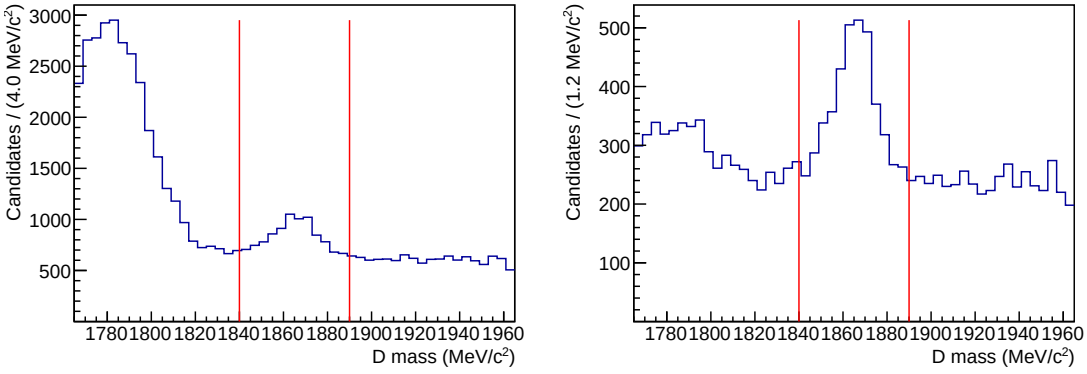

(b) $B^- \to D(\pi^-\pi^+)K^{*-}$

Figure 4.3: Reconstructed D^0 mass distributions of data after a preliminary selection with no PID selection (left) and PID selection on the D^0 daughters (right), for (a) $B^- \to D(K^-K^+)K^{*-}$ and (b) $B^- \to D(\pi^-\pi^+)K^{*-}$. The red lines indicate the position of the D^0 mass requirement in the selection; events that fall between the red lines are retained as signal events.

from misidentified $B^- \to D(K^-\pi^+\pi^-\pi^+)K^{*-}$ events. Tight PID requirements must be placed on the D^0 daughters in order to reduce these crossfeed backgrounds to negligible levels. For the $D^0 \to K^\mp\pi^\pm\pi^\mp\pi^\pm$ modes, e.g. $D^0 \to K^-\pi^+\pi^-\pi^+$, the K^- must satisfy DLLK $>$ 2 and both π^+ must satisfy DLLK $<$ -2; no PID requirement is applied for the π^- because the background $D^0 \to K^+K^-K^+\pi^-$ has a very low branching fraction [10]. These requirements have a signal efficiency of 74% on the $B^- \to D(K^-\pi^+\pi^-\pi^+)K^{*-}$ mode, and the probability of incorrect identification of both the K^- and the π^+ is 0.10%. For the $D^0 \to \pi^+\pi^-\pi^+\pi^-$ mode, the two pions that are of the same charge as the bachelor particle (the pion originating directly

from the K^{*-} decay) must satisfy DLLK < -2. No PID requirements are placed on the other pions because these decays correspond to Cabibbo suppressed backgrounds, and therefore are insignificant. The doubly misidentified crossfeed background from $B^- \to D(K^-\pi^+\pi^-\pi^+)K^{*-}$ events in the $B^- \to D(K^+\pi^-\pi^+\pi^-)K^{*-}$ mode must be investigated further in order to reduce it to negligible levels, as detailed in Sec. 4.1.3.

In addition to the correct identification of the D^0 daughters, it is also necessary to consider possible misidentification of the bachelor pion. A PID requirement is made on this bachelor pion to lower the combinatorial background and reduce the $B^- \to DK^0_S K^-$ background to negligible levels. The $B^- \to DK^0_S K^-$ background is discussed in more detail in Sec. 4.1.3. For all D^0 decay modes, the bachelor pion is required to satisfy DLLK < 4. This requirements has a signal efficiency of 96.4% when applied to the $B^- \to D(K^-\pi^+)K^{*-}$ mode, and the probability of misidentification of the bachelor pion is 7.9%. No PID requirements are placed on the K^0_S daughters as this is not necessary due to the high purity of the K^0_S meson, described in Sec. 4.1.3. The efficiencies of the PID requirements are discussed in more detail in Sec. 5.2.2.

4.1.3 Peaking backgrounds and selections used to suppress them

There are many backgrounds to be considered where certain particles in the decay chain are missed in the reconstruction process, or incorrectly identified. These effects can result in backgrounds that form peaking structures in the B^- mass spectrum, which are dangerous if they significantly affect the B^- mass spectrum. These backgrounds must either be reduced to negligible levels using targeted selection choices, or correctly modelled and included in the fit to the invariant B^- mass spectrum. This section discusses each of the peaking backgrounds individually and the strategy employed to deal with them.

Partially reconstructed $B \to D^*K^*$ decays

The main class of backgrounds in this analysis is the partially reconstructed $B \to D^*K^*$ decays, including $B^- \to (D^{*0} \to D^0[\pi^0])K^{*-}$, $B^- \to (D^{*0} \to D^0[\gamma])K^{*-}$

and $B^0 \to (D^{*+} \to D^0[\pi^+])K^{*-}$, where the particle in square brackets is not reconstructed. As each of these backgrounds involves a pion or photon being missed in the reconstruction, the reconstructed B^- mass for these backgrounds appears at lower mass than the signal peak. This background is irreducible as it is very similar to the signal, therefore these partially reconstructed backgrounds are modelled and included as components in the fit to the B^- mass spectrum, which is discussed in detail in Sec. 4.2.4.

Backgrounds of type $B^- \to K^{*-}hh'$ decays

Backgrounds that involve the same final state particles, but do not proceed via one of the intermediate state particles, are very important since they peak in the same region of B^- mass as the signal. These backgrounds need to be properly understood and reduced to negligible levels such that they do not incorrectly contribute to the estimate of the signal yield.

Charmless backgrounds are classified as B^- meson decays that do not proceed via a D^0 meson *e.g.* $B^- \to K^{*-}\pi^+\pi^-$. Such decays give peaking background under the signal region which is expected to be uniform in D^0 mass. The variable used to investigate charmless background is the flight distance (FD) significance of the D^0 candidate in the z direction. The FD significance of a particle X is defined as

$$\text{FD significance} = \frac{z_X - z_B}{\sqrt{\sigma_X^2 + \sigma_B^2}} \,, \tag{4.1}$$

where $z_{X,B}$ is the z position of the decay vertex of the X, B particle and $\sigma_{X,B}$ is the uncertainty in the z position of the X, B decay vertex. By requiring the D^0 candidate to have a larger FD significance, the probability that the events in the sample contain a true D^0 meson is increased. The charmless background is estimated by investigating the B^- mass distribution of the candidates in the data sample that have a reconstructed D^0 mass greater than 50 MeV/c^2 away from the nominal D^0 mass. These candidates are therefore very unlikely to contain a true D^0 meson. This region of D^0 mass referred to as the D^0 mass sidebands, illustrated in Fig. 4.4.

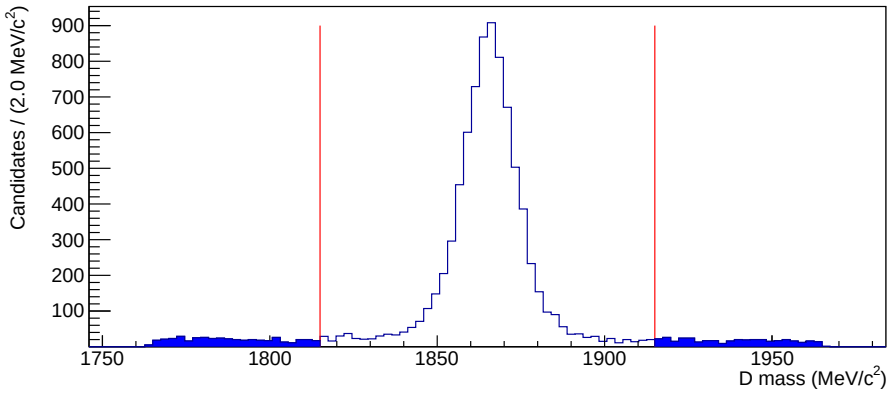

Figure 4.4: Reconstructed D^0 mass for $B^- \to D(K^-\pi^+)K^{*-}$ DD candidates with Run 1 and Run 2 samples combined. The red lines indicate the values 50 MeV/c^2 away from the nominal D^0 mass, and the bins shaded in blue represent the events that contribute to the D^0 mass sidebands. These events are expected to be dominated by charmless decays.

A simple fit is performed to the invariant B mass distribution, formed from the data in the D^0 mass sidebands, using a Gaussian to model the signal and an exponential shape to model the background. Variables that have been refitted with constraints are used in the selection, including the constraint that the D^0 is fixed to its known mass, which then favours events towards the true D^0 mass. This effectively removes the D^0 sidebands and therefore the charmless background cannot be estimated. In order to correctly estimate the background contribution in the D^0 mass sidebands, a modified selection is applied with the refitted vertex χ^2 replaced with the vertex χ^2 with no refit applied. For each D^0 decay mode, two fits are performed on data, one requiring the D^0 FD significance to be greater than zero and the other requiring it to be greater than 2, as shown in Fig. 4.5 for $B^- \to D(\pi^-\pi^+)K^{*-}$.

The fits in Fig. 4.5 give the yields of the B^- mass peak in the D^0 mass sidebands, which are subsequently scaled to provide an estimate for this background within the D^0 mass window. By being able to quantify the number of charmless events expected in the B^- mass spectrum after a given selection, it is possible to determine if the charmless background has been reduced to negligible levels.

In the final selection, the D^0 FD significance is required to exceed 2, as all charmless contributions are consistent with zero under this requirement, which retains 72% of the signal events. The expected yields of the charmless background

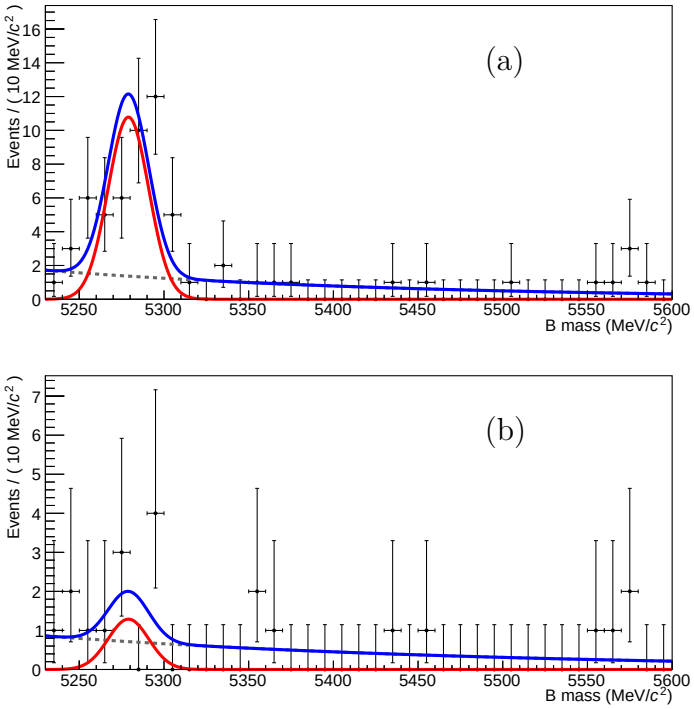

Figure 4.5: Fits, using the Run 1 data, to the refitted B mass taking $B^- \to D(\pi^-\pi^+)K^{*-}$ candidates from the D^0 mass sidebands after requiring the FD significance to be (a) greater than 0 and (b) greater than 2. A Gaussian is used to model the signal and an exponential for the combinatorial background.

in most of the two- and four-body D^0 decay modes are significantly less than 1% of the signal yield and are therefore considered negligible. However, the estimated charmless contribution in the $B^- \to D(\pi^-\pi^+)K^{*-}$ mode is greater than 1% and so could affect the measurements. The D^0 FD significance requirement is not tightened further for the $B^- \to D(\pi^-\pi^+)K^{*-}$ mode, as this would result in an extra 10% loss in signal, which is deemed unacceptable. Instead the possible charmless contribution is considered as a source of systematic uncertainty; details are given in Sec. 5.4.

$B^- \to D\pi^-\pi^+\pi^-$

Now consider backgrounds that do not proceed via a K^0_S meson. In particular $B^- \to D\pi^-\pi^+\pi^-$ decays have a branching fraction of 5.7×10^{-3} [10] (about 50 times the signal $B^- \to DK^{*-}(K^0_S(\pi^+\pi^-)\pi^-)$ branching fraction), and are expected to occur as a peaking background underneath the signal. In order to remove this background, events are selected with the requirement that the K^0_S has travelled

within the detector. For DD candidates this requirement is already satisfied, however for LL candidates a minimum requirement on the FD significance of the K^0_S meson, defined in Eq. 4.1, is used to remove this background.

The $B^- \to D\pi^-\pi^+\pi^-$ background is estimated by taking the K^0_S mass sidebands (> 20 MeV/c^2 from the nominal K^0_S mass) in data, with a modified selection applied that does not use any refitted variables, and performing a fit to the invariant B^- mass distribution, as described for the charmless background. A Gaussian is used to model the signal and an exponential for the combinatorial background. This fit is performed on $B^- \to D(K^-\pi^+)K^{*-}$ data, requiring the K^0_S FD significance to be greater than zero and 5, as shown in Fig. 4.6. Using these fits the estimated $B^- \to D\pi^-\pi^+\pi^-$ yield for Run 2 in the signal region with K^0_S FD significance > 0 is 77 ± 11 events, however with K^0_S FD significance > 5 the yield drops to 1.0 ± 1.0 events corresponding to 0.3% of the signal yield. For the final selection, the K^0_S FD significance is required to be greater than 5, for LL candidates only, as it suppresses the $B^- \to D\pi^-\pi^+\pi^-$ background to a negligible level.

Non-resonant $B^- \to DK^0_S\pi^-$

The K^{*-} meson has a large natural width (about 50 MeV/c^2 [10]) therefore $B^- \to DK^0_S\pi^-$ decays may have a non-negligible contribution in this region, which could affect the measurement of γ. The purity of the K^{*-} in the sample can be increased firstly by only accepting K^{*-} candidates that have a reconstructed mass within 75 MeV/c^2 of the known mass and secondly by exploiting the vector properties of the signal decay.

As the K^{*-} meson is a vector meson, the $B^- \to DK^{*-}$ decay is a *Scalar* $\to$ *Vector Vector* decay, forcing the K^{*-} to be longitudinally polarised due to the conservation of angular momentum. The structure of this decay can be observed using the K^0_S helicity angle, $\theta_{K^0_S}$, which is defined as the angle between the K^0_S and the B^- meson momentum in the K^{*-} rest frame, as illustrated in Fig. 4.7. This angle, $\cos(\theta_{K^0_S})$, follows a parabolic distribution for pure $B^- \to DK^{*-}$, as shown in Fig. 4.8. [1]

[1] The K^0_S helicity angle distribution is not symmetric. The asymmetry in this variable, manifest in both data and simulation, is due to the momentum and transverse momentum selections placed

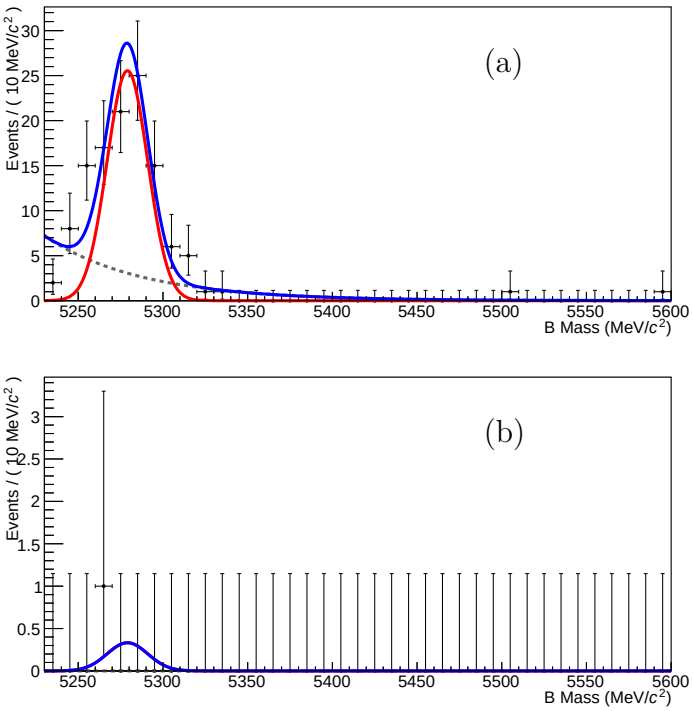

Figure 4.6: Fits to the Run 2 refitted B mass taking $D^0 \to K^-\pi^+$ candidates from the K^0_S mass sidebands after requiring the FD significance to be (a) greater than 0 and (b) greater than 5σ.

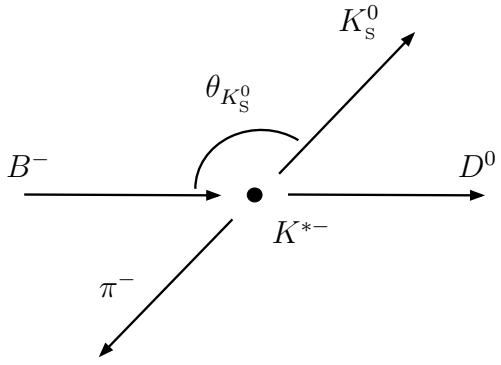

Figure 4.7: Diagram of B^- decay particles in the K^{*-} rest frame, illustrating the definition of the K^0_S helicity angle, $\theta_{K^0_S}$.

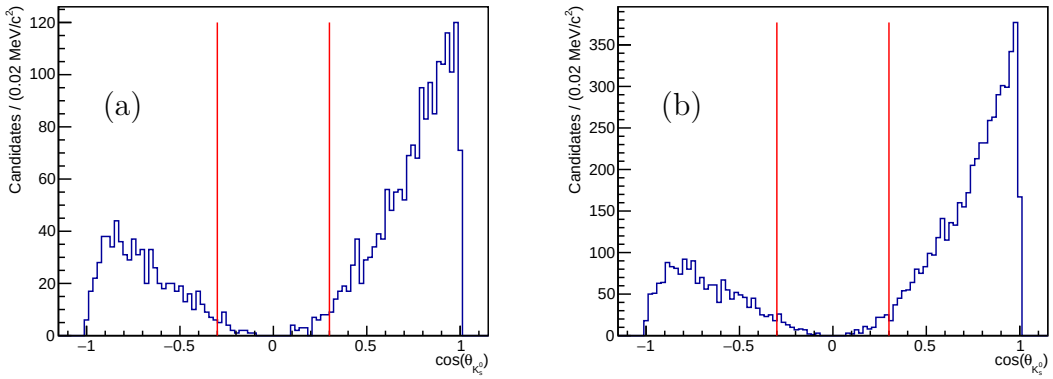

Figure 4.8: Distribution of $\cos(\theta_{K^0_S})$ from a simulated sample of $B^- \to D(K^-\pi^+)K^{*-}$ events for (a) LL candidates and (b) DD candidates. The red lines represent the region $\cos(\theta_{K^0_S})$ that is rejected in the selection.

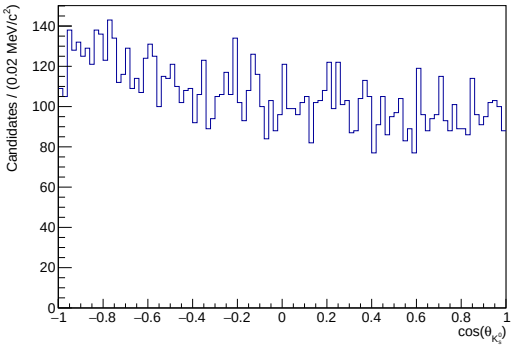

Figure 4.9: Distribution in data of the cosine of K^0_S helicity angle in $B^- \to D(K^-\pi^+)K^{*-}$ combinatorial background.

By removing candidates that have a small absolute value of $\cos(\theta_{K^0_S})$, a large amount of non-resonant $B^- \to DK^0_S\pi^-$ and combinatorial background can be removed while retaining almost all of the pure $B^- \to DK^{*-}$ signal. The combinatorial background is roughly uniform in $\cos(\theta_{K^0_S})$, as shown in Fig. 4.9. Removing events with an absolute value of $\cos(\theta_{K^0_S})$ less than 0.3 retains 97% of true $B^- \to DK^{*-}$ decays, while rejecting 30% of the combinatorial background. This $\cos(\theta_{K^0_S})$ selection would also be expected to remove 33% of the non-resonant $B^- \to DK^0_S\pi^-$ background. The optimisation of the K^{*-} mass and K^0_S helicity angle selection is discussed in Sec. 5.2.4.

on the bachelor pion at the stripping stage of the selection.

Crossfeed background

As discussed in Sec. 4.1.2, the B^- mass spectrum for the doubly Cabibbo suppressed ADS mode, $B^- \to D(\pi^-K^+)K^{*-}$, can contain background events from the favoured $B^- \to D(K^-\pi^+)K^{*-}$ mode, where the D^0 daughter mass hypotheses are swapped, i.e. the kaon is misidentified as a pion and the pion is misidentified as a kaon. When considering the two-body D^0 decay modes, the favoured $B^- \to D(K^-\pi^+)K^{*-}$ mode has a branching ratio 281 times higher than the $B^- \to D(\pi^-K^+)K^{*-}$ mode [10]. Particle identification requirements on the D^0 daughters, detailed in Sec. 4.1.2, significantly reduce this background, however in order to bring it down to negligible levels a veto must be applied. An alternative D^0 mass, $m(D_{\text{swapped}})$, is calculated where the D^0 meson is reconstructed with both daughter mass hypotheses are swapped. The applied veto requires $m(D_{\text{swapped}})$ to be greater than 15 MeV/c^2 away from the known D^0 mass. This veto is illustrated in Fig. 4.10, which shows the distributions from simulated samples for DD candidates in Run 1. Figure 4.10 (a) is the D^0 mass distribution with the correct daughter mass hypothesis, therefore this is what the $m(D_{\text{swapped}})$ distribution would look like for the doubly misidentified background. Similarly, Fig. 4.10 (b) is the D^0 mass distribution with the swapped daughter mass hypothesis, therefore this is what the $m(D_{\text{swapped}})$ distribution would look like for the signal. The veto removes 91.2% of doubly misidentified background, corresponding to events that lie within the red lines in Fig. 4.10 (a), while maintaining a 92.5% signal efficiency, corresponding to events that lie outside the red lines in Fig. 4.10 (b). The two-body veto is only applied to the $B^- \to D(\pi^-K^+)K^{*-}$ mode in this analysis.

For the four-body modes, the equivalent background can appear in the suppressed $B^- \to D(K^+\pi^-\pi^+\pi^-)K^{*-}$ mode due to contamination from the favoured $B^- \to D(K^-\pi^+\pi^-\pi^+)K^{*-}$. In this case, there are two π^+ mesons that could be misidentified as a K^+ meson, therefore two vetos are applied. The two possible alternative D^0 masses are reconstructed as a swapped mass hypothesis, one where the kaon is swapped with the lower momentum pion, $m(D^{\text{low p}}_{\text{swapped}})$, and the other where the kaon is swapped with the higher momentum pion, $m(D^{\text{high p}}_{\text{swapped}})$. The veto

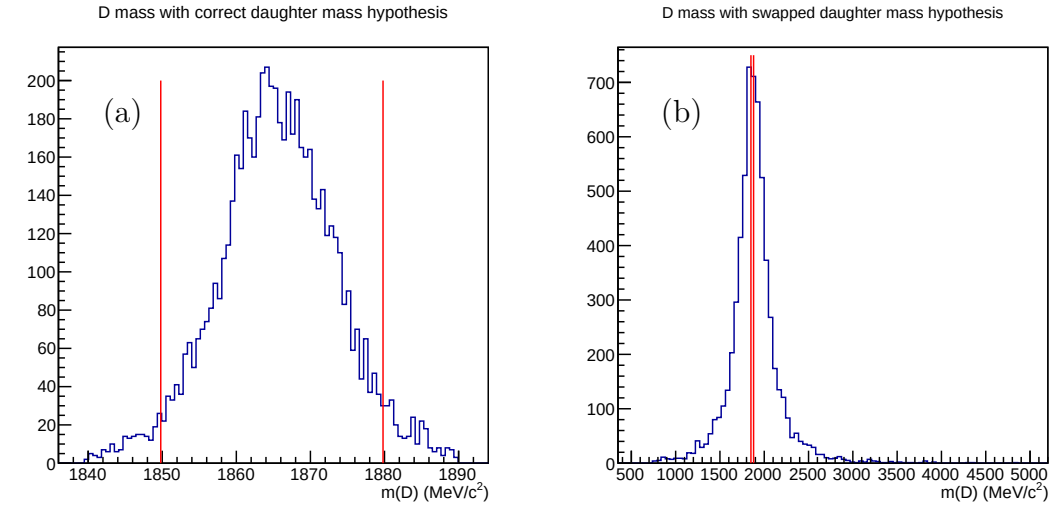

Figure 4.10: Distributions from simulated samples of DD candidates in Run 1 showing D^0 mass with (a) the correct D^0 daughter mass hypothesis and (b) the swapped D^0 daughter mass hypothesis. Events within the red lines correspond to those removed by the double misidentification veto applied to the $B^- \to D(\pi^- K^+)K^{*-}$ mode.

is applied to both these reconstructed masses as demonstrated in Fig. 4.11. The four-body veto is only applied to the $B^- \to D(K^+\pi^-\pi^+\pi^-)K^{*-}$ mode in this analysis.

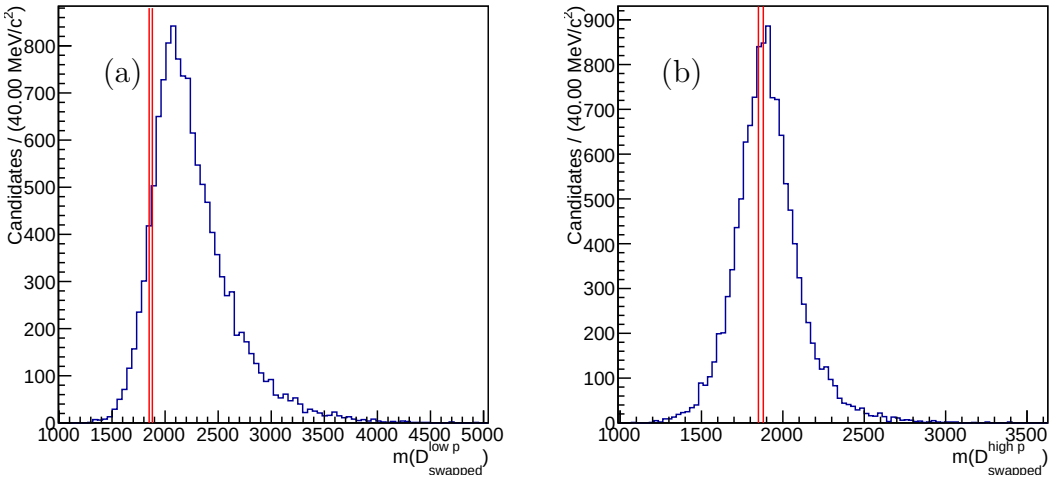

Figure 4.11: Distributions from simulated samples of DD candidates in Run 2 showing the swapped D^0 daughter mass hypothesis where (a) the kaon is swapped with the lower momentum pion and (b) the kaon is swapped with the higher momentum pion. Events within the red lines correspond to those removed by the double misidentification veto to the suppressed $B^- \to D(K^+\pi^-\pi^+\pi^-)K^{*-}$ mode.

In addition to the double misidentification veto, the selection requirement on the reconstructed D^0 mass and the PID requirements, discussed in Secs. 4.1.1 and 4.1.2,

	Run 1	Run 2
LL	9.5×10^{-3}	5.6×10^{-3}
DD	6.5×10^{-3}	5.3×10^{-3}

Table 4.2: The proportion $B^- \to D(K^-\pi^+)K^{*-}$ events expected in the B^- mass spectrum of the suppressed $B^- \to D(\pi^-K^+)K^{*-}$ mode relative to the total $B^- \to D(\pi^-K^+)K^{*-}$ signal yield.

	Run 1	Run 2
LL	2.7×10^{-3}	1.4×10^{-3}
DD	1.0×10^{-3}	6.3×10^{-4}

Table 4.3: The proportion $B^- \to D(K^-\pi^+\pi^-\pi^+)K^{*-}$ events expected in the B^- mass spectrum of the suppressed $B^- \to D(K^+\pi^-\pi^+\pi^-)K^{*-}$ mode relative to the total $B^- \to D(K^+\pi^-\pi^+\pi^-)K^{*-}$ signal yield.

both help to reduce the crossfeed background. In order to determine the overall crossfeed contamination in the suppressed $B^- \to D(\pi^-K^+)K^{*-}$ mode, the efficiency of the D^0 mass window, double misidentification veto and PID requirements are taken into account for both the normal and swapped D^0 mass hypotheses. Tables 4.2 and 4.3 show the expected proportion of crossfeed events in both the two- and four-body ADS modes, relative to the signal. These results show that the crossfeed background is negligible at less than 0.1% of the signal.

$\Lambda_b^0 \to \Lambda_c^+ K^*$ background in the $B^- \to D(K^-K^+)K^{*-}$ mass spectrum

An additional source of background in the $B^- \to D(K^-K^+)K^{*-}$ mass spectrum comes from the decay $\Lambda_b^0 \to \Lambda_c^+(pK^-\pi^+)K^{*-}$, where the proton is misidentified as K^+ and the π^+ is missed in the reconstruction. The decay mode $\Lambda_c^+ \to pK^-\pi^+$ accounts for over 6% of the Λ_c^+ branching fraction [10], whereas Λ_c^+ decays that may contribute as background to the other D^0 decay modes, e.g. $\Lambda_c^+ \to p\pi^-\pi^+$, are suppressed by an order of magnitude. Therefore, the Λ_b^0 background is only considered for the $B^- \to D(K^-K^+)K^{*-}$ decay model.

As the $\Lambda_b^0 \to \Lambda_c^+(pK\pi)K^{*-}$ and $B^- \to D(K^-K^+)K^{*-}$ decays have similar topologies, the selection efficiencies are expected to be similar, with the exception of the requirement on the reconstructed D^0 mass, which significantly reduces this background. Additionally, the background is slightly reduced by the PID

requirements on the D^0 daughters, as the proton has to be incorrectly identified as a K^+ meson. Taking these considerations into account, the Λ_b^0 background is expected to contribute O(1) event to the $B^- \to D(K^-K^+)K^{*-}$ mass spectrum, discussed in Sec. 5.1.3. The PID requirements on the D^0 daughters cannot be increased to ensure this background is reduced to negligible levels, due to the effect on the signal efficiency. Therefore, in order to account for the Λ_b^0 background, it is modelled and included as a component to the fit, discussed in Sec. 5.1.3.

$B_s^0 \to \bar{D}^0 \bar{K}^*(1410)^0$ background

The decay $B_s^0 \to \bar{D}^0 \bar{K}^*(1410)^0$, $\bar{K}^*(1410)^0 \to K^*(892)^- \pi^+$, where the π^+ is missed in reconstruction is a possible background contribution. The branching fraction of this mode is similar to that of the signal and the same particles are present, therefore this background could be significant. Due to this background having the favoured mode corresponding to the combination of $\bar{D}^0$ and K^{*-}, it is considered as a contribution in the ADS mode. As the reconstruction of this background in the ADS mode requires the π^+ meson to be missed, the reconstructed B^- mass would fall in a region just below the signal peak. The fit used to extract the *CP* observables has a lower mass limit of $5230\,\mathrm{MeV}/c^2$, therefore this background will be almost entirely removed. However, it is possible that a small contribution still remains in the signal region.

The $B_s^0 \to \bar{D}^0 \bar{K}^*(1410)^0$ background contribution can be estimated from its branching fraction, $(3.9 \pm 3.5) \times 10^{-4}$ [10], and its efficiency through the $B^- \to DK^{*-}$ selection. Due to the similar topologies of the signal and background decays, the selection efficiency of the $B_s^0 \to \bar{D}^0 \bar{K}^*(1410)^0$ is taken to be the same as for $B^- \to DK^{*-}$, except for the efficiency of the requirement that the B^- mass must be above $5230\,\mathrm{MeV}/c^2$, given by $\epsilon_{B_s^0}(B\ mass\ > 5230\,\mathrm{MeV}/c^2)$. This assumption allows an estimate for the upper limit of the background contribution as a fraction of the signal yield, given by

$$\frac{N(B_s^0 \to \overline{D}^0 \bar{K}^*(1410)^0)}{N(B^- \to DK^{*-})} = \frac{\mathcal{B}(B_s^0 \to \overline{D}^0 \bar{K}^*(1410)^0)}{\mathcal{B}(B^- \to DK^{*-})} \times \frac{\epsilon_{B_s^0}(B\ mass\ > 5230\,\mathrm{MeV}/c^2)}{\epsilon_{B^-}(B\ mass\ > 5230\,\mathrm{MeV}/c^2)}\ . \quad (4.2)$$

In order to calculate the efficiency, $\epsilon_{B_s^0}(B\ mass\ > 5230\,\mathrm{MeV}/c^2)$, a simulated sample of $B_s^0 \to \overline{D}^0 \bar{K}^*(1410)^0$, $\bar{K}^*(1410)^0 \to K^*(892)^- \pi^+$ events is generated, where the π^+ is missed in reconstruction. The efficiency for the B^- mass being greater than $5230\,\mathrm{MeV}/c^2$ is found to be 6.4×10^{-4}.

The calculation using Eq. 4.2 gives an upper limit estimate of the background yield as a fraction of the ADS signal yield of $(1.28 \pm 1.26) \times 10^{-3}$ above 5230 MeV. This estimated B_s^0 background is used to assign a systematic uncertainty to the *CP* observables, discussed in Sec. 5.4.

Lambda contamination

The $K_S^0 \to \pi^+\pi^-$ decay could have contamination coming from $\Lambda \to p\pi^-$, where the proton is reconstructed as a pion. In order to distinguish between K_S^0 decays and Λ contamination, the Armenteros-Podolanski (AP) plot is used [64]. The transverse momentum of the daughters with respect to the mother particle, p_T, is plotted as a function of the longitudinal momentum asymmetry, defined as

$$\frac{p_L^+ - p_L^-}{p_L^+ + p_L^-}\ , \quad (4.3)$$

where $p_L^\pm$ is the longitudinal momentum of the positive (negative) daughter particles with respect to the direction of the mother. The decay products of the $K_S^0 \to \pi^+\pi^-$ decay have the same mass and therefore on average their momenta is symmetrically distributed. For the $\Lambda \to p\pi^-$, the proton would, on average, take a larger proportion of the momentum resulting in an asymmetric distribution. Contamination from Λ baryons would be clearly seen as a distinct structure on the AP plot, as illustrated in Fig. 4.12.

The resulting AP plots from this analysis for both data and simulation are shown in Fig. 4.13. The curves are the same shape as the expected distribution

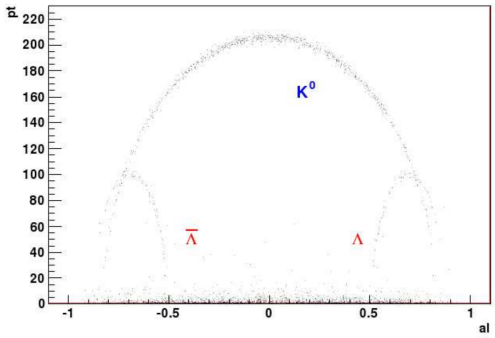

Figure 4.12: An example Armenteros-Podolanski plot showing where the signal regions for K^0_S, Λ and $\overline{\Lambda}$ are located in the AP plane. Reproduced from Ref. [64]. The *pt* label on the y axis refers to the transverse momentum of the daughters with respect to the mother particle and the *al* on the x axis refers to the longitudinal momentum asymmetry, defined in Eq. 4.3.

for a sample of pure K^0_S mesons. Therefore, no contamination from $\Lambda \to p\pi^-$ decays is observed in the data.

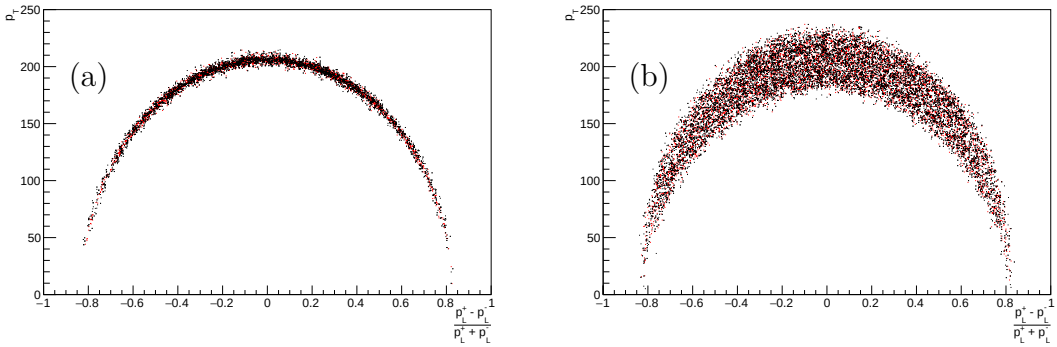

Figure 4.13: Armenteros-Podolanski plots for both data (black) and simulation (red) for (a) LL, and (b) DD candidates. The p_T values on the y axis are the transverse momentum of the daughters with respect to the mother particle and the x axis is the longitudinal momentum asymmetry, defined in Eq. 4.3.

$B \to DK^0_S K$ background

The decay $B^- \to DK^0_S K^-$ has a branching fraction of 5.5×10^{-4} [10], which is similar to the signal $B^- \to DK^{*-}(K^0_S\pi^-)$ branching fraction. However, nearly all of this background is removed by the requirements that the reconstructed K^{*-} mass must be within 75 MeV/c^2 of the known K^* mass and the DLLK of the bachelor pion must be less than four. This PID requirement suppresses the background to

about 8%. The efficiency of the K^{*-} mass selection when applied to the simulated $B^- \to DK^0_S K^-$ samples is 3% for both LL and DD. This gives the expected contribution of $B^- \to DK^0_S K^-$ background in the $B^- \to D(K^-\pi^+)K^{*-}$ mass spectrum to be less than 1% of the signal, therefore the background is considered negligible. Any residual amount is investigated alongside the systematics for the residual low mass background in this region.

4.1.4 Multivariate analysis with a Boosted Decision Tree

Various selection requirements are placed on individual variables relating to particles in the decay chain in order to reduce specific background contributions. However, to achieve a much lower combinatorial background while retaining signal events requires more sophisticated classification techniques. As many variables are correlated with one another, the ability to separate signal from combinatorial background can be improved by using a multivariate analysis (MVA) method, which exploits correlations between the variables.

The MVA implemented in this analysis is a Boosted Decision Tree (BDT) [65]. Decision trees take a given set of variables from signal and background training samples and construct an algorithm to decide whether a given event corresponds to signal or background. Firstly, the best combination of variable and value is found to split events into two subsets in order to maximise separation signal and background. This process is then repeated with a different variable for each of the two subsets. Further repetitions of this process occur in order to build a tree, where the nodes at the end are called leaves, as illustrated in Fig. 4.14. If more than half of the weight of a leaf corresponds to signal, it is a signal leaf, where each event is given a value of +1, otherwise it is a background leaf, where each event is given a value of -1. Signal events on a background leaf and background events on a signal leaf are deemed misclassified. In order to stabilise this process, many trees are built to construct a weighted average over all the trees. After each tree is built, the misclassified events are reweighted (boosted) and a new tree is build with the reweighted events. The boosting makes misclassified events more

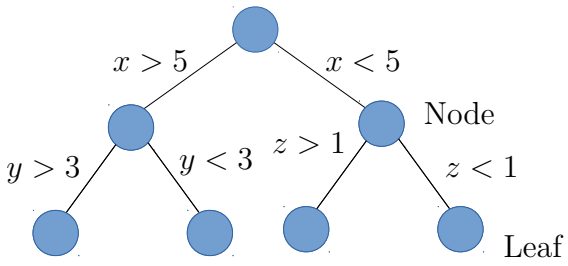

Figure 4.14: Schematic diagram of a decision tree, where x, y, and z represent variable names.

likely to be correctly classified in future trees; a particular type of boosting, called gradient boost, is used in this analysis. The result of the process assigns each event a weight from -1 (most background-like) to +1 (most signal-like).

Training samples

A BDT with the gradient boost (BDTG) method using the Toolkit for Multivariate Analysis (TMVA) framework [66] is employed in order to reduce the combinatorial background level. A separate BDT is trained for LL and DD candidates, named BDTG_LL and BDTG_DD respectively. The BDTs are mainly based on topological variables, so are insensitive as to whether the D^0 daughters are kaons or pions. Therefore, the same BDT is used for all of the two-body D^0 decay modes, trained using $B^- \to D(K^-\pi^+)K^{*-}$ decays, and another BDT is used for all the four-body D^0 decay modes, trained using $B^- \to D(K^-\pi^+\pi^-\pi^+)K^{*-}$ decays.

For the two body modes, simulated samples for the decay $B^- \to D(K^-\pi^+)K^{*-}$ are used to provide a signal sample. Events from data in the favoured $B^- \to D(K^-\pi^+)K^{*-}$ mode in the region of B^- mass above 5600 MeV are used as a sample of background combinatorial events. Generation of simulated events is computationally expensive. A small simulated sample is produced from full LHCb simulation in order to determine efficiencies. The sample is small due to the mode having very low efficiency, so many generated events fail the reconstruction. However, BDT training requires a significantly larger sample, and the available resources are insufficient to simply generate more events. A work-around is employed to remove events, which are less likely to pass the selection, at generator level. Events

are removed on the basis of low momentum or transverse momentum of signal tracks or intermediate particles. This reduces the number of events required to be simulated in the LHCb detector, which is the most computationally expensive part of the reconstruction process. The advantage of this approach is that 89% of generated events are removed, significantly reducing the resource requirement. However, the disadvantage is that the selection has to be more stringent than the final selection and 20% of events that would have passed are removed. Therefore, the BDT may not be as optimal as it may have been with unlimited resources, however this trade-off is deemed acceptable given the BDTs high performance, as discussed later in this section.

For $B^- \to D(K^-\pi^+\pi^-\pi^+)K^{*-}$, signal samples of simulated events for the decay without any selection requirements at generator level are used. This is possible due to an artifact of the time that each stage of the analysis was performed; at this later time the resource availability improved. Events from data in the favoured $B^- \to D(K^-\pi^+\pi^-\pi^+)K^{*-}$ mode in the region of B^- mass above 5600 MeV are used as a sample of background combinatorial events. All samples used in training the BDTs are split into a training and testing sample before being used as an input to the multivariate algorithm.

Setup and implementation of the multivariate algorithm

Initial selection requirements are applied to both the signal and background training samples to remove candidates that would not pass the final selection. This allows a more accurate discrimination between signal and background in data. The selection criteria on the training samples are:

- The χ^2 of the decay chain refit per degree of freedom, χ^2_{refit}, must lie between 0 and 100,
- The χ^2_{IP} of the B^- candidate, with respect to the B^- vertex, must lie between 0 and 25,

- The reconstructed K^{*-} mass must lie within 500 MeV/c^2 of the known K^{*-} mass,

- The reconstructed K^0_S mass must lie with 15 MeV/c^2 of the known K^0_S mass for LL candidates and 20 MeV/c^2 for DD candidates.

These selection requirements are looser than those applied to the full selection, discussed in Sec. 4.1.1. For example, here no requirement is imposed on the reconstructed D^0 mass and the K^{*-} mass requirement is as wide as 500 MeV/c^2 rather than the 75 MeV/c^2 used in the full selection. This is because the training samples required for the BDT must be large enough for the multivariate algorithm to distinguish between important differences in the signal and background samples rather than statistical fluctuations in the distributions. Imposing a tighter selection is found to reduce the size of the samples to a point where the BDTs would be sub-optimal.

Various input variables are used to exploit the topologies of the two- and four-body decays. Of particular importance are the χ^2_{refit} and the p_T asymmetry between the B^- candidate and other tracks from the same PV, defined as

$$A_{p_{\text{T}}} = \frac{p_T^B - p_T^{\text{cone}}}{p_T^B + p_T^{\text{cone}}} \ , \tag{4.4}$$

where p_T^B is the p_T of the reconstructed B^- signal candidate and p_T^{cone} is the sum of the p_T of all other tracks in a cone of radius 1.50 radians surrounding the B^- candidate. This is a quantitative measure of the isolation of the B^- candidate. Some of the variables are transformed using a logarithm function to increase their separation power. Other input variables used include the logarithm of the χ^2_{IP} for the B^-, bachelor, D^0 and all the D^0 decay products, the logarithm of the χ^2_{IP} for the K^0_S and both its decay products (for LL only) and the p_T of the K^0_S candidate (for DD candidates only). The variables used in the BDT are slightly different for LL and DD candidates since the separation power of the K^0_S variables significantly differs between these samples.

Rank	Variable in BDT_LL	Variable in BDT_DD
1	$\log(\chi^2_{\text{refit}})$	$\log(\chi^2_{\text{refit}})$
2	$\log(K^0_S\ \chi^2_{\text{IP}})$	$\log(D^0$ daughter kaon $\chi^2_{\text{IP}})$
3	$\log(\max\ K^0_S$ daughter $\chi^2_{\text{IP}})$	$\log($Bachelor $\chi^2_{\text{IP}})$
4	A_{p_T}	A_{p_T}
5	$\log(D^0$ daughter kaon $\chi^2_{\text{IP}})$	$\log(D^0$ daughter pion $\chi^2_{\text{IP}})$
6	$\log($Bachelor $\chi^2_{\text{IP}})$	$\log(D^0\ \chi^2_{\text{IP}})$
7	$\log(D^0\ \chi^2_{\text{IP}})$	$\log(B^-\ \chi^2_{\text{IP}})$
8	$\log(\min\ K^0_S$ daughter $\chi^2_{\text{IP}})$	$K^0_S\ p_T$
9	$\log(D^0$ daughter pion $\chi^2_{\text{IP}})$	-
10	$\log(B^-\ \chi^2_{\text{IP}})$	-

(a) Input variables for the two-body BDTs.

Rank	Variable in BDT_LL	Variable in BDT_DD
1	$\log(\chi^2_{\text{refit}})$	$\log(\chi^2_{\text{refit}})$
2	$\log(K^0_S\ \chi^2_{\text{IP}})$	A_{p_T}
3	A_{p_T}	$\log(B^-\ \chi^2_{\text{IP}})$
4	$\log(B^-\ \chi^2_{\text{IP}})$	$\log($Bachelor $\chi^2_{\text{IP}})$
5	$\log(D^0\ \chi^2_{\text{IP}})$	$K^0_S\ p_T$
6	$\log(D^0$ daughter kaon $\chi^2_{\text{IP}})$	$\log(D^0\ \chi^2_{\text{IP}})$
7	$\log($Bachelor $\chi^2_{\text{IP}})$	$\log(\max\ D^0$ daughter $\chi^2_{\text{IP}})$
8	$\log(\min\ D^0$ daughter $\chi^2_{\text{IP}})$	$\log(D^0$ daughter ss $\chi^2_{\text{IP}})$
9	$\log(\max\ K^0_S$ daughter $\chi^2_{\text{IP}})$	$\log(D^0$ daughter kaon $\chi^2_{\text{IP}})$
10	$\log(D^0$ daughter ss $\chi^2_{\text{IP}})$	$\log(\min\ D^0$ daughter $\chi^2_{\text{IP}})$
11	$\log(\min\ K^0_S$ daughter $\chi^2_{\text{IP}})$	-
12	$\log(\max\ D^0$ daughter $\chi^2_{\text{IP}})$	-

(b) Input variables for the four-body BDTs.

Table 4.4: List of input variables for the (a) two-body, and (b) four-body, BDTs, ranked by separation power. The variable A_{p_T} represents the p_T asymmetry as defined in Eq. 4.4 and "max (min) K^0_S daughter χ^2_{IP}" refers to the χ^2_{IP} of the K^0_S daughter which has the largest (smallest) χ^2_{IP}. For the four-body BDTs, the particle name "D daughter ss" refers to the pion from the D^0 meson which has the same sign as the kaon.

Tables 4.4a and 4.4b show the list of input variables in the two and four-body BDTs respectively, ranked by separation power. The distributions of the two-body BDT input variables in the signal and background training samples are shown in Figs. 4.15 and 4.16. The equivalent distributions of the input variables for the four-body BDT are shown in Appendix A. Other variables and different setups of testing and training samples were investigated but found to have negligible improvement.

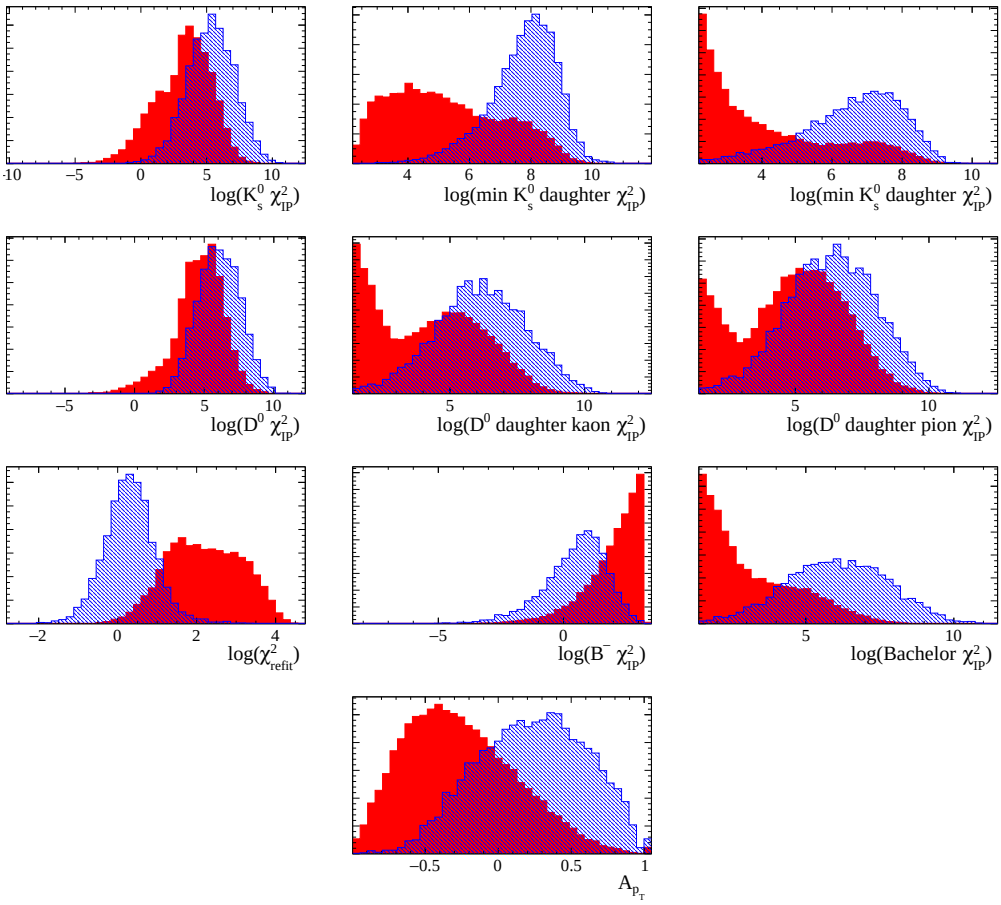

Figure 4.15: Distributions of the input variables using the signal (blue) and background (red) training samples for the two-body LL BDT. The variable $A_{p_{\mathrm{T}}}$ represents the p_{T} asymmetry as defined in Eq. 4.4 and "max (min) K^0_{S} daughter χ^2_{IP}" refers to the χ^2_{IP} of the K^0_{S} daughter which has the largest (smallest) χ^2_{IP}. All distributions have been normalised to unity in order to easily compare their shape, therefore the vertical axis is not labelled as it is not of interest here.

Performance of the multivariate algorithm and choice of working point

Selections are optimised for minimising the uncertainty in the *CP* observables. This method requires the full fit and is described in Sec. 5.2.4. The final BDT requirements chosen, based on this optimisation, are given in Table 4.5. The corresponding signal and background efficiencies in the two- and four-body D^0 decay modes are given in Table 4.6. The performance of the two- and four-body BDT for the LL and DD categories are very similar, with signal efficiency above 90% and background efficiency of less than 6%.

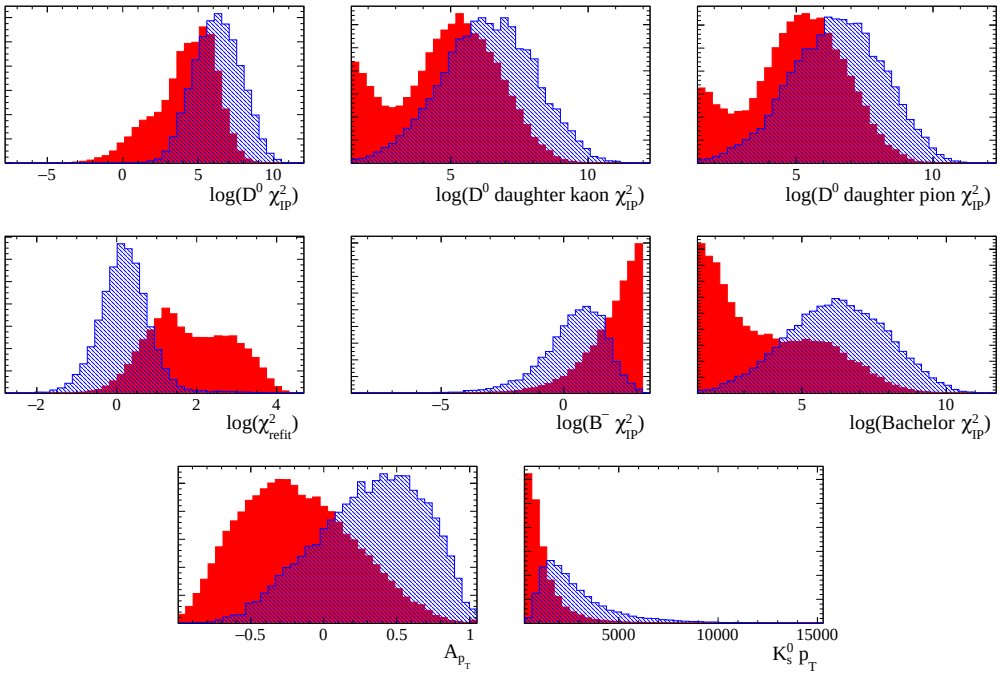

Figure 4.16: Distributions of the input variables using the signal (blue) and background (red) training samples for the two-body DD BDT. The variable $A_{p_{\mathrm{T}}}$ represents the p_{T} asymmetry as defined in Eq. 4.4. All distributions have been normalised to unity in order to easily compare their shape, therefore the vertical axis is not labelled as it is not of interest here.

	LL	DD
All D^0 modes except the ADS modes	0.6	0.7
ADS modes	0.6	0.9

Table 4.5: BDT requirements for each of the D^0 decay modes, where the BDT classifier must be greater than the values in the table, for both LL and DD candidates.

	LL	DD
$B^- \to D(K^-\pi^+)K^{*-}$	0.95 (0.06)	0.90 (0.05)
$B^- \to D(K^-\pi^+\pi^-\pi^+)K^{*-}$	0.95 (0.04)	0.93 (0.03)

Table 4.6: Signal (background) efficiencies averaged across the whole dataset for the chosen BDT requirements in both $B^- \to D(K^-\pi^+)K^{*-}$ and $B^- \to D(K^-\pi^+\pi^-\pi^+)K^{*-}$ modes.

4.1.5 Summary of the selection requirements

Table 4.7 lists a summary of the selection requirements applied to both two- and four-body $B^- \to DK^{*-}$ decays to combinatorial background events and peaking backgrounds.

Variable	Selection requirement
Mass variables	
$\mid D^0$ mass - 1864.86 MeV/c^2 $\mid$	< 25 MeV/c^2
$\mid K^0_S$ mass - 497.614 MeV/c^2 $\mid$	< 15 MeV/c^2 for LL, < 20 MeV/c^2 for DD
$\mid K^{*-}$ mass - 892 MeV/c^2 $\mid$	< 75 MeV/c^2
PID and veto	
DLLK of bachelor	< 4
DLLK of D daughters (two-body)	> 2 for all kaons, $<$ -2 for all pions
DLLK of D daughters ($D^0 \to K^-\pi^+\pi^-\pi^+$)	> 2 for K^-, $<$ -2 for both π^+ mesons
DLLK of D daughters ($D^0 \to \pi^-\pi^+\pi^-\pi^+$)	$<$ -2 for both π^+ mesons
$\lvert D^0{}_{swapped} - 1864.86\,\mathrm{MeV}/c^2\rvert$ for ADS modes	> 15 MeV/c^2
Other backgrounds	
$\lvert\cos(\theta_{K^0_S})\rvert$	> 0.3
D^0 FD significance	> 2
K^0_S FD significance	> 5 for LL, no requirement for DD
B^- χ^2_{IP}	0 - 25
B^- χ^2/dof	0 - 100
BDT	
BDT classifier for CF and GLW modes	> 0.6 for LL, > 0.7 for DD
BDT classifier for ADS modes	> 0.6 for LL, > 0.9 for DD

Table 4.7: Summary of the selection requirements applied to two- and four-body $B^- \to DK^{*-}$ decays in this analysis.

4.1.6 Final refitted B^- mass distributions

The reconstructed B^- mass distributions, with constraints applied, for each of the samples passing the full selection requirements, detailed in this chapter, are given in Fig. 4.17.

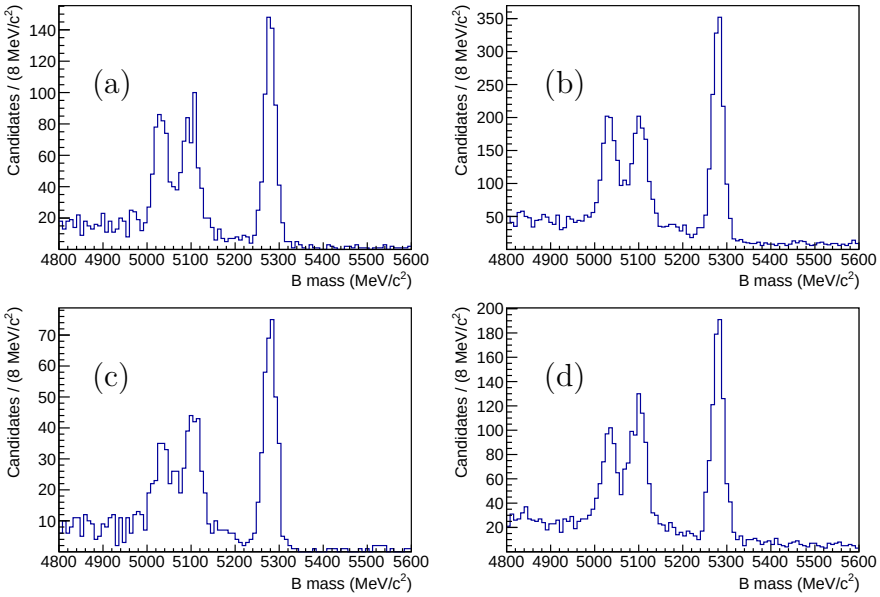

Figure 4.17: Refitted B^- mass distributions in data after the full selection has been applied for (a) $B^- \to D(K^-\pi^+)K^{*-}$ LL, (b) $B^- \to D(K^-\pi^+)K^{*-}$ DD, (c) $B^- \to D(K^-\pi^+\pi^-\pi^+)K^{*-}$ LL, and (d) $B^- \to D(K^-\pi^+\pi^-\pi^+)K^{*-}$ DD candidates, with Run 1 and Run 2 samples combined.

4.2 Mass parameterisation of the favoured modes

This section describes the B^- mass parameterisation developed for the two- and four-body favoured D^0 modes. The aim is to first develop a model that parameterises the invariant B^- mass, and then perform fits to the $B^- \to D(K^-\pi^+)K^{*-}$ and $B^- \to D(K^-\pi^+\pi^-\pi^+)K^{*-}$ data from which various parameters can be extracted. This model is later applied to the suppressed D^0 decay modes when performing the simultaneous fit to measure the *CP* observables, as described in Chapter 5. There are three components considered in the model:

1. Signal, $B^- \to DK^{*-}$ decays,
2. Combinatorial background,
3. Partially reconstructed background.

As some differences are found, data samples are split into the following categories: LL and DD K^0_S reconstruction types, Run 1 and Run 2 data-taking periods and two-body and four-body modes.

4.2.1 Maximum and extended maximum likelihood

The maximum likelihood, or extended maximum likelihood, technique is used to find the best model parameters to describe the data [67, 68]. A model consists of a probability density function (PDF), $f(x;\theta)$, which is a function of a continuous random variable, x, and depends on various parameters, θ, that control the shape of the distribution. The integral across an interval gives the probability that the value is within that interval. Therefore the total PDF is normalised to unity. An experiment performs n independent observations of x, $\{x_1, x_2, ..., x_n\}$. The likelihood is the probability, for given values of the parameters, of observing a particular dataset,

$$L(\theta) = \prod_{i=1}^{n} f(x_i;\theta). \tag{4.5}$$

The parameters are extracted for a given dataset by finding the best combination of these parameters that maximise the likelihood [67]. The maximum likelihood

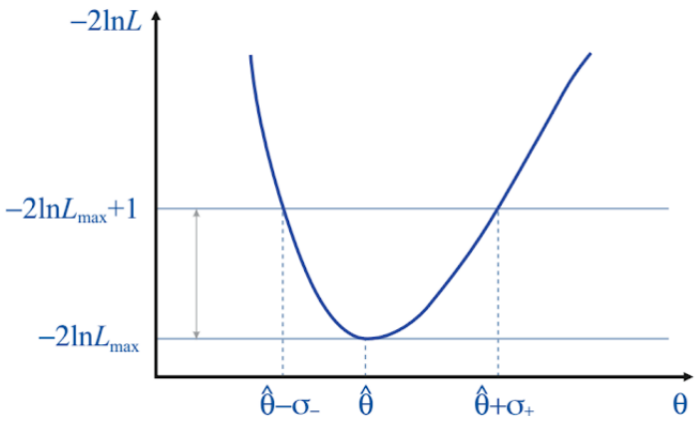

Figure 4.18: An illustrative example of a distribution of $-2\log L$ as a function of the parameter θ. The uncertainty is determined by the variation in $-2\log L$ about the minimum.

technique can be extended to use the number of events described by the PDF as an extra freely-varying parameter [68]. In this case, the likelihood is multiplied by a Poisson probability (of mean N) for observing a sample size n,

$$L(\theta, N) = \frac{e^{-N}}{n!} N^n \prod_{i=1}^{n} f(x_i;\theta) = \frac{e^{-N}}{n!} \prod_{i=1}^{n} N f(x_i;\theta) \ , \tag{4.6}$$

where N is the expected number of events, a parameter to be determined. Maximising the extended likelihood, based on a given dataset, gives estimates for the shape parameters and number of events described by the PDF.

In practice, it is easier to minimise the negative log likelihood, $-2\log(L(\theta, N; x))$. The uncertainties in the parameter estimates are given by the change in the parameter necessary to increase $-2\log L$ by one, as illustrated in Fig. 4.18. For a non-symmetric likelihood distribution, this can result in different values for the positive and negative uncertainties.

Figure 4.18 illustrates $-2\log L$ as a function of a single parameter as an example, however, this procedure usually involves a multi-dimensional minimisation being performed. Additionally, a model is often constructed which contains multiple PDFs. Due to the complexity of the problem, the minimisation is performed using numerical methods [69].

4.2.2 Signal shape

A single Gaussian is not sufficient to model the signal shape in B^- mass as the detector resolution is not straightforward. Instead, it varies with momentum and location of the tracks within the detector. Therefore the shape is described as the sum of two Gaussians, each with a tail extending towards lower invariant mass to account for radiative effects. These modified Gaussians are known as Crystal Ball (CB) functions [70]. The so-called Double Crystal Ball (DCB) shape is defined as a function of reconstructed mass, m, by

$$\mathrm{DCB}(m|\mu,\sigma,\alpha,n,f_\sigma) = f_{cb}\cdot\mathrm{CB}(m|\mu,\sigma,\alpha,n)+(1-f_{cb})\cdot\mathrm{CB}(m|\mu,f_\sigma\sigma,\alpha,n), \quad (4.7)$$

where

$$\mathrm{CB}(m|\mu,\sigma,\alpha,n) = \begin{cases} e^{-((m-\mu)/\sigma)^2/2}, & \text{if } \frac{m-\mu}{\sigma} \geq -\alpha, \\ \left(\frac{n}{|\alpha|}\right)^n e^{-|\alpha|^2/2}\left(\frac{n}{|\alpha|}-|\alpha|-\left(\frac{m-\mu}{\sigma}\right)\right)^{-n}, & \text{otherwise.} \end{cases}$$

Here μ is the peak position, σ is the width of the Gaussian, n parameterises the power-law tail, which starts $\alpha\sigma$ away from the peak position. The parameters f_{cb} and $(1-f_{cb})$ are the fractions of the yield given to each CB, and f_σ is the ratio of the widths between the two CBs. The signal PDF, $P_{sig}(m)$, must be normalised to unity with normalisation constant, $\mathcal{K}_{sig}$, such that

$$P_{sig}(m) = \mathcal{K}_{sig}.DCB(m|\mu,\sigma,\alpha,n,f_\sigma) \text{ , where } \int_{m_0}^{m_1} P_{sig}(m)\, dm = 1 \text{ ,} \quad (4.8)$$

and m_0 and m_1 are the lower and upper limits of the mass fit, respectively.

The B^- mass distributions from simulated signal events are found to be consistent between Run 1 and Run 2 data samples, but slightly different for $B^- \to D(K^-\pi^+)K^{*-}$ and $B^- \to D(K^-\pi^+\pi^-\pi^+)K^{*-}$ modes. Therefore the signal shape for different data-taking periods is the same, but different between $B^- \to D(K^-\pi^+)K^{*-}$ and $B^- \to D(K^-\pi^+\pi^-\pi^+)K^{*-}$ modes.

Unbinned maximum likelihood fits are performed to simulated signal samples, as shown in Fig. 4.19, and the shape parameters obtained from these fits are detailed in Table 4.8. The residuals in these plots are defined as the difference between the data and the projection of the PDF in the centre of the bin, divided by the Poisson

error on the number of candidates in that bin. The tail parameters, α and n, are highly correlated, therefore in order to prevent arbitrary variations between the two parameters and to ensure a stable fit, n is fixed in the fits to the simulated samples. The variation in this parameter does not have significant effect on the quality of the fit, and therefore n is fixed to unity. For the fit to data, in addition to n, the tail parameter α and the ratio of the widths between the CBs, f_σ, are fixed from simulation. However, it is necessary to allow for some variation in the signal shape when performing the fit to data, as parameters, such as the peak position and width, may take slightly different values in data due to imperfections in the simulation of reconstruction and resolution effects of the LHCb detector. Therefore, the peak position and width, μ and σ, are allowed to vary.

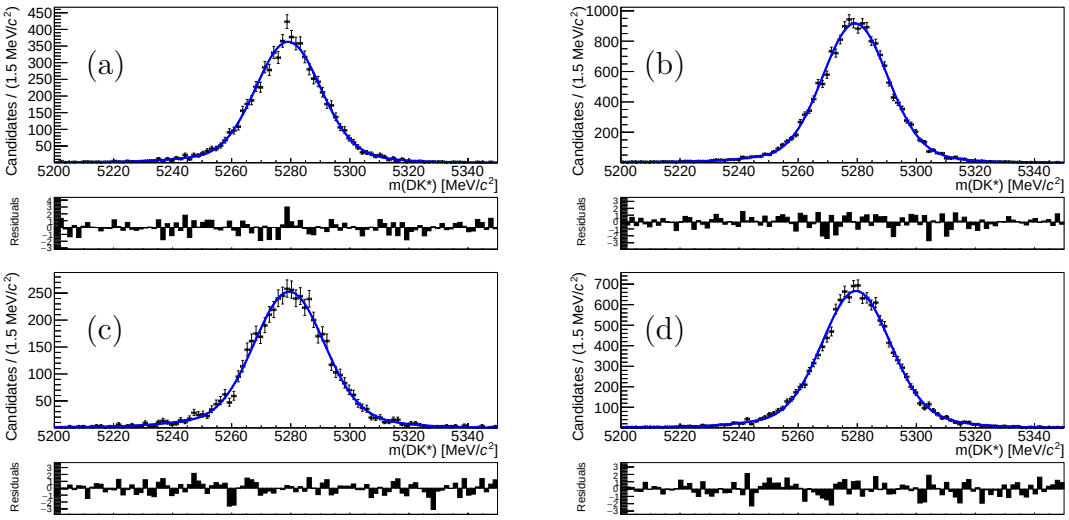

Figure 4.19: Results of the unbinned maximum likelihood fits to the B^- mass distribution from simulated signal samples with Run 1 and Run 2 data combined for (a) $B^- \to D(K^-\pi^+)K^{*-}$ LL, (b) $B^- \to D(K^-\pi^+)K^{*-}$ DD, (c) $B^- \to D(K^-\pi^+\pi^-\pi^+)K^{*-}$ LL, and (d) $B^- \to D(K^-\pi^+\pi^-\pi^+)K^{*-}$ DD. The black points represent the simulated data, while the blue curve is the projection of the optimised shape of the form given in Eq. 4.7. The residuals are shown at the bottom of each plot.

4.2.3 Combinatorial background

The combinatorial background is formed of random tracks, that do not correspond to the signal decay, being combined in the reconstruction. The combinatorial

	$B^- \to D(K^-\pi^+)K^{*-}$		$B^- \to D(K^-\pi^+\pi^-\pi^+)K^{*-}$	
	LL	DD	LL	DD
μ/ MeV/c^2	5279.12 ± 0.15	5279.30 ± 0.09	5279.62 ± 0.12	5279.50 ± 0.19
σ/ MeV/c^2	10.7 ± 0.3	10.8 ± 0.2	11.2 ± 0.2	11.6 ± 0.3
f_σ	2.04 ± 0.10	1.97 ± 0.06	2.08 ± 0.07	2.10 ± 0.11
α	2.53 ± 0.07	2.46 ± 0.04	2.60 ± 0.07	2.50 ± 0.10
n	1.0 (fixed)	1.0 (fixed)	1.0 (fixed)	1.0 (fixed)
f_{cb}	0.82 ± 0.03	0.84 ± 0.02	0.80 ± 0.03	0.81 ± 0.04

Table 4.8: Signal shape parameters obtained by a fit to simulated signal samples of the $B^- \to D(K^-\pi^+)K^{*-}$ and $B^- \to D(K^-\pi^+\pi^-\pi^+)K^{*-}$ modes with Run 1 and Run 2 samples combined. Parameter names are defined in Eq. 4.7. All parameters except for the peak position and width are fixed to these values in the mass fit to data.

background is modelled using an exponential PDF, P_{bkg}, given by

$$P_{bkg} = \mathcal{K}_{bkg}\ e^{\beta m}\ , \quad \text{with } \mathcal{K}_{bkg} = \frac{\beta}{e^{\beta m_1} - e^{\beta m_0}}\ , \tag{4.9}$$

and where m_0 and m_1 are the lower and upper limits of the mass fit, respectively, and β is the slope parameter that is allowed to vary.

4.2.4 Partially reconstructed backgrounds

Partially reconstructed decays refer to those in which one or more particle, in a B decay similar to the signal decay, has failed to be reconstructed, resulting in peaking structures in the B mass spectrum at a reconstructed mass lower than the signal peak. The partially reconstructed decays are of the form $B \to D^*K^*$, where the D^* decays to a D^0 meson and a pion or photon that is missed when reconstructing the decay. Three partially reconstructed decays contribute to the invariant mass fit:

- $B^- \to (D^{*0} \to D^0[\pi^0])K^{*-}$,
- $B^- \to (D^{*0} \to D^0[\gamma])K^{*-}$,
- $B^0 \to (D^{*+} \to D^0[\pi^+])K^{*-}$,

where the particle in square brackets corresponds to the missed particle. Each $B \to D^*K^*$ decay is a *Scalar* $\to$ *Vector Vector* decay, therefore, due to the conservation of angular momentum, there are three different helicity amplitudes to consider,

labelled +1, 0, -1 corresponding to the helicity state of the D^* particle. The helicity state of the D^* and the spin of the missing particle in the subsequent D^* decay determines the distribution of the reconstructed B mass. The states +1 and -1 produce the same distribution in B^- mass, therefore for the mass parameterisation these states are combined and collectively referred to as ± 1. This results in six different shapes to be modelled in the mass fit:

- $B^- \to (D^{*0} \to D^0[\pi^0])K^{*-}$, D^{*0} helicity: 0,
- $B^- \to (D^{*0} \to D^0[\pi^0])K^{*-}$, D^{*0} helicity: ± 1,
- $B^- \to (D^{*0} \to D^0[\gamma])K^{*-}$, D^{*0} helicity: 0,
- $B^- \to (D^{*0} \to D^0[\gamma])K^{*-}$, D^{*0} helicity: ± 1,
- $B^0 \to (D^{*+} \to D^0[\pi^+])K^{*-}$, D^{*+} helicity: 0,
- $B^0 \to (D^{*+} \to D^0[\pi^+])K^{*-}$, D^{*+} helicity: ± 1.

All of these shapes are modelled using three analytic PDFs; the so-called Horns, Hill and Little Horns, developed by Paolo Gandini and Shu-Faye Cheung for the study of $B^- \to D(hh')K^-$ and $B^0 \to DK^{*0}$ decays [32, 34]. These shapes are physically motivated, exploiting the decay kinematics of the partially reconstructed decays.

Horns function

Consider the $B^- \to D^{*0}K^{*-}$, $D^{*0} \to D^0\pi^0$, where the D^{*0} is in helicity state 0. The helicity of the D^{*0}, the fact that the missing π^0 meson is spin-0 and the requirement that angular momentum must be conserved means that the π^0 meson will decay predominantly along the helicity angle $\theta = 0°$ or $\theta = 180°$. The distribution θ has a one-to-one correspondence with its momentum and therefore the reconstructed B^- mass. When $\theta = 0°$, the fraction of momentum carried by the π^0 in the B^- rest frame is at its smallest, resulting in a larger reconstructed B^- mass. Conversely, if $\theta = 180°$, the fraction of momentum carried by the π^0 is greatest, leading to a lower reconstructed B^- mass.

This distribution is modelled using the Horns function. The underlying kinematic distribution is a parabola, $p_{HORNS}(x)$, with kinematics end-points a and b, determined in the fit, where

$$p_{HORNS}(x) = \begin{cases} \left(x - \frac{a+b}{2}\right)^2, & \text{if } a \leq x \leq b \\ 0, & \text{otherwise.} \end{cases} \tag{4.10}$$

The reconstruction of particles within the LHCb detector gives rise to resolution effects that result in a smearing of the mass distribution. These resolution effects are modelled by convolving the Horns parabola with two Gaussians. Given a Gaussian function of mean m and width σ, $G(m, \sigma)$, a Double Gaussian can be constructed as

$$DG(x) = f_G G(x|m, \sigma) + (1 - f_G)\, G(x|m, R_\sigma \sigma) \ , \tag{4.11}$$

where σ is the width of the first Gaussian, f_G is the fractional yield contained by the first Gaussian and R_σ is the relative width between the two. Additionally selection effects, arising from preferentially selecting high p_{T} events, can affect the shape of one peak relative to the other. This is taken into account by introducing a linear polynomial with a slope of $1 - \xi$. The resulting Horns PDF is

$$\begin{aligned} \mathrm{Horns}(m) = \mathcal{K}_{Horns} \int_a^b dx \left(x - \frac{a+b}{2}\right)^2 DG(x|m, \sigma, f_G, R_\sigma) \\ \left(\frac{1 - \xi_{HORNS}}{b-a} x + \frac{b\xi_{HORNS} - a}{b-a}\right), \end{aligned} \tag{4.12}$$

where m is the mass variable to be fitted, x is the integration variable in the convolution, and $\mathcal{K}_{Horns}$ is the normalisation constant required for the PDF. An example of such a double peak structure is shown in Fig. 4.20 for simulated data.

Hill function

Consider now the $B^- \to D^{*0} K^{*-}$, $D^{*0} \to D^0 \gamma$, where the D^{*0} is in helicity state 0. The helicity of the D^{*0}, the fact that the γ is spin-1 and the requirement that angular momentum is conserved means that the γ will decay predominantly along $\theta = 90°$ or $\theta = 270°$. The fraction of momentum carried by the photon is the same in both cases, so no double peak structure is observed.

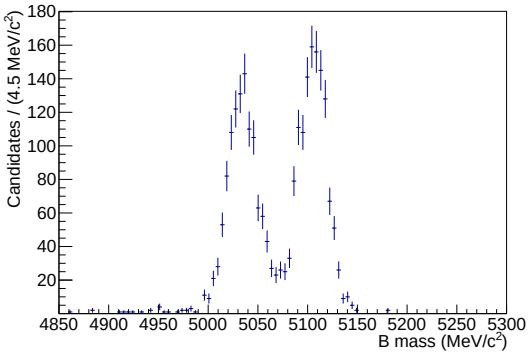

Figure 4.20: Distribution of simulated $B^- \to (D^{*0} \to D^0\pi^0)K^{*-}$ events, where the π^0 is missed in reconstruction and the D^{*0} is in helicity state 0.

This distribution is modelled using the Hill function. The underlying kinematic distribution is a parabola with negative curvature, $p_{HILL}(x)$, and kinematic endpoints a and b where

$$p_{HILL}(x) = \begin{cases} -(x-a')(x-b'), & \text{if } a' \leq x \leq b' \\ 0, & \text{otherwise.} \end{cases} \tag{4.13}$$

As with the Horns function, this parabola is convolved with a Double Gaussian and a linear polynomial to account for resolution and selection effects, respectively. The resulting Hill function is

$$\text{Hill}(m) = \mathcal{K}_{Hill} \int_{a'}^{b'} dx \, [-(x-a')(x-b')] \, DG(x|m,\sigma,f_G,R_\sigma) \left(\frac{1-\xi_{HILL}}{b'-a'}x + \frac{b'\xi_{HILL}-a'}{b'-a'}\right), \tag{4.14}$$

where m is the mass variable to be fitted, x is the integration variable in the convolution and $\mathcal{K}_{Hill}$ is the normalisation constant required for the PDF. This Hill function also applies to the $B^- \to D^{*0}K^{*-}$, $D^{*0} \to D^0\pi^0$ decay, where the D^{*0} is in helicity state ± 1. An example of such a distribution is shown in Fig. 4.21 for simulated data.

Little Horns function

For the configuration $B^- \to D^{*0}K^{*-}$, $D^{*0} \to D^0\gamma$, where the D^{*0} is in helicity state ± 1, the B^- mass distribution is shown in Fig. 4.22.

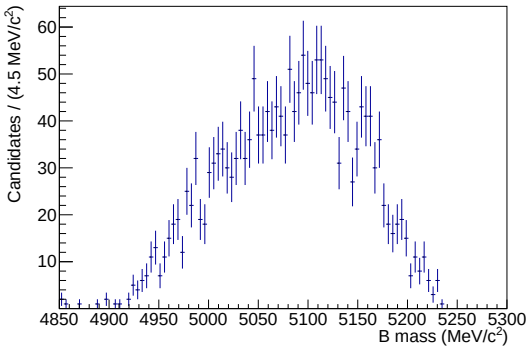

Figure 4.21: Distribution of simulated $B^- \to (D^{*0} \to D^0\gamma)K^{*-}$ events, where the γ is missed in reconstruction and the D^{*0} is in helicity state 0.

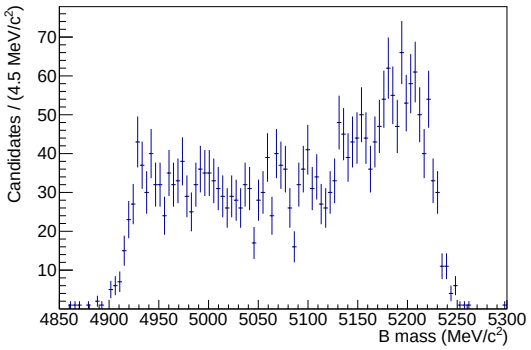

Figure 4.22: Distribution of simulated $B^- \to (D^{*0} \to D^0\gamma)K^{*-}$ events, where the γ is missed in reconstruction and the D^{*0} is in helicity state ± 1.

This is modelled using the Little Horns shape. The underlying kinematic distribution is described by the sum of a parabola and a uniform distribution, $p_{LITTLEHORNS}(x)$, and kinematic endpoints a'' and b'' where

$$p_{LITTLEHORNS}(x) = \begin{cases} \left(x - \frac{a''+b''}{2}\right)^2 + \left(\frac{a''-b''}{2}\right)^2, & \text{if } a'' \leq x \leq b'' \\ 0, & \text{otherwise.} \end{cases} \tag{4.15}$$

Again, this distribution is convolved with a Double Gaussian and linear polynomial to describe the resolution and selection effects, respectively. This results in a Little Horns function

$$\text{LittleHorns}(m) = \mathcal{K}_{LittleHorns} \int_{a''}^{b''} dx \Bigg\{ \left[\left(x - \frac{a''+b''}{2}\right)^2 + \left(\frac{a''-b''}{2}\right)^2 \right] DG(x|m,\sigma,f_G,R_\sigma) \left(\frac{1-\xi_{LITTLEHORNS}}{b''-a''} x + \frac{b''\xi_{LITTLEHORNS} - a''}{b''-a''} \right) \Bigg\}, \tag{4.16}$$

where m is the mass variable to be fitted, x is the integration variable in the convolution and $\mathcal{K}_{LittleHorns}$ is the normalisation constant required for the PDF.

Total partially reconstructed function

The normalisation constants $\mathcal{K}_{Horns}$, $\mathcal{K}_{Hill}$ and $\mathcal{K}_{LittleHorns}$ in Eqs. 4.12, 4.14 and 4.16 respectively, are required for the PDFs to be correctly normalised. This requires, $\int_{m_0}^{m_1} P(m)dm = 1$ for each of the PDFs, $P(m)$, where m_0 and m_1 are the lower and upper limits of the mass fit. Due to the complexity of the shapes, the normalisation constant is calculated numerically.

Each partially reconstructed shape contributes to the mass fit in the B^- mass region below the signal peak. Table 4.9 summarises the use of the different analytic shapes described: Horns, Hill and Little Horns functions.

Decay mode	Helicity of D^*	Kinematic dependence	PDF
$B^- \to (D^{*0} \to D^0[\pi^0])K^{*-}$	0	$\left(x - \frac{a_1+b_1}{2}\right)^2$	Horns, from Eq. 4.12
$B^- \to (D^{*0} \to D^0[\pi^0])K^{*-}$	± 1	$-(x-a_2)(x-b_2)$	Hill, from Eq. 4.14
$B^- \to (D^{*0} \to D^0[\gamma])K^{*-}$	0	$-(x-a_3)(x-b_3)$	Hill, from Eq. 4.14
$B^- \to (D^{*0} \to D^0[\gamma])K^{*-}$	± 1	$\left(x - \frac{a_4+b_4}{2}\right)^2 + \left(\frac{a_4-b_4}{2}\right)^2$	Little Horns, from Eq. 4.16
$B^0 \to (D^{*+} \to D^0[\pi^+])K^{*-}$	0	$\left(x - \frac{a_5+b_5}{2}\right)^2$	Horns, from Eq. 4.12
$B^0 \to (D^{*+} \to D^0[\pi^+])K^{*-}$	± 1	$-(x-a_6)(x-b_6)$	Hill, from Eq. 4.14

Table 4.9: The different partially reconstructed shapes for the D^* helicity states. The kinematic endpoints a_i and b_i can be different for each of the partially reconstructed shapes.

In order to obtain values for the various parameters in the shape functions, simulated samples are generated and the full reconstruction and selection applied. The parameters are obtained from performing individual unbinned maximum likelihood fits to the simulated samples using the functions given by Eqs. 4.12, 4.14 and 4.16. The fits for DD events are shown in Fig. 4.23, those for the LL samples are similar. All shape parameters are then fixed to these values for the fits to data. Although the simulated samples forced the D^0 meson to decay to $K^-\pi^+$, the D^0 meson decay mode does not have a significant effect on the shape of the partially reconstructed background, hence the same shapes are used for all D^0 decay modes. Similarly, distributions in B^- mass of Run 1 and Run 2 simulated samples are considered sufficiently similar to use the same shapes for both data-taking periods.

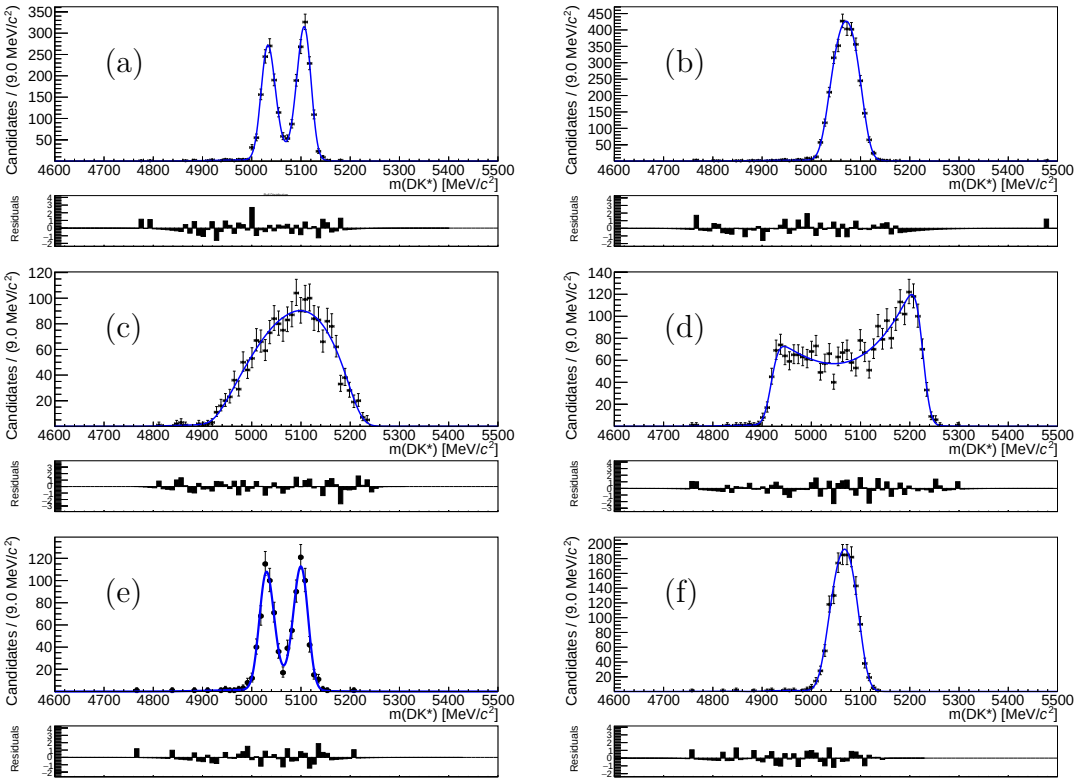

Figure 4.23: Results of the unbinned maximum likelihood fits to the B^- mass distribution for $B \to D^*K^*$ Run 1 simulated samples for DD candidates (a) $B^- \to (D^{*0} \to D^0[\pi^0])K^{*-}$ 0, (b) $B^- \to (D^{*0} \to D^0[\pi^0])K^{*-}$ ±1, (c) $B^- \to (D^{*0} \to D^0[\gamma])K^{*-}$ 0, (d) $B^- \to (D^{*0} \to D^0[\gamma])K^{*-}$ ±1, (e) $B^0 \to (D^{*+} \to D^0[\pi^+])K^{*-}$ 0, and (f) $B^0 \to (D^{*+} \to D^0[\pi^+])K^{*-}$ ±1. The residuals are shown at the bottom of each plot.

As the shapes all occur in the same region of B^- mass, allowing the six individual yield parameters to vary leads to an unstable fit. Therefore, it is necessary to apply additional constraints, in the form of fixing ratios of different yields.

The total partially reconstructed PDF, $P_{partreco}$, is given by

$$P_{partreco} = f_0 P_0 + (1 - f_0) P_{\pm1} \ , \tag{4.17}$$

where P_0 and $P_{\pm1}$ represent the shapes for the D^* helicity states 0 and ±1 respectively, and are given by

$$P_0 = \frac{1}{1 + c_0^{B^-,\gamma} + c_0^{B^0,\pi}} \left(P_0^{B^-,\pi} + c_0^{B^-,\gamma} P_0^{B^-,\gamma} + c_0^{B^0,\pi} P_0^{B^0,\pi} \right) \ ,$$
$$P_{\pm1} = \frac{1}{1 + c_{\pm1}^{B^-,\gamma} + c_{\pm1}^{B^0,\pi}} \left(P_{\pm1}^{B^-,\pi} + c_{\pm1}^{B^-,\gamma} P_{\pm1}^{B^-,\gamma} + c_{\pm1}^{B^0,\pi} P_{\pm1}^{B^0,\pi} \right) \ .$$

Here $P_x^{y,z}$ represents the partially reconstructed PDF, where x is the D^* helicity state (0 or ± 1), y is the type of B meson (B^- or B^0), and z is the particle missed in the reconstruction (π or γ). Similarly, $c_x^{y,z}$ are the ratios between the yields. The yield ratios between $B^- \to (D^{*0} \to D^0[\pi^0])K^{*-}$, $B^- \to (D^{*0} \to D^0[\gamma])K^{*-}$ and $B^0 \to (D^{*+} \to D^0[\pi^+])K^{*-}$ are fixed separately for the 0 and ± 1 helicity states of the D^*. The expected yield ratios, $c_0^{B^-,\gamma}$, $c_0^{B^0,\pi}$, $c_{\pm 1}^{B^-,\gamma}$ and $c_{\pm 1}^{B^0,\pi}$ can be individually calculated from knowledge of the ratio of production of the relevant decays and the ratio of the efficiencies, as detailed in Sec. 4.1. By way of example,

$$\begin{aligned} c_0^{B^-,\gamma} &= \frac{N(B^- \to (D^{*0} \to D^0\gamma)K^{*-})}{N(B^- \to (D^{*0} \to D^0\pi^0)K^{*-})} \\ &= \frac{\mathcal{B}(B^- \to (D^{*0} \to D^0\gamma)K^{*-})}{\mathcal{B}(B^- \to (D^{*0} \to D^0\pi^0)K^{*-})} \times \frac{\epsilon_{sel}(B^- \to (D^{*0} \to D^0\gamma)K^{*-})}{\epsilon_{sel}(B^- \to (D^{*0} \to D^0\pi^0)K^{*-})} \end{aligned} \quad (4.18)$$

where N represents the yield, $\mathcal{B}$ represents the branching fraction and ϵ_{sel} represents the selection efficiency of the partially reconstructed decay. The branching fractions used in the ratios are given in Table 4.10. The selection efficiency, ϵ_{sel}, calculated using simulated samples, is defined as the number of partially reconstructed events passing the selection compared to the number generated. Using Eq. 4.18 and equivalent calculations, the values are then fixed in the mass fit. The estimated yield ratios are given in Table 4.11.

Mode	Branching ratio
$B^- \to (D^{*0} \to D^0\pi^0)K^{*-}$	$(5.0 \pm 0.9) \times 10^{-4}$
$B^- \to (D^{*0} \to D^0\gamma)K^{*-}$	$(3.1 \pm 0.6) \times 10^{-4}$
$B^0 \to (D^{*+} \to D^0\pi^+)K^{*-}$	$(2.2 \pm 0.4) \times 10^{-4}$

Table 4.10: Branching ratios for the different partially reconstructed decay modes. These are taken from Ref [10], constructed by multiplying the relevant B and D^* branching fractions.

Other backgrounds investigated in this analysis, but not included in the mass fit, are discussed in Sec. 4.1.3.

4.2.5 Mass fit to the data in the favoured modes

Extended maximum likelihood fits to the invariant B mass in the $B^- \to D(K^-\pi^+)K^{*-}$ and $B^- \to D(K^-\pi^+\pi^-\pi^+)K^{*-}$ favoured modes are performed using the shapes

	LL	DD
$c_0^{B^-,\gamma}$	0.53 ± 0.14	0.51 ± 0.14
$c_0^{B^0,\pi}$	0.38 ± 0.14	0.37 ± 0.14
$c_{\pm1}^{B^-,\gamma}$	0.53 ± 0.14	0.51 ± 0.14
$c_{\pm1}^{B^0,\pi}$	0.38 ± 0.14	0.38 ± 0.14

Table 4.11: Yield ratios fixed in the mass fit for the partially reconstructed backgrounds.

discussed in Secs. 4.2.2, 4.2.3 and 4.2.4. The total extended likelihood PDFs used to model the data are given by

$$P_{tot}(x_i; \mathbb{O}, N) = N_{sig}P_{sig} + N_{comb}P_{comb} + N_{partreco}P_{partreco} \ , \tag{4.19}$$

where x_i is the reconstructed B^- mass of the candidate and $\mathbb{O}$ are the set of parameters to be optimised, namely $\{\mu, \sigma, \beta, f_0\}$, along with the expected yields, N, of the signal, combinatorial and partially reconstructed PDFs, $\{N_{sig}, N_{comb}, N_{partreco}\}$, as additional freely varying parameters to be determined, as described in Sec. 4.2.1. The signal PDF, P_{sig}, is given by Eq. 4.7, the combinatorial PDF, P_{comb}, is given by Eq. 4.9, where the slope parameter β varies in the fit, and the partially reconstructed PDF, $P_{partreco}$, is given by Eq. 4.17. The yield of the signal and combinatorial PDFs, N_{sig} and N_{comb}, are left to vary without constraint, as well as the peak position, μ, and width, σ, of the signal PDF. The only parameters not fixed in the partially reconstructed background are the yield ratio between the 0 and ±1 amplitudes, f_0, and the overall yield, $N_{partreco}$.

Figures 4.24 and 4.25 show the results of the extended maximum likelihood fits to the invariant B mass distribution in the $B^- \to D(K^-\pi^+)K^{*-}$ and $B^- \to D(K^-\pi^+\pi^-\pi^+)K^{*-}$ favoured modes respectively, for LL and DD candidates in both Run 1 and Run 2. The estimated signal yields extracted from these fits are given in Table 4.12. It can be seen that the yield in the $B^- \to D(K^-\pi^+)K^{*-}$ mode is almost twice as large as that in the $B^- \to D(K^-\pi^+\pi^-\pi^+)K^{*-}$ mode, which is primarily a result of the lower reconstruction efficiency due to the two additional tracks in the four-body mode, and additional PID requirements necessary to reduce

	$B^- \to D(K^-\pi^+)K^{*-}$		$B^- \to D(K^-\pi^+\pi^-\pi^+)K^{*-}$	
	Run 1	Run 2	Run 1	Run 2
LL	220 ± 16	388 ± 21	87 ± 10	215 ± 15
DD	505 ± 24	901 ± 33	205 ± 16	516 ± 25

Table 4.12: Signal yields from the $B^- \to D(K^-\pi^+)K^{*-}$ and $B^- \to D(K^-\pi^+\pi^-\pi^+)K^{*-}$ mass fits for both K^0_S reconstruction types and data-taking periods separately.

faking backgrounds. Table 4.12 also shows that the yield per unit of integrated luminosity is about 3 times higher in Run 2 (1.8 fb^{-1}) compared to Run 1 (3 fb^{-1}), which is driven by the increase in centre-of-mass energy in Run 2. The gain in yield between Run 1 and Run 2 is not the same for the two- and four-body modes due to the difference in trigger efficiencies.

The results for the $B^- \to D(K^-\pi^+)K^{*-}$ and $B^- \to D(K^-\pi^+\pi^-\pi^+)K^{*-}$ fits are shown in Tables 4.13a and 4.13b respectively. The values of μ are all consistent with the known B^- mass of $5279.3\,\text{MeV}/c^2$. The slight variations in the values are primarily due to the statistical uncertainty in the data. The parameter f_0 is the yield ratio between 0 and ± 1 helicity amplitudes in the partially reconstructed background, which is purely dependent on the physics of the decay, so should not vary depending on the data sample used. As observed in data, f_0 is found to be consistent between all of the categories in the $B^- \to D(K^-\pi^+)K^{*-}$ and $B^- \to D(K^-\pi^+\pi^-\pi^+)K^{*-}$ mass fits separately.

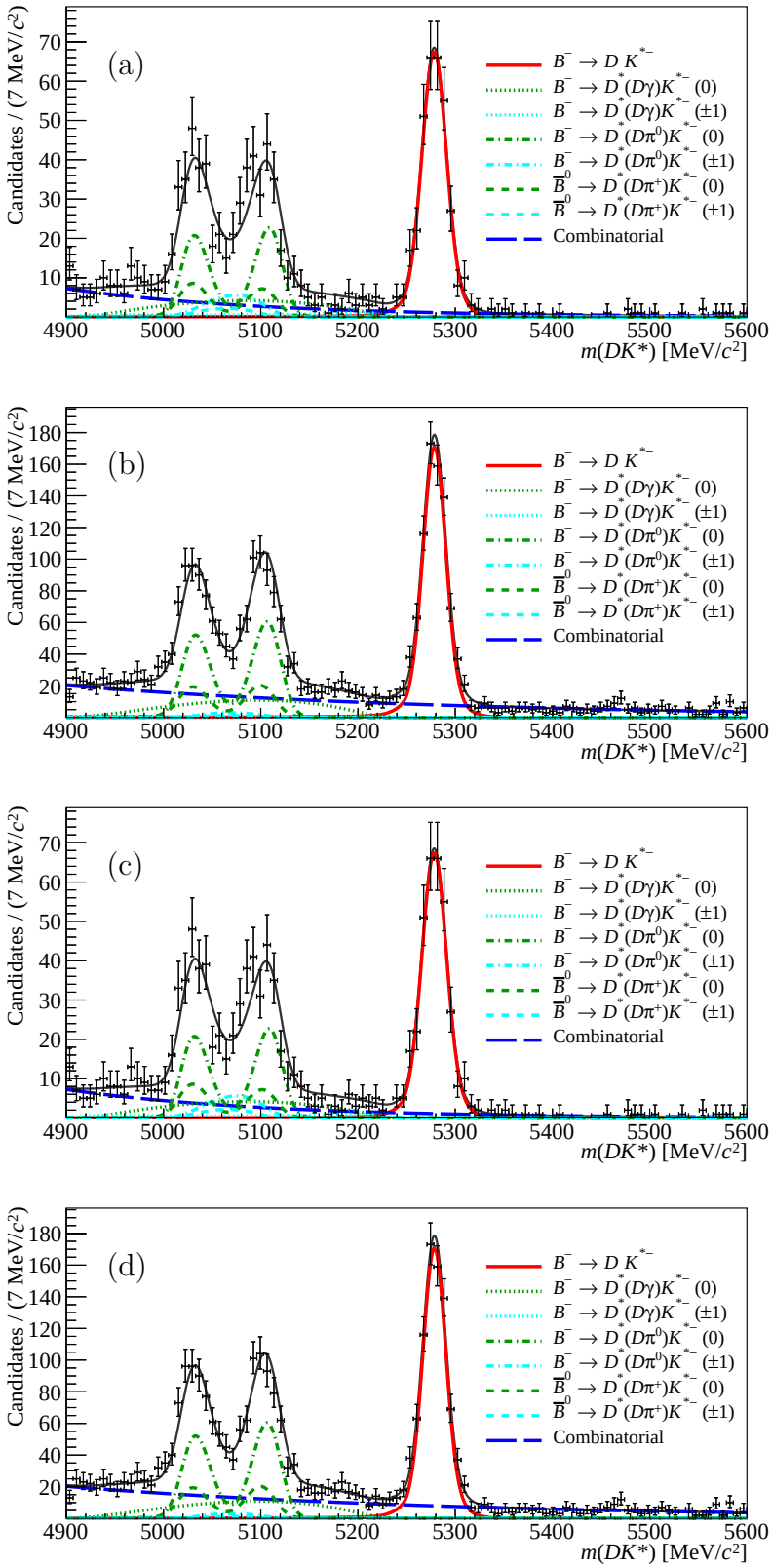

Figure 4.24: Results of the unbinned maximum likelihood fits to the $B^- \to D(K^-\pi^+)K^{*-}$ invariant B mass distribution for (a) Run 1 LL, (b) Run 1 DD, (c) Run 2 LL, and (d) Run 2 DD, with B^- and B^+ decays combined. The black points represent the data, while the black curve is the projection of the optimised shape of the form given in Eq. 4.19.

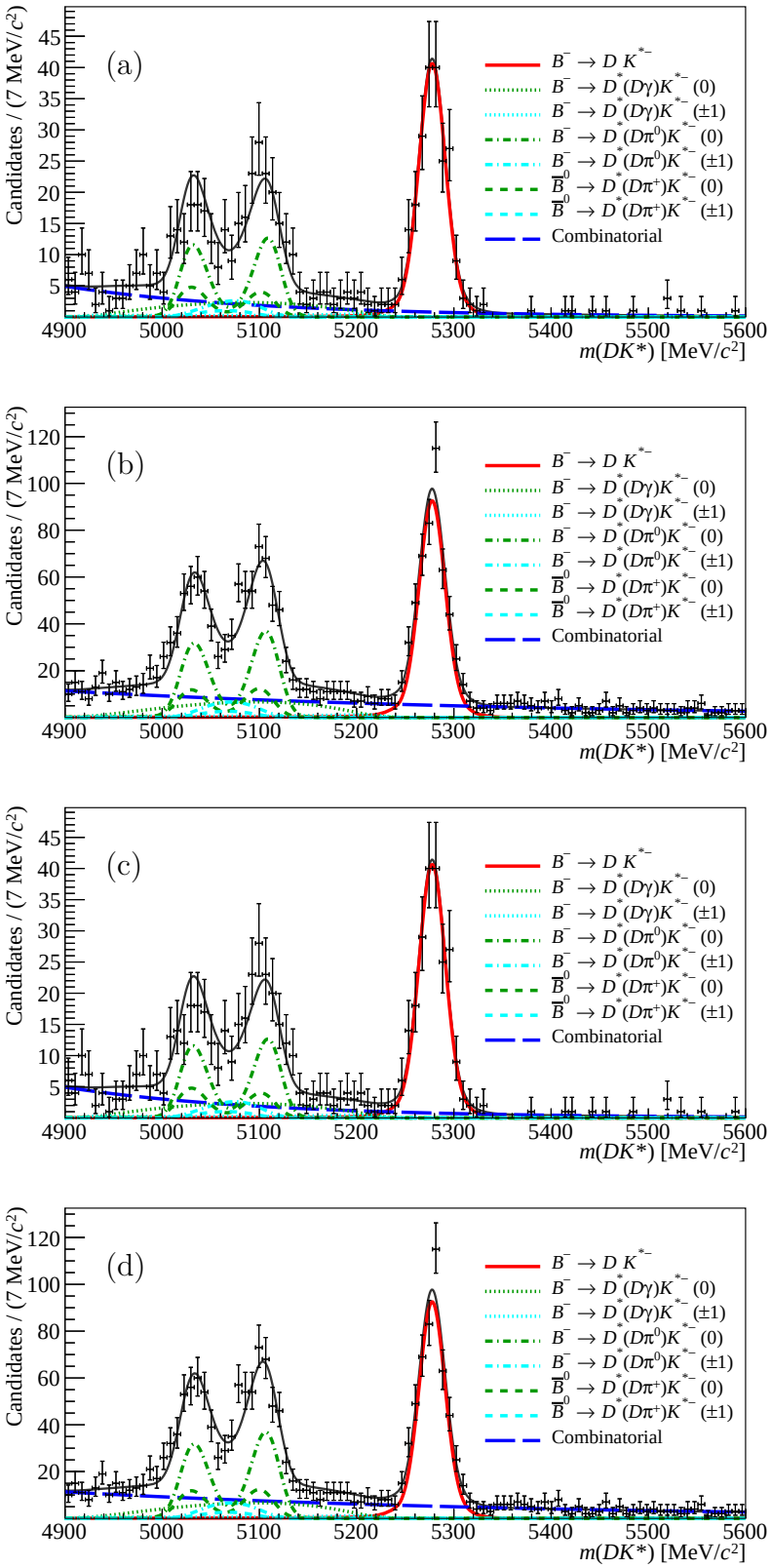

Figure 4.25: Results of the unbinned maximum likelihood fits to the $B^- \to D(K^-\pi^+\pi^-\pi^+)K^{*-}$ invariant B mass distribution for (a) Run 1 LL, (b) Run 1 DD, (c) Run 2 LL, and (d) Run 2 DD, with B^- and B^+ decays combined. The black points represent the data, while the black curve is the projection of the optimised shape of the form given in Eq. 4.19.

	Run 1		Run 2	
	LL	DD	LL	DD
$\beta/\,\mathrm{MeV}/c^2{}^{-1}$	$(-4.8 \pm 0.5) \times 10^{-3}$	$(-2.8 \pm 0.3) \times 10^{-3}$	$(-4.4 \pm 0.5) \times 10^{-3}$	$(-2.5 \pm 0.2) \times 10^{-3}$
f_0	0.15 ± 0.08	0.12 ± 0.05	0.18 ± 0.05	0.06 ± 0.04
$\mu/\,\mathrm{MeV}/c^2$	5280.7 ± 0.8	5280.7 ± 0.6	5278.5 ± 0.8	5278.6 ± 0.5
N_{comb}	167 ± 20	472 ± 34	223 ± 24	1100 ± 50
$N_{partreco}$	338 ± 23	810 ± 36	654 ± 31	1397 ± 49
N_{sig}	220 ± 16	505 ± 24	388 ± 21	901 ± 33
$\sigma/\,\mathrm{MeV}/c^2$	10.2 ± 0.7	11.5 ± 0.5	12.2 ± 0.6	11.5 ± 0.4

(a) Fit results from the $B^- \to D(K^-\pi^+)K^{*-}$ favoured mode.

	Run 1		Run 2	
	LL	DD	LL	DD
$\beta/\,\mathrm{MeV}/c^2{}^{-1}$	$(-5.2 \pm 1.1) \times 10^{-3}$	$(-2.3 \pm 0.4) \times 10^{-3}$	$(-4.4 \pm 0.5) \times 10^{-3}$	$(-2.1 \pm 0.2) \times 10^{-3}$
f_0	0.26 ± 0.11	0.20 ± 0.08	0.15 ± 0.07	0.16 ± 0.05
$\mu/\,\mathrm{MeV}/c^2$	5281.3 ± 1.3	5283.9 ± 0.9	5278.7 ± 1.0	5277.7 ± 0.7
N_{comb}	50 ± 12	252 ± 24	168 ± 20	707 ± 40
$N_{partreco}$	154 ± 15	317 ± 24	342 ± 23	914 ± 40
N_{sig}	102 ± 10	226 ± 16	244 ± 16	578 ± 27
$\sigma/\,\mathrm{MeV}/c^2$	11.4 ± 1.0	11.3 ± 0.8	12.9 ± 0.8	13.1 ± 0.6

(b) Fit results from the $B^- \to D(K^-\pi^+\pi^-\pi^+)K^{*-}$ favoured mode.

Table 4.13: Fit results from the $B^- \to D(K^-\pi^+)K^{*-}$ and $B^- \to D(K^-\pi^+\pi^-\pi^+)K^{*-}$ favoured modes, corresponding to the fits in Figs. 4.24 and 4.25. The parameter β is the combinatorial background slope, f_0 is the yield ratio between 0 and ± 1 helicity amplitudes, μ and σ are the peak position and width of the signal shape, and N_{sig}, N_{comb} and $N_{partreco}$ are the yields of signal, combinatorial background and partially reconstructed decays respectively.

5

Fits for *CP* observables in two- and four-body decays

In this chapter the *CP* observables are measured by performing an extended maximum likelihood fit to $B^- \to DK^{*-}$ candidates in data, simultaneously for each D^0 decay mode, where the data are split into B^+ and B^- decays. This fit is referred to as the *CP* fit. The mass parameterisation used in the *CP* fit is described in Sec. 5.1, before detailing the setup of the *CP* fit in Sec. 5.2. The *CP* fit results are given in Sec. 5.3, followed by an outline of the systematic uncertainties in Sec. 5.4. Section 5.5 presents a summary of the measurements of the *CP* observables.

5.1 Mass parameterisation of the *CP* fit

The mass parameterisation described in Sec. 4.2 is used to model all D^0 modes for both B charges in the *CP* fit. However, when generalising the model, developed for the charge-combined favoured modes, there must be additional factors taken into consideration, such as *CP* violation in the background components and additional sources of backgrounds in other D^0 decay modes.

5.1.1 Choice of fit range

The modelling of the partially reconstructed backgrounds pose a problem when being implemented in the *CP* fit, as detailed below. The relative yields for the partially reconstructed decays are fixed in the charge-combined mass fit to the favoured modes, as described in Sec. 4.2.4. When considering the favoured $B^- \to D(K^-\pi^+)K^{*-}$ and $B^- \to D(K^-\pi^+\pi^-\pi^+)K^{*-}$ decays in the *CP* fit it is reasonable to assume that no *CP* violation occurs, i.e. the yield ratios for B^- and B^+ are the same. However in the other D^0 final states, for example $B^- \to D(\pi^-K^+)K^{*-}$, *CP* violation is expected in the partially reconstructed background for which the *CP* violation parameters are unknown. Therefore, it is not possible to make any constraints on the B^+ and B^- yield ratios in these modes. The fit that would result from fitting six individual yields with an order of magnitude less data would be unstable and this lack of constraint in the low mass region would lead to a large amount of freedom in the combinatorial background, casting doubt that the signal yields could be correctly extracted. This problem is addressed by raising the lower limit of the B^- mass parameterisation when performing the *CP* fit, as discussed below.

The lower range of the mass parameterisation, illustrated in Fig. 4.24, is raised up to 5230 MeV/c^2, which only removes 0.4% of the total signal yield. There are a number of advantages to this. Firstly, as the overlap of the partially reconstructed and signal peaks is very small, this removes most of the partially reconstructed background. Hence, performing the *CP* fit from 5230 MeV/c^2 avoids the need to fit the various partially reconstructed yields in each of the other D^0 decays modes. Nevertheless, the extended mass fit to the favoured modes is required initially in order to estimate the amount of partially reconstructed background contributing above 5230 MeV/c^2. A further benefit is that low-level broad backgrounds, for example $B^- \to DK^{*-}\pi^0$ and $B^0 \to K^+\pi^-\pi^+\pi^-$, which may be present in the range 4900 - 5200 MeV/c^2, do not need to be considered as sources of systematic uncertainty.

The upper mass range used in the *CP* fit is 5600 MeV/c^2. This gives the fit sufficient data to accurately model the combinatorial background while maintaining

a reasonable sample size, above 5600 MeV/c^2 in B^- mass, to be used as the background sample in the BDT training.

5.1.2 Partially reconstructed yield in the *CP* fit

The modelling of the partially reconstructed background is described in detail in Sec. 4.2.4. The shape and yield of the small amount of partially reconstructed background present in all D^0 decay-mode categories above 5230 MeV/c^2 is determined and fixed from the fits to data of the $B^- \to D(K^-\pi^+)K^{*-}$ and $B^- \to D(K^-\pi^+\pi^-\pi^+)K^{*-}$ decays, taking into account the smaller branching fractions of the D^0 decays. Table 5.1 shows the fixed values of the partially reconstructed yields in the *CP* fit. The assumptions used to determine the fixed yields and shape are relaxed in order to evaluate the systematic uncertainties from the partially reconstructed background, as discussed in Sec. 5.4.1.

	Run 1		Run 2	
	LL	DD	LL	DD
$K\pi$	0.55	1.03	1.18	1.35
KK	0.060	0.112	0.116	0.131
$\pi\pi$	0.019	0.034	0.041	0.049
πK	0.008	0.012	0.017	0.016
$K\pi\pi\pi$	0.34	0.52	0.55	1.31
$\pi\pi\pi\pi$	0.031	0.045	0.050	0.122
$\pi K\pi\pi$	0.004	0.006	0.007	0.014

Table 5.1: Partially reconstructed yields fixed in the *CP* fit. The values show the number of events of B^+ and B^- combined; each of these are divided equally between the B^+ and B^- categories. Uncertainties for these values are O(10%).

5.1.3 Additional background component in the $B^- \to D(K^-K^+)K^{*-}$ mass spectrum

An additional source of background is present in the $B^- \to D(K^-K^+)K^{*-}$ mass spectrum from $\Lambda_b^0 \to \Lambda_c^+(pK^-\pi^+)K^{*-}$ decays, described in Sec. 4.1.3. The shape used to model the $\Lambda_b^0 \to \Lambda_c^+ K^{*-}$ contribution is a Cruijff PDF, defined as,

$$P_\Lambda(m;\mu,\sigma_L,\sigma_R,\alpha_L,\alpha_R) = \begin{cases} \mathcal{K}_L exp\left(-\frac{(m-\mu)^2}{2\sigma_L^2+\alpha_L(m-\mu)^2}\right), & \text{if } m-\mu<0, \\ \mathcal{K}_R exp\left(-\frac{(m-\mu)^2}{2\sigma_R^2+\alpha_R(m-\mu)^2}\right), & \text{otherwise,} \end{cases} \quad (5.1)$$

where μ is the peak position, $\sigma_{L,R}$ are the widths on the left and right sides of the peak, $\alpha_{L,R}$ are modification constants and $\mathcal{K}_{L,R}$ are the normalisation constants required for the PDF. Due to reasons relating to timing and speed of generation, a simulated sample of $\Lambda_b^0 \to \Lambda_c^+ K^{*-}$ events is not available. Therefore, the parameters of the PDF are taken from a maximum likelihood fit to a simulated sample of $\Lambda_b^0 \to \Lambda_c^+ K^-$ events reconstructed as $B^- \to DK^-$ events; this PDF is expected to be similar to one taken from a $\Lambda_b^0 \to \Lambda_c^+ K^{*-}$ sample, and any uncertainty in the shape is accounted for as a systematic uncertainty, described in Sec. 5.4.

A maximum likelihood fit, as described in Sec. 4.2.1, is performed on the B^- mass spectrum of the simulated sample. This fit is shown in Fig. 5.1, where it can be seen that the reconstructed B^- mass falls between 4800 and 5500 MeV/c^2. The results from the fit are shown in Table 5.2 and all corresponding shape parameters are fixed to these values in the simultaneous fit.

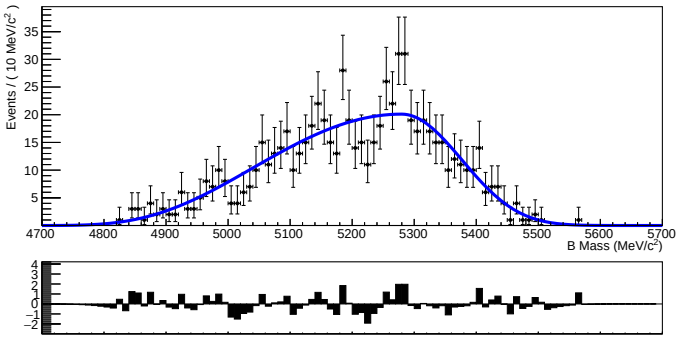

Figure 5.1: Maximum likelihood fit to the mass distribution of a simulated $\Lambda_b^0 \to \Lambda_c^+(pK^-\pi^+)K^-$ sample using a Cruijff function, where the π^+ is missed in reconstruction and the proton is misidentified as a kaon.

Parameter	Value
μ/ MeV/c^2	5280 ± 18
σ_L/ MeV/c^2	221 ± 26
σ_R/ MeV/c^2	96 ± 16
α_L	-0.19 ± 0.19
α_R	-0.04 ± 0.06

Table 5.2: Shape parameters from a maximum likelihood fit to simulated $\Lambda_b^0 \to \Lambda_c^+ K^-$ events using a Cruijff PDF. These shape parameters are fixed in the *CP* fit.

The PDF is assumed to be the same in each $B^- \to D(K^-K^+)K^{*-}$ category of the *CP* fit, i.e. the K^0_S reconstruction type (LL and DD) and data-taking period (Run 1 and Run 2). This is because there is such a low number of events that contribute to this background that the possible variations in the shape in the different categories have negligible effect on the results. The $\Lambda^0_b \to \Lambda^+_c(pK^-\pi^+)K^{*-}$ yield as a fraction of the signal yield in the favoured $B^- \to D(K^-\pi^+)K^{*-}$ mode, f_Λ, is allowed to vary in the fit and is required to be the same for all fit categories.

5.2 Setup of the *CP* fit

The *CP* fit is performed on the invariant mass of $B^- \to DK^{*-}$ candidates. A simultaneous fit strategy is employed on each of the 7 D^0 decay modes as well as two bins of B charge (B^+ and B^-), two bins of K^0_S reconstruction type (LL and DD) and two bins of data type (Run 1 and Run 2), resulting in 56 samples in total. The parameters extracted from the simultaneous fit are the *CP* observables: $A_{K\pi}$, A_{KK}, $A_{\pi\pi}$, R_{KK}, $R_{\pi\pi}$, $R^+_{K\pi}$, $R^-_{K\pi}$, $A_{K\pi\pi\pi}$, $A_{\pi\pi\pi\pi}$, $R_{\pi\pi\pi\pi}$, $R^+_{K\pi\pi\pi}$ and $R^-_{K\pi\pi\pi}$, which relate to the physics parameters of interest, as defined in Eqs. 2.41 - 2.45. Since the *CP* observables are measured from the ratios of yields in different D^0 modes and different B meson charges, it is necessary to separate the corresponding data samples before fitting. By performing the fit to these data samples simultaneously, parameters can be constrained in the higher yielding modes and shared in the other modes.

The simultaneous fit extracts the *CP* observables directly, rather than measuring the pure yields and subsequently converting them into the *CP* observables. This strategy avoids the need to deal with combining results from different categories, which is complicated due to the many correlations between variables.

5.2.1 Asymmetry corrections

Raw asymmetries calculated directly from the yields contain contributions from several effects. Of primary importance is the physics asymmetry due to *CP* violation, A_{phys}, which is the physical parameter to be measured. However, it

is also necessary to consider and correct for other sources of asymmetry that would affect the measurement:

- the production asymmetry A_{prod} comes from the difference in the production rate of B^+ compared to B^- mesons in the pp collisions; and
- the detection asymmetry A_{det} comes from the difference in efficiency of the detector for detecting a positively charged particle compared to a negatively charge particle.

These asymmetries all contribute to produce the raw observed asymmetry measured in data, A_{raw}. Assuming that the asymmetries are small, the physical asymmetry is given by,

$$A_{\text{phys}} = A_{\text{raw}} - A_{\text{prod}} - A_{\text{det}} \ . \tag{5.2}$$

The detection asymmetry also affects the charge-dependent yield ratios in the ADS modes.

Production asymmetry

The $B^{\pm}$ production asymmetry is estimated from LHCb Run 1 data, binned in p and η, using $B^+ \to \overline{D}^0\pi^+$ decays [71]. The production asymmetry for $B^- \to DK^{*-}$ is $A_{\text{prod}} = (-0.54 \pm 0.54) \times 10^{-2}$ and is calculated by performing a weighted average based on the p and η distribution in simulated signal samples. This value for the production asymmetry is consistent with zero as expected. The equivalent result for Run 2 data is not currently available, therefore the production asymmetry for Run 2 is taken to have the same central value as Run 1 in the absence of other information.

Detection asymmetry

The detection asymmetry arises from differences in interactions of matter and antimatter particles with the matter detector. The $B^- \to DK^{*-}$ decay contains a final state consisting of purely pions and kaons, therefore the pion and kaon detection asymmetry are the values of interest. The pion detection asymmetry is

consistent with zero and has been measured at LHCb to be $(0.08 \pm 0.30)\%$ [72]. However, for the kaon asymmetry the best measured value at LHCb is the $K\pi$ asymmetry difference $A_{\rm det}^{K\pi} = A_{\rm det}^{K} - A_{\rm det}^{\pi}$, where $A_{\rm det}^{K}$ is the kaon asymmetry and $A_{\rm det}^{\pi}$ is the pion asymmetry. The $K\pi$ asymmetry has been measured in bins of kaon momentum [73], therefore the value of $A_{\rm det}^{K\pi}$ for $B^- \to DK^{*-}$ is calculated by performing a weighted average based on the kaon momentum distribution in the simulated signal sample. The value of $A_{\rm det}^{K\pi}$ thus obtained is $(-1.06 \pm 0.16)\%$. Both $A_{\rm det}^{\pi}$ and $A_{\rm det}^{K\pi}$ values are obtained using Run 1 data. The changes to the detector between the data-taking periods are not expected to significantly affect the $A_{\rm det}$ measurement, therefore the same results are applied to both Run 1 and Run 2 data.

The detection asymmetry must be corrected for any *CP* observable that is sensitive to the charge of the B meson decay. Therefore, it affects both the asymmetries and the yield ratios in the ADS modes, which are considered separately for B^- and B^+. The correction varies for the different *CP* observables, depending on the number of charged kaons and pions in the final state and the structure of the *CP* observable being measured, as summarised in Table 5.3. The correction for the asymmetries is additive as seen by Eq. 5.2, however when dealing with the yield ratios, the correction is a ratio of efficiencies, which must be multiplied by the raw yield ratio to correct for the detection asymmetry effect.

Observable	Mode	Detection asymmetry	In terms of $A_{\rm det}^{K\pi}$
$A_{K\pi}$	$B^\pm \to [K^\pm\pi^\mp]_D[K_s^0\pi^\pm]_{K^*}$	$A_{\rm det}^K - A_{\rm det}^\pi + A_{\rm det}^\pi$	$A_{\rm det}^{K\pi} + A_{\rm det}^\pi$
A_{KK}	$B^\pm \to [K^\pm K^\mp]_D[K_s^0\pi^\pm]_{K^*}$	$A_{\rm det}^K - A_{\rm det}^K + A_{\rm det}^\pi$	$A_{\rm det}^\pi$
$A_{\pi\pi}$	$B^\pm \to [\pi^\pm\pi^\mp]_D[K_s^0\pi^\pm]_{K^*}$	$A_{\rm det}^\pi - A_{\rm det}^\pi + A_{\rm det}^\pi$	$A_{\rm det}^\pi$
$R_{K\pi}^+$	$B^+ \to [K^-\pi^+]_D[K_s^0\pi^+]_{K^*}$	$\epsilon_{K^+\pi^-}/\epsilon_{K^-\pi^+}$	$2A_{\rm det}^{K\pi} + 1$
$R_{K\pi}^-$	$B^- \to [K^+\pi^-]_D[K_s^0\pi^-]_{K^*}$	$\epsilon_{K^-\pi^+}/\epsilon_{K^+\pi^-}$	$1/(2A_{\rm det}^{K\pi} - 1)$
$A_{K\pi\pi\pi}$	$B^\pm \to [K^\pm\pi^\mp\pi^\pm\pi^\mp]_D[K_s^0\pi^\pm]_{K^*}$	$A_{\rm det}^K - A_{\rm det}^\pi + A_{\rm det}^\pi - A_{\rm det}^\pi + A_{\rm det}^\pi$	$A_{\rm det}^{K\pi} + A_{\rm det}^\pi$
$A_{\pi\pi\pi\pi}$	$B^\pm \to [\pi^\pm\pi^\mp\pi^\pm\pi^\mp]_D[K_s^0\pi^\pm]_{K^*}$	$A_{\rm det}^\pi - A_{\rm det}^\pi + A_{\rm det}^\pi - A_{\rm det}^\pi + A_{\rm det}^\pi$	$A_{\rm det}^\pi$
$R_{K\pi\pi\pi}^+$	$B^+ \to [K^-\pi^+\pi^-\pi^+]_D[K_s^0\pi^+]_{K^*}$	$\epsilon_{K^+\pi^-}/\epsilon_{K^-\pi^+}$	$2A_{\rm det}^{K\pi} + 1$
$R_{K\pi\pi\pi}^-$	$B^- \to [K^+\pi^-\pi^+\pi^-]_D[K_s^0\pi^-]_{K^*}$	$\epsilon_{K^-\pi^+}/\epsilon_{K^+\pi^-}$	$1/(2A_{\rm det}^{K\pi} - 1)$

Table 5.3: Detection asymmetry factors for each of the observables in the *CP* fit.

5.2.2 Efficiency corrections to yield ratios

The *CP* observables related to the ratio of yields, R_{KK}, $R_{\pi\pi}$, $R_{K\pi}^+$, $R_{K\pi}^-$, $R_{\pi\pi\pi\pi}$, $R_{K\pi\pi\pi}^+$ and $R_{K\pi\pi\pi}^-$, are physical quantities, which are independent of the detec-

tion and selection strategies employed. Therefore, in order to extract these *CP* observables from the raw yield ratios, various efficiency corrections, taken from simulated signal samples, must be applied.

For the GLW and qGLW modes, efficiency corrections are applied to the raw value of the yield ratios to extract R_{KK}, $R_{\pi\pi}$ and $R_{\pi\pi\pi\pi}$, given by

$$R_{hh} = \frac{N(B^- \to D(h^+h^-)K^{*-})}{N(B^- \to D(K^-\pi^+)K^{*-})} \times \frac{\mathcal{B}(D^0 \to K^-\pi^+)}{\mathcal{B}(D^0 \to hh)} \times \frac{\epsilon_{\rm sel}(K\pi)}{\epsilon_{\rm sel}(hh)} \times \frac{\epsilon_{\rm pid}(K\pi)}{\epsilon_{\rm pid}(hh)} \ , \tag{5.3}$$

$$R_{\pi\pi\pi\pi} = \frac{N(B^- \to D(\pi^+\pi^-\pi^+\pi^-)K^{*-})}{N(B^- \to D(K^-\pi^+\pi^-\pi^+)K^{*-})} \times \frac{\mathcal{B}(D^0 \to K^-\pi^+\pi^-\pi^+)}{\mathcal{B}(D^0 \to \pi\pi\pi\pi)} \times \frac{\epsilon_{\rm sel}(K\pi\pi\pi)}{\epsilon_{\rm sel}(\pi\pi\pi\pi)} \times \frac{\epsilon_{\rm pid}(K\pi\pi\pi)}{\epsilon_{\rm pid}(\pi\pi\pi\pi)} \ , \tag{5.4}$$

where $\epsilon_{\rm sel}$ and $\epsilon_{\rm pid}$ are the selection and PID efficiencies respectively. Since PID variables are poorly modelled in the LHCb simulation, a separate, data-driven method for determining PID efficiencies is employed, as detailed later in this section.

The final states in the ADS modes are almost identical to the corresponding charge favoured modes, and therefore the selection efficiencies that are common to both are assumed to cancel. There are only two differences between the selection for the ADS mode and the charge favoured mode: the tighter BDT selection for DD candidates and the double misidentification veto, discussed in Secs. 4.1.4 and 4.1.3 respectively. Both of these are only applied to the ADS mode. The efficiency corrections required to extract $R^+_{K\pi}$, $R^-_{K\pi}$, $R^+_{K\pi\pi\pi}$ and $R^-_{K\pi\pi\pi}$ from the raw yield ratios are then given by,

$$R^\pm_{K\pi} = \frac{N(B^\pm \to D(K^\mp\pi^\pm)K^{*\pm})}{N(B^\pm \to D(K^\pm\pi^\mp)K^{*\pm})} \times \frac{\epsilon_{\rm bdt}(K\pi)}{\epsilon_{\rm bdt}(\pi K)} \times \frac{1}{\epsilon_{\rm veto}(\pi K)} \times A_{\rm det}(\pi K) \ , \tag{5.5}$$

$$R^\pm_{K\pi\pi\pi} = \frac{N(B^\pm \to D(K^\mp\pi^\pm\pi^\mp\pi^\pm)K^{*\pm})}{N(B^\pm \to D(K^\pm\pi^\mp\pi^\pm\pi^\mp)K^{*\pm})} \times \frac{\epsilon_{\rm bdt}(K\pi\pi\pi)}{\epsilon_{\rm bdt}(\pi K\pi\pi)} \times \frac{1}{\epsilon_{\rm veto}(\pi K\pi\pi)} \times A_{\rm det}(\pi K\pi\pi) \ , \tag{5.6}$$

where $\epsilon_{\rm bdt}$ and $\epsilon_{\rm veto}$ are the BDT and veto efficiencies respectively, and $A_{\rm det}$ is the detection asymmetry correction discussed in Sec. 5.2.1.

The *CP* observables relating to the yield ratios R_{KK}, $R_{\pi\pi}$, $R^+_{K\pi}$, $R^-_{K\pi}$ $R_{\pi\pi\pi\pi}$, $R^+_{K\pi\pi\pi}$ and $R^-_{K\pi\pi\pi}$ are extracted from the *CP* fit with all the above efficiency corrections applied.

Signal efficiencies from simulation

The signal efficiency, ϵ_{sel}, is defined as the probability that a true signal candidate passes the full selection imposed, including acceptance and trigger requirements. This is extracted from samples of simulated signal events by calculating the number of events that pass the selection as a fraction of those generated. The values are then used as fixed inputs in the *CP* fit according to Eqs. 5.3 and 5.4. These values have been calculated separately for Run 1 and Run 2 samples as well as LL and DD categories, as shown in Table 5.4. It can be seen that the Run 2 efficiencies are consistently higher than Run 1, which is attributed to the changes in the trigger between the two running periods, such as the lowering of momentum thresholds.

	Run 1		Run 2	
	LL	DD	LL	DD
$\epsilon_{\text{sel}}(K\pi)$	0.0939 ± 0.0011	0.2519 ± 0.0018	0.1266 ± 0.0011	0.3155 ± 0.0017
$\epsilon_{\text{sel}}(KK)$	0.0919 ± 0.0011	0.2450 ± 0.0018	0.1189 ± 0.0010	0.2923 ± 0.0016
$\epsilon_{\text{sel}}(\pi\pi)$	0.1015 ± 0.0012	0.2584 ± 0.0018	0.1292 ± 0.0011	0.3309 ± 0.0017
$\epsilon_{\text{sel}}(K\pi\pi\pi)$	0.0288 ± 0.0006	0.0816 ± 0.0020	0.0484 ± 0.0004	0.1229 ± 0.0007
$\epsilon_{\text{sel}}(\pi\pi\pi\pi)$	0.0272 ± 0.0013	0.0825 ± 0.0022	0.0436 ± 0.0011	0.1185 ± 0.0017

Table 5.4: Summary of the selection efficiencies used in the *CP* fit.

The BDT signal efficiency, defined as the probability that a true signal event passes the BDT selection imposed, is calculated as the number of events that pass the BDT selection compared to the number that already pass the stripping and mass requirements. The results are given in Table 5.5. These efficiencies, obtained from samples of simulated signal events, are used as fixed inputs in the *CP* fit according to Eqs. 5.5 and 5.6.

	Run 1		Run 2	
	LL	DD	LL	DD
$\epsilon_{\text{bdt}}(K\pi)$	0.947 ± 0.005	0.896 ± 0.004	0.949 ± 0.003	0.907 ± 0.002
$\epsilon_{\text{bdt}}(\pi K)$	0.947 ± 0.005	0.802 ± 0.005	0.949 ± 0.003	0.826 ± 0.003
$\epsilon_{\text{bdt}}(K\pi\pi\pi)$	0.938 ± 0.010	0.903 ± 0.007	0.952 ± 0.003	0.928 ± 0.002
$\epsilon_{\text{bdt}}(\pi K\pi\pi)$	0.938 ± 0.010	0.838 ± 0.009	0.952 ± 0.003	0.870 ± 0.003

Table 5.5: Summary of the BDT efficiencies used in the *CP* fit.

PID efficiencies

The selections for the different D^0 decays modes are almost identical apart from the PID requirements. The PID power of the detector for hadrons originates primarily from the RICH detectors [50, 51]. As PID variables are poorly modelled in LHCb simulation, the efficiencies for the various PID selections are determined from data using calibration samples containing a known particle type for protons, kaons and pions, *e.g.* $D^0 \to K^-\pi^+$ and $K^0_S \to \pi^-\pi^+$. The PID efficiency varies as a function of momentum and pseudorapidity, therefore when calculating the PID efficiency for a specific decay channel, the calibration sample is reweighted based on the momentum and pseudorapidity distribution of the signal candidates. The uncertainties in the PID efficiencies originate from the limited size of the calibration samples, the limited size of the simulated signal samples, the reweighting procedure itself and the purity of the calibration samples.

The PID efficiencies are calculated individually for each year of data-taking and each magnet polarity and are subsequently combined according to the efficiency-corrected yields in each of the samples. The results of the PID efficiencies are given in Table 5.6. These efficiencies are used as fixed inputs in the *CP* fit as described by Eqs. 5.3 and 5.4.

	Run 1		Run 2	
	LL	DD	LL	DD
$\epsilon_{\text{pid}}(K\pi)$	0.734 ± 0.002	0.747 ± 0.002	0.811 ± 0.002	0.821 ± 0.002
$\epsilon_{\text{pid}}(KK)$	0.812 ± 0.002	0.825 ± 0.002	0.844 ± 0.002	0.853 ± 0.002
$\epsilon_{\text{pid}}(\pi\pi)$	0.670 ± 0.002	0.676 ± 0.002	0.779 ± 0.002	0.790 ± 0.002
$\epsilon_{\text{pid}}(K\pi\pi\pi)$	0.630 ± 0.002	0.636 ± 0.002	0.784 ± 0.002	0.798 ± 0.002
$\epsilon_{\text{pid}}(\pi\pi\pi\pi)$	0.675 ± 0.002	0.687 ± 0.002	0.822 ± 0.002	0.835 ± 0.002

Table 5.6: Summary of the PID efficiencies used in the *CP* fit.

It can be seen from Table 5.6 that the PID efficiency in Run 2 is higher than Run 1 for the PID selection used in this analysis. This is primarily due to the removal of the aerogel radiator in Run 2, which is discussed in Sec. 3.3.

Veto efficiencies

Another input to the fit is the efficiency of the double misidentification veto used in Eqs. 5.5 and 5.6. The veto efficiency, defined as the probability that a true signal event survives the veto selection, is calculated as the ratio of the number of events in data that pass the veto selection to the number that pass the rest of the selection. [1] The values of the veto efficiencies are given in Table 5.7.

	Run 1		Run 2	
	LL	DD	LL	DD
$\epsilon_{\text{veto}}(\pi K)$	0.905 ± 0.009	0.919 ± 0.005	0.915 ± 0.007	0.917 ± 0.004
$\epsilon_{\text{veto}}(\pi K \pi\pi)$	0.895 ± 0.005	0.882 ± 0.003	0.916 ± 0.003	0.906 ± 0.002

Table 5.7: Summary of the veto efficiencies used in the *CP* fit.

5.2.3 Likelihood function

An extended maximum likelihood fit, as described in Sec. 4.2.1, is used to extract the *CP* observables. A likelihood is assigned to each candidate in a given category by constructing the signal and background PDFs. The total extended log-likelihood, $\log \mathcal{L}_{\text{tot}}$, is the sum of the extended log-likelihoods for the individual candidates in each of the different categories: B charge ($\{+, -\}$, indexed q), K^0_{S} reconstruction type ($\{\text{LL, DD}\}$, indexed t), data type ($\{\text{Run 1, Run 2}\}$, indexed r) and D^0 decay mode ($\{K^-\pi^+,\ K^-K^+,\ \pi^-\pi^+,\ \pi^-K^+,\ K^-\pi^+\pi^-\pi^+,\ \pi^-\pi^+\pi^-\pi^+,\ \pi^-K^+\pi^-\pi^+\ \}$, indexed m). This is described by

$$\log \mathcal{L}_{\text{tot}} = \sum_m \sum_q \sum_t \sum_r \left[\sum_{x_i} \log \mathcal{L}^q_{m,t,r}\left(\theta, N; x_i\right) \right] , \tag{5.7}$$

where θ are the set of parameters that describe the shapes of the PDFs in the model,

$$\theta = \{\mu_{\text{two-body}}, \sigma_{\text{two-body}}, \mu_{\text{four-body}}, \sigma_{\text{four-body}}, \beta_{\text{two-body LL}}, \beta_{\text{two-body DD}}, \beta_{\text{four-body LL}}, \beta_{\text{four-body DD}}\} , \tag{5.8}$$

[1] For the four-body modes, the efficiency is calculated by comparing the numbers that pass the selection before BDT and PID requirements. This inconsistency results in smaller uncertainties on the four-body veto efficiencies as these are calculated from a larger sample, however it has no significant effect on the final results.

and N are the set of parameters relating to the expected number of events described by each PDF,

$$N = \{A_{K\pi}, A_{KK}, A_{\pi\pi}, A_{K\pi\pi\pi}, A_{\pi\pi\pi\pi}, R_{KK}, R_{\pi\pi}, R^{+}_{K\pi}, R^{-}_{K\pi}, R_{\pi\pi\pi\pi}, R^{+}_{K\pi\pi\pi}, R^{-}_{K\pi\pi\pi}, \{N_{K\pi,t,r}\}, \{N_{K\pi\pi\pi,t,r}\}, \{N^{q}_{comb,m,t,r}\}\} \ . \quad (5.9)$$

Here $N_{m,t,r}$ refers to the expected signal yield summed over charge in the bin and $N^{q}_{comb,m,t,r}$ refers to the expected combinatorial yield in each of the 56 bins. The parameter x_i is the reconstructed mass of a given candidate i.

The extended likelihood for each bin is constructed from the model containing the signal, combinatorial and partially reconstructed PDFs: $P_{\rm sig}$, $P_{\rm comb}$ and $P_{\rm partreco}$, respectively, and information about the expected number of events described by each of the PDFs, as described in Sec. 4.2. The extended likelihood functions for each of the bins is given by:

$$\mathcal{L}^{\pm}_{K\pi,t,r} = \frac{1}{2}\boldsymbol{N}_{\mathbf{K\pi,t,r}}\left(1 \mp \mathbf{A}_{\mathbf{K\pi,raw}}\right) P_{\rm sig}\left(\boldsymbol{\mu}_{\mathbf{two\text{-}body}}, \boldsymbol{\sigma}_{\mathbf{two\text{-}body}}\right) + \boldsymbol{N}^{\pm}_{\mathbf{comb,K\pi,t,r}} P_{\rm comb}\left(\boldsymbol{\beta}_{\mathbf{two\text{-}body,\ t}}\right) + \frac{1}{2} N_{{\rm partreco},K\pi,t,r} P_{{\rm partreco},t} \quad (5.10)$$

$$\mathcal{L}^{\pm}_{KK,t,r} = \frac{1}{2}\boldsymbol{N}_{\mathbf{K\pi,t,r}}\left(1 \mp \boldsymbol{A}_{\mathbf{KK,raw}}\right) \boldsymbol{R}_{\mathbf{KK,raw}} P_{\rm sig}\left(\boldsymbol{\mu}_{\mathbf{two\text{-}body}}, \boldsymbol{\sigma}_{\mathbf{two\text{-}body}}\right) + \boldsymbol{N}^{\pm}_{\mathbf{comb,KK,t,r}} P_{\rm comb}\left(\boldsymbol{\beta}_{\mathbf{two\text{-}body,\ t}}\right) + \frac{1}{2} N_{{\rm partreco},KK,t,r} P_{{\rm partreco},t} + \boldsymbol{N}_{\mathbf{K\pi,t,r}} \mathbf{f}_{\boldsymbol{\Lambda}} P_{\Lambda} \quad (5.11)$$

$$\mathcal{L}^{\pm}_{\pi\pi,t,r} = \frac{1}{2}\boldsymbol{N}_{\mathbf{K\pi,t,r}}\left(1 \mp \mathbf{A}_{\mathbf{\pi\pi,raw}}\right) \mathbf{R}_{\mathbf{\pi\pi,raw}} P_{\rm sig}\left(\boldsymbol{\mu}_{\mathbf{two\text{-}body}}, \boldsymbol{\sigma}_{\mathbf{two\text{-}body}}\right) + \boldsymbol{N}^{\pm}_{\mathbf{comb},\pi\pi,\mathbf{t,r}} P_{\rm comb}\left(\boldsymbol{\beta}_{\mathbf{two\text{-}body,\ t}}\right) + \frac{1}{2} N_{{\rm partreco},\pi\pi,t,r} P_{{\rm partreco},t} \quad (5.12)$$

$$\mathcal{L}^{\pm}_{\pi K,t,r} = \frac{1}{2}\boldsymbol{N}_{\mathbf{K\pi,t,r}}\left(1 \mp \mathbf{A}_{\mathbf{K\pi,raw}}\right) \boldsymbol{R}^{\pm}_{\mathbf{K\pi,raw}} P_{\rm sig}\left(\boldsymbol{\mu}_{\mathbf{two\text{-}body}}, \boldsymbol{\sigma}_{\mathbf{two\text{-}body}}\right) + \boldsymbol{N}^{\pm}_{\mathbf{comb},\pi\mathbf{K},\mathbf{t,r}} P_{\rm comb}\left(\boldsymbol{\beta}_{\mathbf{two\text{-}body,\ t}}\right) + \frac{1}{2} N_{{\rm partreco},\pi K,t,r} P_{{\rm partreco},t} \quad (5.13)$$

$$\mathcal{L}^{\pm}_{K\pi\pi\pi,t,r} = \frac{1}{2}\boldsymbol{N}_{\mathbf{K\pi\pi\pi,t,r}}\left(1 \mp \boldsymbol{A}_{\mathbf{K\pi\pi\pi,raw}}\right) P_{\rm sig}\left(\boldsymbol{\mu}_{\mathbf{four\text{-}body}}, \boldsymbol{\sigma}_{\mathbf{four\text{-}body}}\right) + \boldsymbol{N}^{\pm}_{\mathbf{comb,K\pi\pi\pi,t,r}} P_{\rm comb}\left(\boldsymbol{\beta}_{\mathbf{four\text{-}body,\ t}}\right) + \frac{1}{2} N_{{\rm partreco},K\pi\pi\pi,t,r} P_{{\rm partreco},t} \quad (5.14)$$

$$\mathcal{L}^{\pm}_{\pi\pi\pi\pi,t,r} = \frac{1}{2}\boldsymbol{N}_{\mathbf{K\pi\pi\pi,t,r}}\left(1 \mp \boldsymbol{A}_{\pi\pi\pi\pi,\mathbf{raw}}\right)\boldsymbol{R}_{\pi\pi\pi\pi,\mathbf{raw}}P_{\rm sig}\left(\boldsymbol{\mu}_{\mathbf{four\text{-}body}},\boldsymbol{\sigma}_{\mathbf{four\text{-}body}}\right) + \boldsymbol{N}^{\pm}_{\mathbf{comb},\pi\pi\pi\pi,\mathbf{t},\mathbf{r}}P_{\rm comb}\left(\boldsymbol{\beta}_{\mathbf{four\text{-}body,\ t}}\right) + \frac{1}{2}N_{\rm partreco,\pi\pi\pi\pi,t,r}P_{{\rm partreco},t} \quad (5.15)$$

$$\mathcal{L}^{\pm}_{\pi K\pi\pi,t,r} = \frac{1}{2}\boldsymbol{N}_{\mathbf{K\pi\pi\pi,t,r}}\left(1 \mp \boldsymbol{A}_{\mathbf{K\pi\pi\pi,raw}}\right)\boldsymbol{R}^{\pm}_{\mathbf{K\pi\pi\pi,raw}}P_{\rm sig}\left(\boldsymbol{\mu}_{\mathbf{four\text{-}body}},\boldsymbol{\sigma}_{\mathbf{four\text{-}body}}\right) + \boldsymbol{N}^{\pm}_{\mathbf{comb},\pi\mathbf{K}\pi\pi,\mathbf{t},\mathbf{r}}P_{\rm comb}\left(\boldsymbol{\beta}_{\mathbf{four\text{-}body,\ t}}\right) + \frac{1}{2}N_{\rm partreco,\pi K\pi\pi,t,r}P_{{\rm partreco},t} \quad (5.16)$$

where the parameters in bold are measured in the fit and the index $\pm$ refers to the different bins of B charge. The signal yields are constructed as a function of the asymmetries, yield ratios and yields in the favoured mode, therefore it is these quantities that are freely varying parameters to be optimised in the *CP* fit. The combinatorial yields in each of the 56 bins are included as freely-varying parameters, however the partially reconstructed yields, $N_{{\rm partreco},m,t,r}$, which are summed over charge in each bin, are fixed as described in Sec. 5.1.2. The parameters $A_{m,\rm raw}$ and $R_{m,\rm raw}$ are the raw asymmetries and yield ratios without any of the corrections discussed in Secs. 5.2.1 and 5.2.2 applied. The parameters relate to the *CP* observables by

$$A_{m,\rm raw} = A_m - A_{\rm prod} - A_{m,\rm det}\ , \quad (5.17)$$

$$R^{(\pm)}_{m,\rm raw} = \epsilon_{m,\rm corr}R^{(\pm)}_m\ , \quad (5.18)$$

where $\epsilon_{m,\rm corr}$ refers to the relevant efficiency correction given in Eqs. 5.3 - 5.6, and $A_{m,\rm det}$ refers to the mode-dependent corrections due to the detection asymmetry given in Table 5.3.

5.2.4 Optimisation of BDT and K^* selection

To select $B^- \to DK^{*-}$ events, a BDT is implemented and selection requirements are applied to the K^{*-} mass and $K^0_{\rm S}$ helicity angle to preferentially select events that proceed via a K^{*-} meson, as described in Sec. 4.1. These selection requirements are optimised simultaneously with the aim of minimising the uncertainty on the *CP* observables.

In order to perform the optimisation procedure, "pseudo-experiments" are carried out to estimate the expected uncertainty on the *CP* observables for different selection requirements. For a single pseudo-experiment, samples are generated for each of the *CP* fit categories based on the model used for the *CP* fit. The signal, combinatorial and partially reconstructed expected yields for the two- and four-body favoured D^0 decay modes are extracted by performing a single fit to data, as described below. The expected yields in the other D^0 decay modes are extracted using the yield ratios and asymmetries which are calculated based on the physics parameters, r_B, δ_B and γ, using Eqs. 2.41 - 2.45. For this study, values of $r_B = 0.1$, $\delta_B = 150^\circ$ and $\gamma = 70^\circ$ are assumed, where γ and r_B are consistent with the current world averages [15].[2] An equal combinatorial background rate is generated in each of the D^0 decay modes and spilt equally between B^- and B^+ categories. Then by performing the *CP* fit to the generated data, the *CP* observables and their uncertainties can be extracted. Within a single pseudo-experiment this generation and fitting process is repeated 1000 times, where each time the generated yields take a different value, drawn from a Poisson distribution with a mean of the corresponding expected yield. Therefore, each pseudo-experiment results in a distribution of each *CP* observable as well as a corresponding uncertainty distribution. The value of the expected uncertainty for a given *CP* observable is taken to be the mean of its uncertainty distribution.

Pseudo-experiments are performed for a range of different selections, which are

- The reconstructed K^{*-} mass lies within 50 MeV/c^2, 75 MeV/c^2 or 100 MeV/c^2 of the known K^{*-} mass,
- The magnitude of $\cos(\theta_{K^0_S})$ is greater than 0, 0.1, 0.2, 0.3 or 0.4,
- The BDT classifier is greater than -0.8, -0.6, -0.4, -0.2, 0, 0.2, 0.4, 0.6, 0.7, 0.8, 0.9 or 0.95.

To calculate the appropriate expected yields for each selection requirement in the favoured D^0 decay modes, the following procedure is performed. The selection

[2] Although the value of δ_B is completely unknown, the optimisation has been repeated for various values of δ_B and is found to be insensitive to this choice.

described in Sec. 4.1 is applied to data excluding any requirements on the K^{*-} mass or K^0_S helicity angle, and with only a loose BDT selection, requiring the BDT classifier to be greater than -0.8. With this setup, a single fit is performed to each of the two- and four-body favoured modes, similar to the fit in Sec. 4.2.5, to extract the signal, combinatorial and partially reconstructed yields for this loose selection. The signal and background efficiencies for each of the selection requirements listed above are calculated using simulated samples and high B^- mass data respectively. For a given pseudo-experiment, the expected signal and background yields are then estimated based on both the yields extracted using the loose selection, and the signal and background efficiencies for the selection requirement under investigation.

For optimising the selection for the GLW modes, the fit uncertainty was minimised for A_{KK}, R_{KK}, $A_{\pi\pi}$ and $R_{\pi\pi}$. As an example, Fig. 5.2 shows the fit uncertainty in R_{KK} as a function of the K^0_S helicity angle selection point, for different K^{*-} mass requirements. The minimum uncertainty is achieved by requiring the reconstructed K^{*-} mass to lie within 75 MeV/c^2 of the known K^{*-} mass and the magnitude of the K^0_S helicity angle to be greater than 0.3. A similar study is performed on the *CP* observables A_{KK}, $A_{\pi\pi}$ and $R_{\pi\pi}$, which show reasonable agreement with the same position of the minimum as indicated in Fig. 5.2; therefore the above K^{*-} requirements are chosen for the final selection. Similarly, the requirement on the BDT classifier for the GLW modes is chosen to be greater than 0.6 for LL candidates and 0.7 for DD candidates.

The BDT selection for the ADS modes was optimised to minimise the fit uncertainties in $R^+_{K\pi}$ and $R^-_{K\pi}$. Studies were performed to investigate a tighter BDT selection for the ADS mode as illustrated in Fig. 5.3, showing that the uncertainty in $R^+_{K\pi}$ continues to decrease as the BDT requirement is tightened. A tighter BDT cut of 0.9 in the ADS mode for DD candidates was chosen as it results in a lower uncertainty on $R^+_{K\pi}$ and $R^-_{K\pi}$ due to an increase in the background rejection from 93% to 98%, while retaining 80% of the signal. Although the uncertainty appears to decrease for a BDT cut of 0.95, this tighter selection results in a significant drop

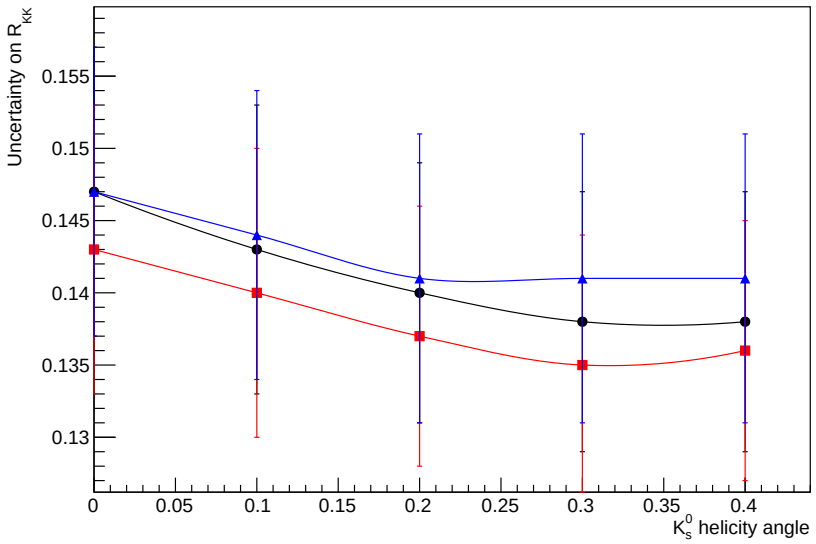

Figure 5.2: Value of the uncertainty on R_{KK} as a function of the K^0_S helicity angle selection for different K^* mass selections. The reconstructed K^{*-} mass is required to lie within 50 MeV/c^2 (blue), 75 MeV/c^2 (red), or 100 MeV/c^2 (black) of the known K^* mass.

in signal efficiency to 73%. The small drop in uncertainty between 0.9 and 0.95 is statistically insignificant and does not justify such a large drop in signal efficiency.

In summary, the final selection chosen is:

- The reconstructed K^{*-} mass must lie within 75 MeV/c^2 of the known K^{*-} mass.
- The magnitude of $\cos(\theta_{K^0_S})$ is required to be greater than 0.3.
- The BDT classifier is required to be greater than 0.6 for LL candidates and greater than 0.7 for DD candidates, except in the ADS mode where it is required to be greater than 0.6 for LL candidates and 0.9 for DD candidates.

As mentioned earlier, the pseudo-experiments described in this section were originally generated with an equal combinatorial rate in each of the D^0 decay modes. However, a significantly lower combinatorial rate is observed in data in the ADS modes compared to the corresponding favoured $B^- \to D(K^-\pi^+)K^{*-}$ and $B^- \to D(K^-\pi^+\pi^-\pi^+)K^{*-}$ decay channels. Consequently, the sensitivity to changes in the combinatorial rate were investigated, and showed the choice

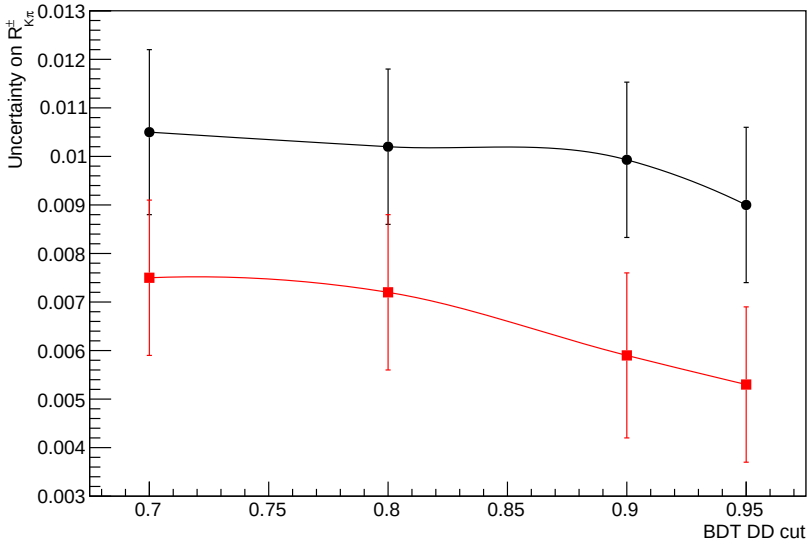

Figure 5.3: Value of the uncertainty on $R^{+}_{K\pi}$ (black) and $R^{-}_{K\pi}$ (red) as a function of BDT_DD cut in the ADS mode. These pseudo-experiments are run with a BDT_LL cut of 0.6 on all modes and BDT_DD cut of 0.7 on all modes other than the ADS.

of BDT selection for the ADS modes remained insensitive to a lower fraction of combinatorial background.

5.2.5 Fitter bias in *CP* fit

The validity of the *CP* fit is investigated by testing for any biases, incorrect determination of the uncertainties, or instabilities in the *CP* fit procedure. Pseudo-experiments are performed using the same procedure described in Sec. 5.2.4, however in this case they are based on the final selection values. The physics parameters $r_B = 0.1$, $\delta_B = 111°$ and $\gamma = 70°$ are used, where again the results are found to have little sensitivity to the chosen value of δ_B. The *CP* fit is performed on 1000 trials, where the value of each *CP* observable and its associated uncertainty is extracted. The validity of the fit is tested by observing the pull distribution of each fit parameter x, given by:

$$P_x = \begin{cases} \frac{x_{\rm fit} - x_{\rm gen}}{\sigma_x^-}, & \text{if } x_{\rm fit} - x_{\rm gen} > 0. \\ \frac{x_{\rm gen} - x_{\rm fit}}{\sigma_x^+}, & \text{if } x_{\rm fit} - x_{\rm gen} < 0. \end{cases}$$

where $x_{\rm fit}$ is the value of the parameter returned by the fit, $x_{\rm gen}$ is the generated value of the parameter, and σ_x^+ and σ_x^- are the upper and lower asymmetric

uncertainties respectively. These asymmetric uncertainties are determined as described in Sec. 4.2.1.

The pull distributions for each of the *CP* observables are shown in Fig. 5.4, where for each distribution a Gaussian fit is performed. All fitted Gaussians are consistent with a mean of zero and width of unity, which shows that the *CP* fit is unbiased and the uncertainties are correctly determined. Additionally, all fits converge, therefore the fit is stable.

5.3 Fit results

The *CP* fit is performed on data, with mass projections shown in Figs. 5.5 and 5.6. For ease of illustration, these projections are summed across all K^0_S reconstruction and data types after the fit is performed. From Fig. 5.5 a slight asymmetry between the B^+ and B^- decays can be observed in the $B^- \to D(K^-K^+)K^{*-}$ and $B^- \to D(\pi^-\pi^+)K^{*-}$ and $B^- \to D(\pi^-K^+)K^{*-}$ modes, with the asymmetry in the $B^- \to D(\pi^-K^+)K^{*-}$ mode occurring in with the opposite sign to the others. The four-body modes, shown in Fig. 5.6, display similar characteristics, but with fewer events. Using Eqs. 2.41 - 2.46, these observations indicate that the value of δ_B is expected to lie in the region satisfying $\sin\delta_B > 0$ and $\cos\delta_B > 0$.

Table 5.8 shows the *CP* fit results for the *CP* observables of interest. There is no significant asymmetry observed in the GLW and quasi-GLW modes, i.e. A_{KK}, $A_{\pi\pi}$ and $A_{\pi\pi\pi\pi}$ are all consistent with zero. However, asymmetry can be seen in the two-body ADS mode, where $R^+_{K\pi}$ is larger than $R^-_{K\pi}$ within statistical uncertainty. The four-body ADS mode shows a similar behaviour, however the asymmetry is less significant. It can also be seen that $A_{K\pi}$ and $A_{K\pi\pi\pi}$ are consistent with zero, as expected due to the very low level of interference in these modes. Additionally, A_{KK} and $A_{\pi\pi}$, and R_{KK} and $R_{\pi\pi}$, respectively are both in agreement with each other, which is consistent with expectation.

Table 5.9 shows the fit results for the favoured $B^- \to D(K^-\pi^+)K^{*-}$ and $B^- \to D(K^-\pi^+\pi^-\pi^+)K^{*-}$ signal yields and the shape parameters. It can be seen that both the peak positions and the widths of the signal peaks in the two- and

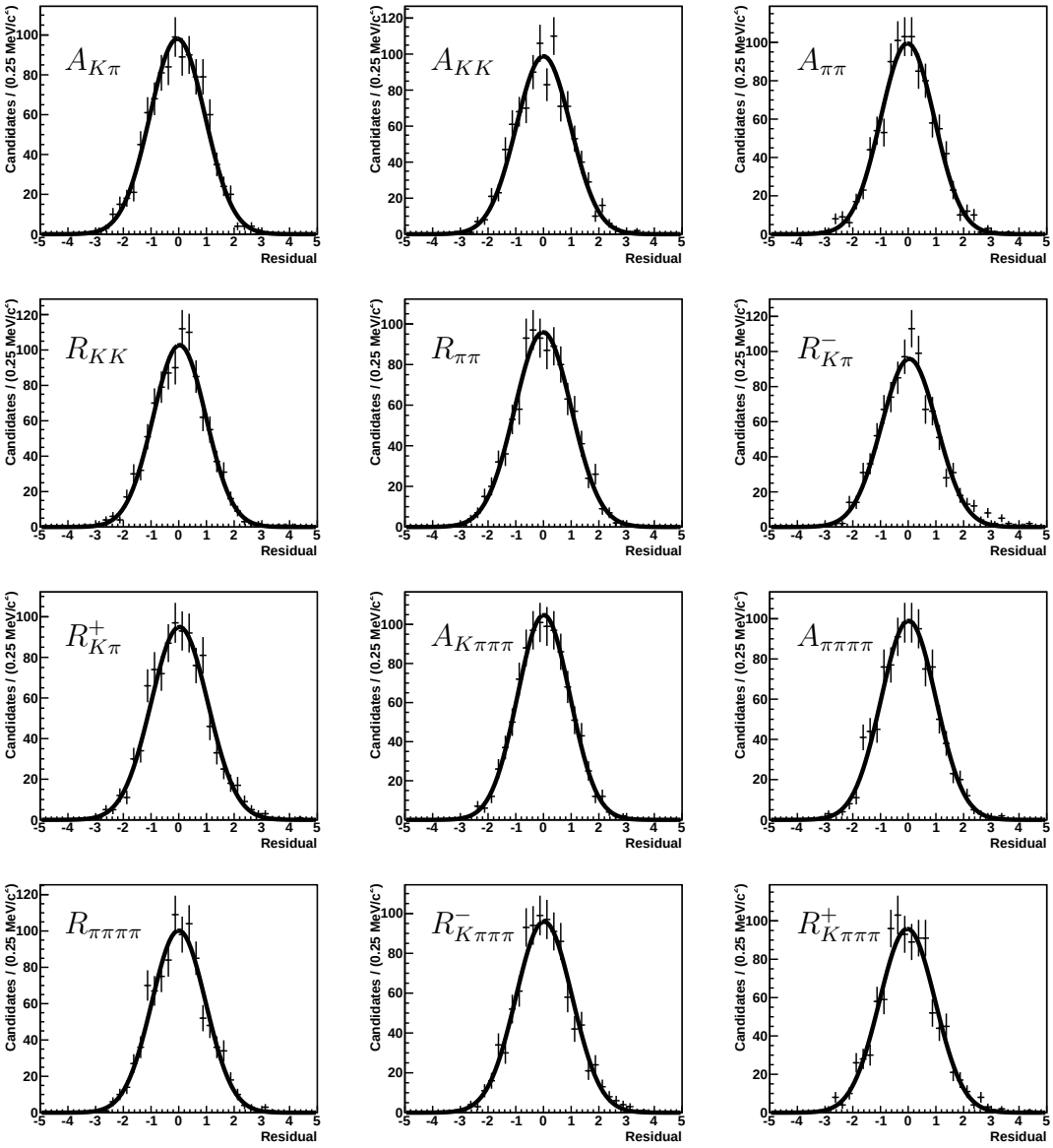

Figure 5.4: Pull distributions, P_x, from pseudo-experiments for all *CP* observables in the fit. The points represent the results from pseudo-experiments and the curves the fitted Gaussians.

four-body modes are consistent with each other. The yields are significantly higher in Run 2 compared to Run 1 even though the integrated luminosity of Run 2 is lower. In fact, the yield per unit of integrated luminosity is about 3 times higher in Run 2 compared to Run 1, which is driven by the increase in Run 2 centre-of-mass energy.

All the combinatorial yields are free to vary in the *CP* fit for each of the different bins, and they are found to be consistent between B^- and B^+, as expected. However, there is a significantly higher combinatorial yield in the $B^- \to D(K^-\pi^+)K^{*-}$ mode compared to the $B^- \to D(\pi^-K^+)K^{*-}$ mode. This difference is also observed between the $B^- \to D(K^-\pi^+\pi^-\pi^+)K^{*-}$ and $B^- \to D(K^+\pi^-\pi^+\pi^-)K^{*-}$ modes, but to a lesser extent. This observed difference in background level is consistent with a significant fraction of the combinatorial background coming from $B^- \to D\pi^-X$ decays combined with a real but unrelated K^0_S meson.

The fitted signal yields obtained from running the fit with B^+ and B^- samples combined are given in Table 5.10. When comparing the ratio of the two-body signal yields with the favoured mode, the results are consistent with the ratio of the branching fractions of the corresponding D^0 modes. For the four-body modes, the ratio of $B^- \to D(K^-\pi^+\pi^-\pi^+)K^{*-}$ to $B^- \to D(\pi^-\pi^+\pi^-\pi^+)K^{*-}$ signal yield is also consistent with the relative branching fractions.

Parameter	Fitted value	Negative uncertainty	Positive uncertainty
$A_{K\pi}$	-0.004	-0.023	0.023
A_{KK}	0.06	-0.07	0.07
$A_{\pi\pi}$	0.15	-0.13	0.13
R_{KK}	1.24	-0.08	0.09
$R_{\pi\pi}$	1.08	-0.14	0.15
$R^+_{K\pi}$	0.020	-0.006	0.006
$R^-_{K\pi}$	0.0018	-0.0032	0.0040
$A_{K\pi\pi\pi}$	-0.013	-0.031	0.031
$A_{\pi\pi\pi\pi}$	0.03	-0.11	0.11
$R_{\pi\pi\pi\pi}$	1.11	-0.12	0.13
$R^+_{K\pi\pi\pi}$	0.016	-0.006	0.008
$R^-_{K\pi\pi\pi}$	0.006	-0.005	0.006

Table 5.8: Fitted values of all the *CP* parameters from the *CP* fit.

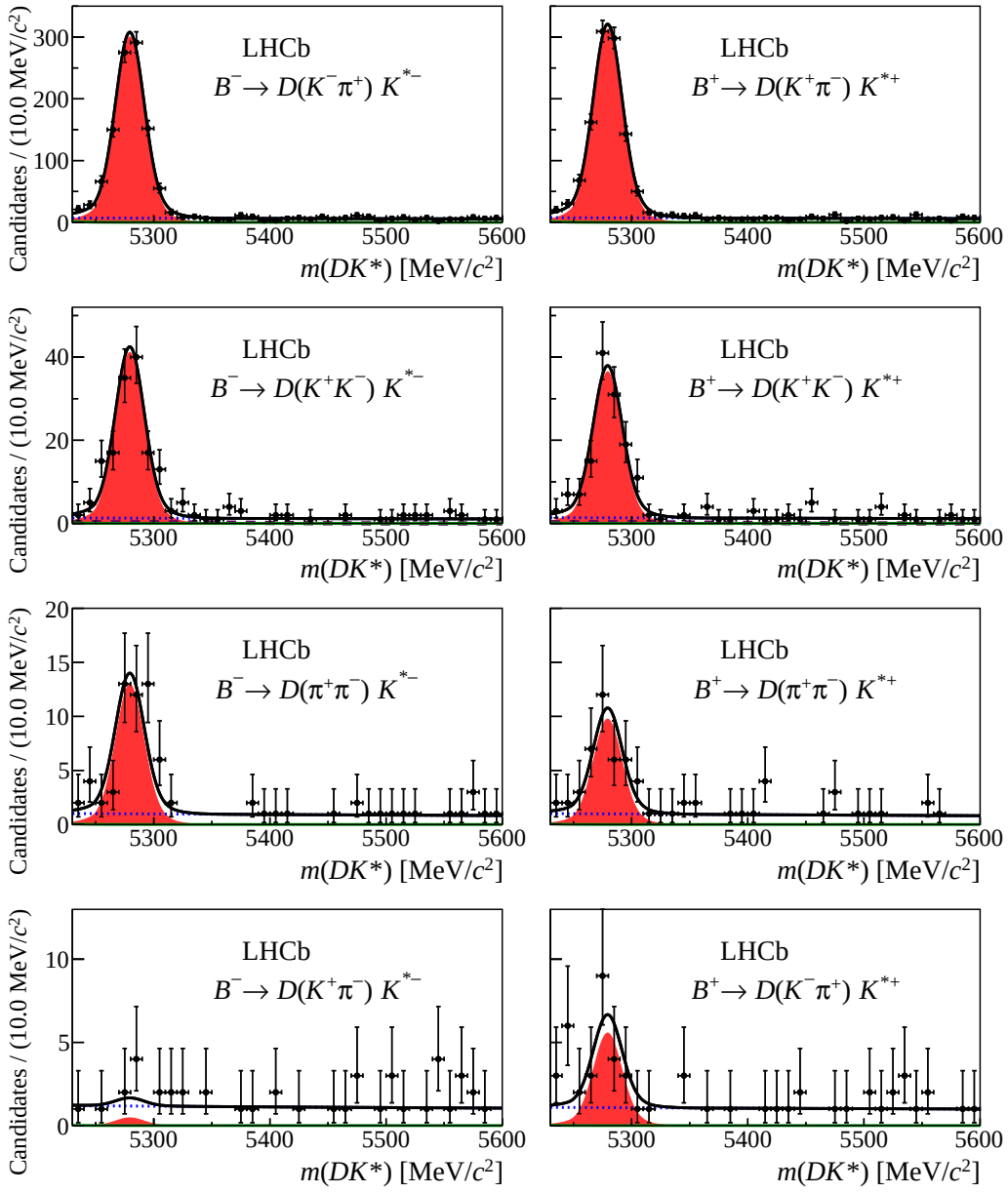

Figure 5.5: Results of the *CP* fit for the two-body modes, summed over all K^0_S reconstruction types and data-taking periods after the fit is performed, for B^+ (left) and B^- (right) decays. The signal is represented by the red shaded area, the combinatorial background by the dotted blue line and the partially reconstructed background by the solid green line. In the $B^- \to D(K^-K^+)K^{*-}$ fits, the $\Lambda_b^0 \to \Lambda_c^+ K^{*-}$ background is represented by the dashed purple line. The total fit is given by the black line.

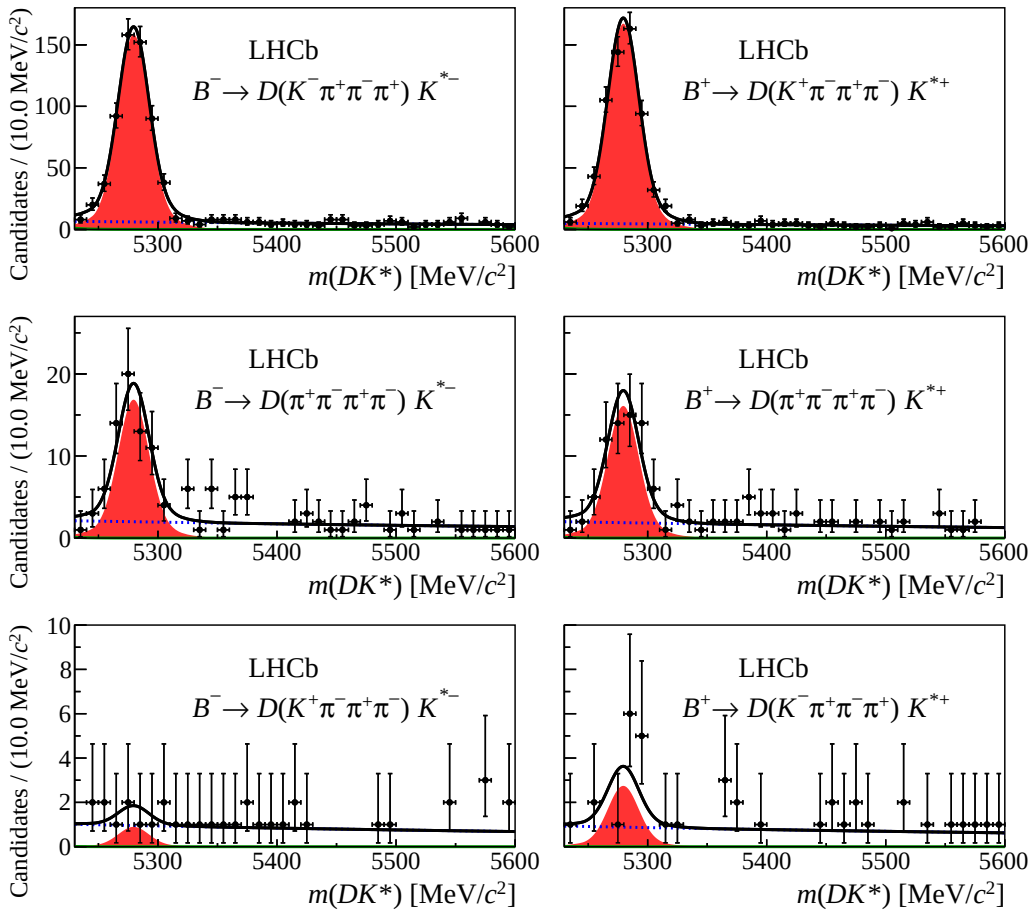

Figure 5.6: Results of the *CP* fit for the four-body modes, summed over all K^0_S reconstruction types and data-taking periods after the fit is performed, for B^+ (left) and B^- (right) decays. The signal is represented by the red shaded area, the combinatorial background by the dotted blue line and the partially reconstructed background by the solid green line. The total fit is given by the black line.

5.4 Systematic uncertainty

In addition to the statistical uncertainty, there is a systematic uncertainty arising from the assumptions involved in the construction and implementation of the model. In this section, various sources of systematic uncertainty that affect the measurements of the *CP* observables are investigated.

5.4.1 Sources of systematic uncertainty

Systematic uncertainties are calculated via two different methods. The method chosen in each case depends on the nature of the assumption being tested, as

Parameter	Fitted value	Negative uncertainty	Positive uncertainty
$N_{K\pi,\mathrm{DD,Run\ 1}}$	503	−22	23
$N_{K\pi,\mathrm{DD,Run\ 2}}$	911	−32	32
$N_{K\pi,\mathrm{LL,Run\ 1}}$	228	−14	15
$N_{K\pi,\mathrm{LL,Run\ 2}}$	388	−19	19
$N_{K\pi\pi\pi,\mathrm{DD,Run\ 1}}$	233	−15	16
$N_{K\pi\pi\pi,\mathrm{DD,Run\ 2}}$	560	−26	26
$N_{K\pi\pi\pi,\mathrm{LL,Run\ 1}}$	101	−9	10
$N_{K\pi\pi\pi,\mathrm{LL,Run\ 2}}$	251	−16	16
$\mu_{\text{two-body}}$	5279.4	−0.3	0.3
$\mu_{\text{four-body}}$	5279.5	−0.5	0.5
$\sigma_{\text{two-body}}$	12.1	−0.3	0.3
$\sigma_{\text{four-body}}$	12.6	−0.4	0.4
$\beta_{\text{two-body,DD}}$	−0.0008	−0.0006	0.0006
$\beta_{\text{two-body,LL}}$	0.0002	−0.0011	0.0012
$\beta_{\text{four-body,DD}}$	−0.0014	−0.0006	0.0006
$\beta_{\text{four-body,LL}}$	−0.0003	−0.0014	0.0015

Table 5.9: Fitted values of the signal yields and shape parameters from the *CP* fit, where μ is the mean of the signal peak, σ is the width of the signal peak and β is the slope of the combinatorial background.

Decay mode	Total signal yield
$B^- \to D(K^-\pi^+)K^{*-}$	2030 ± 49
$B^- \to D(K^-K^+)K^{*-}$	257 ± 18
$B^- \to D(\pi^-\pi^+)K^{*-}$	80 ± 11
$B^- \to D(\pi^-K^+)K^{*-}$	20 ± 7
$B^- \to D(K^-\pi^+\pi^-\pi^+)K^{*-}$	1144 ± 37
$B^- \to D(\pi^-\pi^+\pi^-\pi^+)K^{*-}$	115 ± 13
$B^- \to D(K^+\pi^-\pi^+\pi^-)K^{*-}$	13 ± 7

Table 5.10: Total fitted yields in each of the D^0 decay modes extracted from the simultaneous fit performed with B^- and B^+ charges combined.

well as the information available.

The first method (Method 1) involves determining the systematic uncertainty in data, whereby some input of the model is adjusted. Sources of systematic uncertainty calculated via this method are those that arise from the use of fixed inputs in the *CP* fit. This method aims to quantify the amount by which the *CP* observables are affected by changes to these inputs on the scale of their associated uncertainty. The value of the input is drawn from a Gaussian distribution that has a mean corresponding to the central value of the input, as used in the nominal fit, and a width corresponding to the uncertainty in that value. In cases where parameters are varied simultaneously, any correlations between the parameters are ignored. Each

Mode	Branching ratio
$\mathcal{B}(D^0 \to K^-\pi^+)$	0.0393 ± 0.0004
$\mathcal{B}(D^0 \to K^+K^-)$	0.00401 ± 0.00007
$\mathcal{B}(D^0 \to \pi^+\pi^-)$	0.001421 ± 0.000025
$\mathcal{B}(D^0 \to K^-\pi^+\pi^-\pi^+)$	0.0811 ± 0.0015
$\mathcal{B}(D^0 \to \pi^+\pi^-\pi^+\pi^-)$	0.00745 ± 0.00020

Table 5.11: Branching ratios for the different D^0 decay modes, which are used as fixed inputs in the *CP* fit [10].

time the *CP* fit is performed, a value for each of the fitted parameters is extracted, resulting in a distribution for each *CP* observable. The standard deviation of each of these distributions is taken to be the systematic uncertainty for that *CP* observable.

The second method (Method 2) involves estimating the systematic uncertainty using pseudo-experiments, as described in Sec. 5.2.4. For each systematic effect being investigated, the generated model is varied to account for the corresponding model assumption. The systematic uncertainty on each observable is taken to be the difference between the mean of the fitted parameter distribution from the pseudo-experiments and the generated value. Sources of systematic uncertainty calculated via this method are those where Method 1 cannot be used.

Each source of systematic uncertainty, from both fixed inputs and model components, is described individually below. A summary of the systematic uncertainties for the *CP* observables is given in Table 5.13.

Branching ratios

The branching ratios for the different D^0 decays enter into the *CP* fit as in Eqs. 5.3 and 5.4. Table 5.11 gives the values of the branching ratios, which are fixed inputs in the *CP* fit, along with their uncertainties. The systematic uncertainty due to using branching ratios is calculated using Method 1, where the uncertainties in the branching ratios are used as the scale of the variation in the corresponding input.

Selection, PID and veto efficiencies

Selection, BDT, PID and veto efficiencies enter into the *CP* fit as in Eqs. 5.3, 5.4, 5.5 and 5.6. The values used in the *CP* fit are shown in Tables 5.4, 5.5, 5.6 and

5.7 along with their uncertainties. The systematic uncertainties, due to using the efficiencies as fixed values in the *CP* fit, are calculated separately for selection, PID and veto efficiencies using Method 1, where the uncertainties in the efficiencies are used as the scale of the variation.

Asymmetry corrections

Corrections must be made in the *CP* fit for production asymmetry and detection asymmetry as detailed in Sec. 5.2.1. For each source of asymmetry, a correction is applied in the *CP* fit and a systematic uncertainty is assigned separately to each based on the uncertainty of each correction using Method 1.

For the production asymmetry, a Run 1 value of the asymmetry is extracted using measurements performed with $B^+ \to \overline{D}^0\pi^+$ decays [71] in data. The equivalent results for Run 2 are not currently available, therefore the production asymmetry for Run 2 is taken to have the same central value as for Run 1 with twice the uncertainty. This is considered sufficient to cover any unknown difference due to the increased centre-of-mass energy. For the detection asymmetry, the corrections are obtained using Run 1 data and again the same results are used for Run 2 data. The changes to the detector between the data-taking periods are not expected to significantly affect the detection asymmetry characteristics, hence the uncertainty is not increased in this case. For each asymmetry correction, the uncertainties are used as the scale of the variation for calculating the systematic uncertainty.

Signal shape

The signal shape, described in Sec. 4.2.2, is modelled as a Double Crystal Ball with all parameters fixed from simulation apart from the peak position and a width. There are two sources of uncertainty in the choice of signal shape: the tail parameters, α and n, and the width ratio and yield fraction between the two CBs, f_σ and f_{cb} respectively. These two sources of uncertainty are treated separately and then combined.

The uncertainty in the tail parameters is quantified using Method 2 by using an alternative signal shape, formed from the sum of two Gaussian-like distributions

with a common mean, different widths, and two additional parameters relating to the skewness and sharpness of the distribution [74]. This shape is taken to have the same width ratio and yield fraction as the Double Crystal Ball used in the *CP* fit. The two additional parameters are fixed from a maximum likelihood fit to the simulated signal sample, shown in Fig. 5.7. Data are generated with this alternative shape, and the *CP* fit is then repeated using the nominal fit model. The systematic uncertainties associated with this method are given in the first row of Table 5.12.

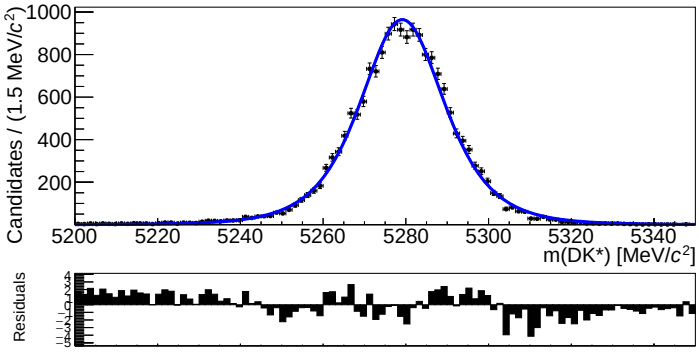

Figure 5.7: Maximum likelihood fit performed on a simulated signal sample of DD candidates using the alternative shape described in the text [74].

For the width ratio and yield fraction, a systematic uncertainty is assigned using Method 1, where the scale of the variation in the inputs used is the uncertainty in these values, as given in Table 4.8. The results from this method are given in the second row of Table 5.12.

The systematic uncertainties from generating an alternative distribution and from variation of the Double Crystal Ball parameters are added in quadrature to give the total signal shape systematic uncertainty. The systematic uncertainty associated with the use of the alternative shape dominates the signal shape uncertainty for most of the *CP* observables.

Combinatorial background

The shape parameter of the combinatorial background, β, defined in Sec. 4.2.3, is fixed across all D^0 modes in the *CP* fit; there are not enough data for the fit to be stable if the shape is allowed to vary in each mode. In order to ascertain the

	$A_{K\pi}$	A_{KK}	$A_{\pi\pi}$	R_{KK}	$R_{\pi\pi}$	$R^+_{K\pi}$	$R^-_{K\pi}$
Alternative shape	1.1×10^{-3}	2.9×10^{-3}	1.1×10^{-2}	3.0×10^{-3}	2.6×10^{-2}	1.0×10^{-3}	1.3×10^{-3}
Vary parameters	2.3×10^{-4}	1.1×10^{-3}	1.4×10^{-3}	5.9×10^{-4}	4.4×10^{-3}	2.2×10^{-4}	1.1×10^{-4}
Total	1.1×10^{-3}	3.1×10^{-3}	1.1×10^{-2}	3.0×10^{-3}	2.7×10^{-2}	1.1×10^{-3}	1.3×10^{-3}

	$A_{K\pi\pi\pi}$	$A_{\pi\pi\pi\pi}$	$R_{\pi\pi\pi\pi}$	$R^+_{K3\pi}$	$R^-_{K3\pi}$
Alternative shape	1.6×10^{-3}	1.3×10^{-3}	9.8×10^{-3}	3.0×10^{-3}	3.8×10^{-3}
Vary parameters	4.7×10^{-4}	1.8×10^{-3}	2.5×10^{-3}	2.4×10^{-4}	1.2×10^{-4}
Total	1.7×10^{-3}	2.2×10^{-3}	1.0×10^{-2}	3.0×10^{-3}	3.8×10^{-3}

Table 5.12: Summary of systematic uncertainties associated with the signal shape.

variation in combinatorial shape between different D^0 modes, individual maximum likelihood fits are performed to each D^0 decay mode in the high B^- mass region (5400 - 5600 MeV/c^2) using an exponential function. The selection requirements are loosened as described below in order to retain enough data to perform a meaningful fit. Run 1 data are used for the fits with the selection applied, except for the K^{*-} selection and D^0 and K^0_S FD significance cuts. PID selection of the D^0 daughters is applied in order to be sure of accessing the difference between the corresponding D^0 modes. The systematic uncertainty is assigned using Method 2, with β for each D^0 mode fixed to these values given in Fig. 5.8, where the fits to the DD candidates are shown. Separate fits were also performed for LL candidates.

Partially reconstructed background

The partially reconstructed decays have a fixed shape and yield in the *CP* fit, as discussed in Sec. 5.1.2. Method 2 is used to assign a systematic uncertainty, by making three simultaneous modifications to the partially reconstructed region. These are:

- The yield is increased by 20%. The uncertainty in the yield from the fit to the $B^- \to D(K^-\pi^+)K^{*-}$ invariant mass is about 5%. However this is considered to be an underestimate as other partially reconstructed low mass backgrounds, such as $B^- \to DK^{*-}\pi^0$, may contribute a small amount at low reconstructed B^- mass, outside of the *CP* fit range. This may affect the estimate for the yield of partially reconstructed background, therefore a conservative systematic uncertainty of 20% is used.

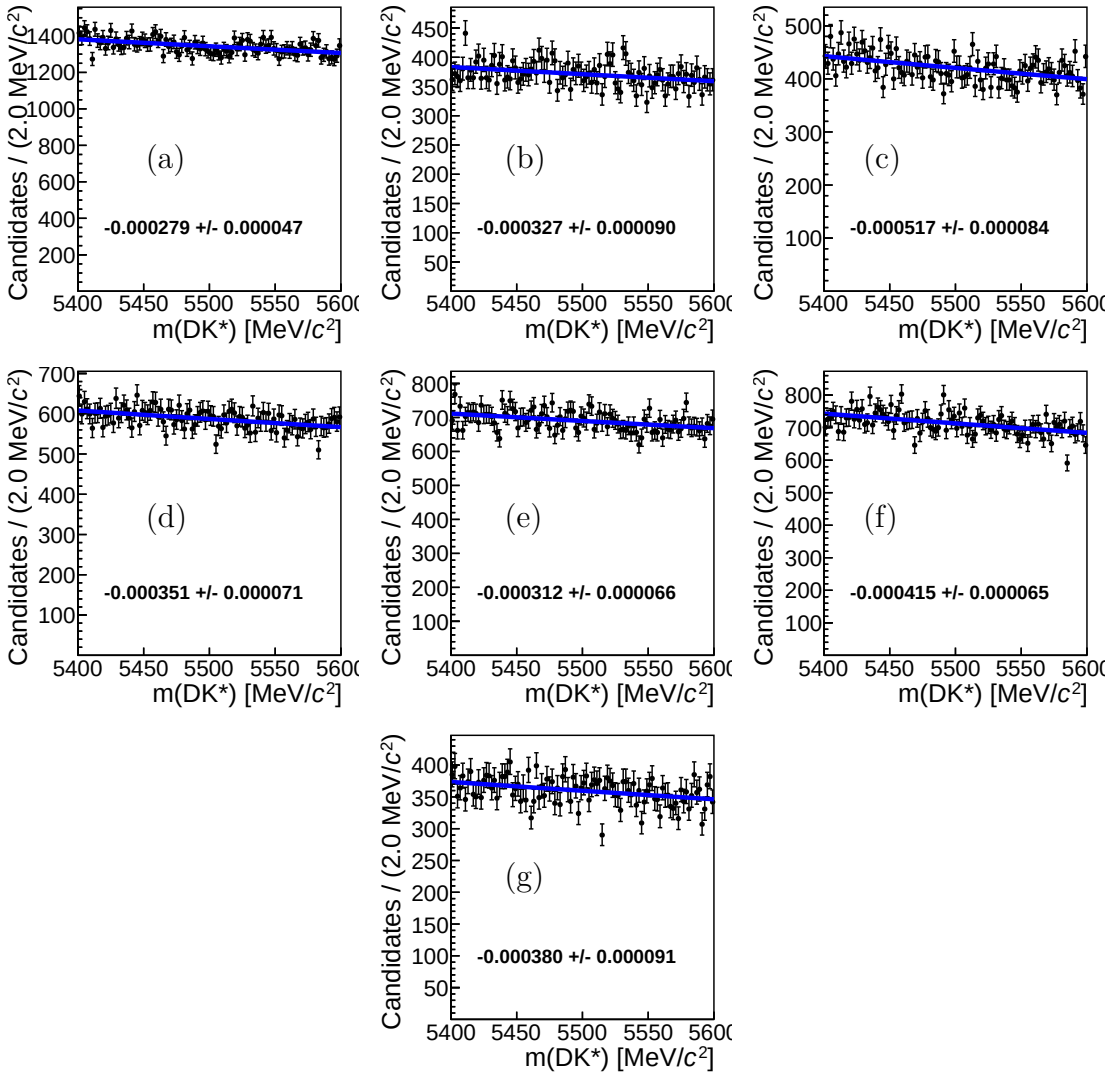

Figure 5.8: Maximum likelihood fits to the combinatorial background in the high B^- mass region for DD candidates for the D^0 decay to (a) $K^-\pi^+$, (b) K^-K^+, (c) $\pi^-\pi^+$, (d) π^-K^+, (e) $K^-\pi^+\pi^-\pi^+$, (f) $\pi^-\pi^+\pi^-\pi^+$, and (g) $\pi^-K^+\pi^-\pi^+$. The fitted values for the exponential slope parameter, β, are given on each plot in units MeV/c^{2-1}.

- All partially reconstructed shapes are smeared by the difference in signal width between simulated samples and data. The widths for all partially reconstructed shapes are increased by 4% for LL bins and 5% for DD bins.

- A 10% asymmetry is introduced to take into account possible *CP* violation in the partially reconstructed yields.

Charmless contribution

Section 4.1.3 shows that there is a possibility for a residual charmless contribution to be present in the $B^- \to D(\pi^-\pi^+)K^{*-}$ mode. In order to estimate the associated systematic uncertainty, Method 2 is used. Here the yield of charmless events to be generated in $B^- \to D(\pi^-\pi^+)K^{*-}$ is drawn from a Gaussian distribution that has mean and width corresponding to the expected number of charmless events and its uncertainty, calculated in Sec. 4.1.3. The number of events is O(1) in each of the bins. For each pseudo-experiment, the value taken from the Gaussian distribution is rounded to a whole number and randomly distributed between B^+ and B^-, as an additional contribution to the yield in the signal region.

$\Lambda_b^0 \to \Lambda_c^+(pK\pi)K^{*-}$ background

The model for the $B^- \to D(K^-K^+)K^{*-}$ mass spectrum in the *CP* fit contains an additional background from $\Lambda_b^0 \to \Lambda_c^+(pK^-\pi^+)K^{*-}$ decays, as described in Sec. 4.1.3. The shape parameters are fixed from a maximum likelihood fit to a simulated sample of $\Lambda_b^0 \to \Lambda_c^+(pK^-\pi^+)K^-$ decays, the values of which are given in Table 5.2. The systematic uncertainty corresponding to this model component is estimated using Method 2, by varying the parameters of the model according to the uncertainties in Table 5.2.

$B_s^0 \to \overline{D}^0\bar{K}^*(1410)^0$ background

The decay $B_s^0 \to \overline{D}^0\bar{K}^*(1410)^0$ is a background for the $B^- \to D(\pi^-K^+)K^{*-}$ mode, as described in Sec. 4.1.3. The shape is taken from a maximum likelihood fit to simulated events and the fractional yield compared to the $B^- \to D(\pi^-K^+)K^{*-}$ signal yield is taken to be $(1.28 \pm 1.26) \times 10^{-3}$. The systematic uncertainty corresponding to this model component is estimated using Method 2, where the generated fractional yield is drawn from a Gaussian distribution with a mean of 1.28×10^{-3} and a width of 1.26×10^{-3}.

5.4.2 Summary of systematic uncertainties

Table 5.13 summarises the systematic uncertainties for each of the different sources discussed in this section. If the systematic uncertainty is found to be over two orders of magnitude smaller than the statistical uncertainty then a value of zero is given. It can be seen that all systematic uncertainties are smaller than the corresponding statistical uncertainty. The systematic uncertainty due to the signal shape contributes to the uncertainty for all *CP* observables, and for some it is the dominant contribution. Leading systematic uncertainties in the yield ratios come from simulation efficiencies and branching ratios. These are external measurements, whose uncertainties could be reduced by further work.

5.5 Summary of results

The final results for the *CP* observables are

$$
\begin{aligned}
A_{K\pi} &= -0.004 \pm 0.023 \pm 0.008 \\
A_{KK} &= 0.06 \pm 0.07 \pm 0.01 \\
A_{\pi\pi} &= 0.15 \pm 0.13 \pm 0.01 \\
R_{KK} &= 1.22 \pm 0.09 \pm 0.02 \\
R_{\pi\pi} &= 1.08 \pm 0.14 \pm 0.03 \\
R^{+}_{K\pi} &= 0.020 \pm 0.006 \pm 0.001 \\
R^{-}_{K\pi} &= 0.002 \pm 0.004 \pm 0.001 \\
A_{K\pi\pi\pi} &= -0.013 \pm 0.031 \pm 0.009 \\
A_{\pi\pi\pi\pi} &= 0.02 \pm 0.11 \pm 0.01 \\
R_{\pi\pi\pi\pi} &= 1.08 \pm 0.13 \pm 0.03 \\
R^{+}_{K\pi\pi\pi} &= 0.016 \pm 0.007 \pm 0.003 \\
R^{-}_{K\pi\pi\pi} &= 0.006 \pm 0.006 \pm 0.004
\end{aligned}
$$

where the first uncertainty is statistical and the second is systematic. The correlation matrices for the statistical and systematic uncertainties are given in Tables 5.14

	$A_{K\pi}$	A_{KK}	$A_{\pi\pi}$	R_{KK}	$R_{\pi\pi}$	$R^+_{K\pi}$	$R^-_{K\pi}$	$A_{K\pi\pi\pi}$	$A_{\pi\pi\pi\pi}$	$R_{\pi\pi\pi\pi}$	$R^+_{K\pi\pi\pi}$	$R^-_{K\pi\pi\pi}$
Statistical uncertainty	0.023	0.07	0.13	0.09	0.15	0.006	0.004	0.031	0.11	0.13	0.008	0.007
Branching fractions	–	–	0.001	0.013	0.012	–	–	–	0.0008	0.027	–	–
Selection efficiencies	–	–	–	0.007	0.006	0.0002	–	–	0.0008	0.014	–	–
PID efficiencies	–	–	–	0.002	0.002	–	–	–	–	0.002	–	–
Veto efficiencies	–	–	–	–	–	0.0001	–	–	–	–	–	–
A_{prod}	0.0073	0.007	0.008	–	–	–	–	0.0079	0.0077	–	–	–
A_{det}	0.0034	0.003	0.003	–	–	0.0001	–	0.0034	0.0030	–	0.0001	–
Signal shape	0.0011	0.003	0.003	0.011	0.027	0.0011	0.0013	0.0017	0.0022	0.010	0.0030	0.0038
Combinatorial shape	0.0012	0.003	0.005	0.004	0.009	0.0002	0.0003	0.0001	0.0018	–	0.0012	0.0004
Partially reconstructed shape	0.0007	0.001	0.003	0.001	0.005	–	0.0003	0.0003	0.0005	0.002	0.0008	0.0001
Charmless	0.0008	–	0.003	0.002	0.007	–	0.0003	0.0009	0.0030	0.002	0.0008	0.0001
$\Lambda^0_b \to \Lambda^+_c K^{*-}$	0.0002	–	–	0.011	0.001	0.0001	–	–	–	–	–	–
$B^0_s \to DK^*(1410)^0$	–	–	–	–	–	0.0005	0.0001	–	–	–	–	–
Total systematic uncertainty	0.0083	0.009	0.012	0.022	0.032	0.0012	0.0014	0.0088	0.0093	0.032	0.0034	0.0038

Table 5.13: Summary of systematic uncertainties on the fitted *CP* observables. The total systematic uncertainty for each *CP* observable is calculated by summing each component in quadrature. Uncertainties are not shown if they are more than two orders of magnitude smaller than the statistical uncertainty.

and 5.15, respectively. For the systematic uncertainties, the correlation matrices are calculated separately for each contribution to the systematic uncertainty, listed in Sec. 5.4, then these correlation matrices are combined. The large correlations of the systematic uncertainties are mainly due to the contributions from production and detection asymmetries. Combined results of the *CP* observables from the *CP*-even $B^- \to D(K^-K^+)K^{*-}$ and $B^- \to D(\pi^-\pi^+)K^{*-}$ decay modes, taking correlations into account, are

$$A_{CP+} = 0.08 \pm 0.06 \pm 0.01,$$
$$R_{CP+} = 1.18 \pm 0.08 \pm 0.02,$$

where the first uncertainty is statistical and the second is systematic. The parameters A_{CP+} and R_{CP+} are defined in Eqs. 2.41 and 2.42 respectively. It can be seen that the asymmetry in the GLW modes, A_{CP+}, is not statistically significant.

The *CP* observables R^+_m and R^-_m, where m represents $K\pi$ or $K\pi\pi\pi$, can be transformed into $R^m_{ADS} = (R^-_m + R^+_m)/2$ and $A^m_{ADS} = (R^-_m - R^+_m)/(R^-_m + R^+_m)$ in order to compare with the results from BaBar [44]. The results from the analysis presented in this thesis, taking correlations into account, are

$$\begin{aligned} A^{K\pi}_{ADS} &= -0.81 \pm 0.17 \pm 0.04 \\ R^{K\pi}_{ADS} &= 0.011 \pm 0.004 \pm 0.001 \\ A^{K\pi\pi\pi}_{ADS} &= -0.45 \pm 0.21 \pm 0.14 \\ R^{K\pi\pi\pi}_{ADS} &= 0.011 \pm 0.005 \pm 0.003\ , \end{aligned}$$

where the first uncertainty is statistical and the second is systematic. These uncertainties a factor of 3 to 5 larger than those obtained from the equivalent modes in the $B^- \to DK^-$ channel [16]. The measured asymmetries and ratios for the two-body D^0 meson decay modes are consistent with, and more precise than, the previous measurements from BaBar [44], which are

$$\begin{aligned} A^{K\pi}_{ADS} &= -0.34 \pm 0.43 \pm 0.16 \\ R^{K\pi}_{ADS} &= 0.066 \pm 0.031 \pm 0.010\ , \end{aligned}$$

where the first uncertainty is statistical and the second is systematic.

The Wilks' theorem statistical significance [75] for the two-body and four-body ADS decay modes, is defined as:

$$\sqrt{-2ln\left(\frac{L_0}{L_i}\right)} \tag{5.19}$$

where L_0 is the extended maximum likelihood value for the nominal *CP* fit model and L_i is the extended maximum likelihood value for the alternative model, which forces $R^{K\pi}_{ADS} = 0$ or $R^{K\pi\pi\pi}_{ADS} = 0$ respectively. Therefore, the more unlikely that the alternative model is correct, given the data, the higher the statistical significance. It is worth noting that this calculation does not account for systematic uncertainties. The signal significance for the four-body ADS decay mode is calculated to be 2.8σ, while for the two-body ADS decay mode it is calculated to be 4.2σ, showing the first evidence for $B^- \to D(\pi^-K^+)K^{*-}$ decays.

	$A_{K\pi}$	A_{KK}	$A_{\pi\pi}$	R_{KK}	$R_{\pi\pi}$	$R^+_{K\pi}$	$R^-_{K\pi}$	$A_{K\pi\pi\pi}$	$A_{\pi\pi\pi\pi}$	$R_{\pi\pi\pi\pi}$	$R^+_{K\pi\pi\pi}$	$R^-_{K\pi\pi\pi}$
$A_{K\pi}$	1	–	–	–	–	0.08	−0.01	–	–	–	–	–
A_{KK}		1	–	–	–	–	–	–	–	–	–	–
$A_{\pi\pi}$			1	–	−0.02	–	–	–	–	–	–	–
R_{KK}				1	0.05	0.02	−0.01	–	–	–	–	–
$R_{\pi\pi}$					1	0.03	0.02	–	–	–	–	–
$R^+_{K\pi}$						1	0.02	–	–	–	–	–
$R^-_{K\pi}$							1	–	–	–	–	–
$A_{K\pi\pi\pi}$								1	–	–	0.07	−0.03
$A_{\pi\pi\pi\pi}$									1	0.01	–	–
$R_{\pi\pi\pi\pi}$										1	0.04	0.04
$R^+_{K\pi\pi\pi}$											1	0.03
$R^-_{K\pi\pi\pi}$												1

Table 5.14: Correlation matrix of the statistical uncertainties for the twelve physics observables from the simultaneous fit to data. Only half of the symmetric matrix is shown.

	$A_{K\pi}$	A_{KK}	$A_{\pi\pi}$	R_{KK}	$R_{\pi\pi}$	$R^+_{K\pi}$	$R^-_{K\pi}$	$A_{K\pi\pi\pi}$	$A_{\pi\pi\pi\pi}$	$R_{\pi\pi\pi\pi}$	$R^+_{K\pi\pi\pi}$	$R^-_{K\pi\pi\pi}$
$A_{K\pi}$	1	0.82	0.72	–	–	0.01	−0.02	0.94	0.84	–	−0.01	–
A_{KK}		1	0.65	−0.04	0.02	0.01	−0.02	0.83	0.77	–	–	–
$A_{\pi\pi}$			1	–	−0.03	–	−0.02	0.72	0.68	–	–	0.01
R_{KK}				1	–	0.05	0.03	−0.01	–	−0.01	−0.01	−0.01
$R_{\pi\pi}$					1	0.06	0.08	−0.01	–	−0.01	−0.02	0.01
$R^+_{K\pi}$						1	0.08	−0.01	–	–	−0.01	−0.01
$R^-_{K\pi}$							1	−0.01	−0.01	−0.01	0.01	0.03
$A_{K\pi\pi\pi}$								1	0.84	–	−0.01	−0.02
$A_{\pi\pi\pi\pi}$									1	0.03	0.01	–
$R_{\pi\pi\pi\pi}$										1	0.01	−0.01
$R^+_{K\pi\pi\pi}$											1	0.05
$R^-_{K\pi\pi\pi}$												1

Table 5.15: Correlation matrix of the systematic uncertainties for the twelve physics observables from the simultaneous fit to data. Only half of the symmetric matrix is shown.

6

Extraction of CKM angle γ and future prospects

The *CP* observables from $B^- \to DK^{*-}$ decays are used to determine the physics parameters, r_B, δ_B and γ, via Eqs. 2.41 - 2.46. In this determination, the other parameters that appear in Eqs. 2.41 - 2.46, namely $r_D^{K\pi}$, $\delta_D^{K\pi}$, $r_D^{K3\pi}$, $\delta_D^{K3\pi}$, $R_{K3\pi}$ and $F_{4\pi}$, are taken directly from other measurements to be used as external inputs [24, 28–30]. The coherence factor κ, discussed in Sec. 2.5, is estimated, as described in Sec. 6.1, and used as an extra constraint when determining r_B, δ_B and γ. The variations in acceptance across the four-body phase space and the effect of this on the interpretation of results are considered in Sec. 6.2. Section 6.3 discusses the determination of r_B, δ_B and γ from the measurements of $B^- \to DK^{*-}$ decays. Finally, Sec. 6.4 discusses the expected sensitivity of the $B^- \to DK^{*-}$ channel to r_B, δ_B and γ with an increased dataset, after further running periods of the LHC.

6.1 The coherence factor, κ

As discussed in Sec. 2.5, due to the large natural width of the K^{*-} meson in the region near the K^{*-} mass, interference may occur between the signal K^{*-} decay amplitude and amplitudes due to other $B^- \to DK^0_S\pi^-$ contributions, for example higher $K^0_S\pi^-$ resonances and non-resonant decays. The presence of these interfering

contributions when analysing the $B^- \to DK^{*-}$ decays dilutes the sensitivity to γ. This is quantified by the coherence factor, κ, and $0 \leq \kappa \leq 1$, where $\kappa = 1$ denotes a pure K^{*-} contribution, which gives maximum sensitivity to γ.

6.1.1 The decay model

There are no amplitude studies of $B^- \to DK^0_S\pi^-$ decays in data to date. Hence, the coherence factor κ is estimated by developing an amplitude model for $B^- \to DX^-$ decays, where X^- represents either a resonant or non-resonant $K^0_S\pi^-$ pair. The components of the model used for this study are:

- $B^+ \to D^0K^*(892)^+$ and $B^+ \to \overline{D}^0K^*(892)^+$
- $B^+ \to D^0K^*_0(1430)^+$ and $B^+ \to \overline{D}^0K^*_0(1430)^+$.

Other resonances, e.g. $K^*(1680)^+$ and $D^*_2(2460)^-$, are considered to be negligible in the region of phase space near the $K^*(892)^+$ and so are not included in the model, as they will not affect the κ calculation. The $K^*(892)^+$ line-shape uses a relativistic Breit-Wigner component. The line-shape for the $K^*_0(1430)^+$ uses a parameterisation developed by the LASS experiment [76], which approximately consists of a relativistic Breit-Wigner component [77] corresponding to the resonant $K^*_0(1430)^+$, and a non-resonant scattering component. The parameters of the resonances are listed in Table 6.1.

Resonance	Mass, M MeV/c^2	Width, Γ MeV/c^2	Spin
$K^*(892)^+$	891.66 ± 0.26	50.8 ± 0.9	1
$K^*_0(1430)^+$	1425 ± 50	270 ± 80	0

Table 6.1: Parameters of the resonances in the decay model of $B^- \to DX^-$ decays [10].

In order to calculate κ, it is necessary to consider the magnitudes and phases of the model components described. The parameters A_{ub} describing $b \to u$ transitions, and A_{cb} describing $b \to c$ transitions, are the total amplitudes of the suppressed

and favoured $B^- \to DX^-$ decays respectively. The amplitudes A_{ub} and A_{cb} are modelled as:

$$\begin{aligned} A_{ub} = & a_{ub}^{K^*(892)^+} e^{-i\delta_{ub}^{K^*(892)^+}} RelBW(p; M_{K^*(892)^+}, \Gamma_{K^*(892)^+}, 1) + \\ & a_{ub}^{K_0^*(1430)^+} e^{-i\delta_{ub}^{K_0^*(1430)^+}} LASS\_BW(p; M_{K_0^*(1430)^+}, \Gamma_{K_0^*(1430)^+}, 0) + \\ & a_{ub}^{NR} e^{-i\delta_{ub}^{NR}} LASS\_NR \end{aligned}$$

and

$$\begin{aligned} A_{cb} = & a_{cb}^{K^*(892)^+} e^{-i\delta_{cb}^{K^*(892)^+}} RelBW(p; M_{K^*(892)^+}, \Gamma_{K^*(892)^+}, 1) + \\ & a_{cb}^{K_0^*(1430)^+} e^{-i\delta_{cb}^{K_0^*(1430)^+}} LASS\_BW(p; M_{K_0^*(1430)^+}, \Gamma_{K_0^*(1430)^+}, 0) + \\ & a_{cb}^{NR} e^{-i\delta_{cb}^{NR}} LASS\_NR \ , \end{aligned}$$

where $RelBW$, $LASS\_BW$ and $LASS\_NR$ refer to the relativistic Breit-Wigner, LASS Breit-Wigner and LASS non-resonance shapes respectively [76]. A given resonance denoted by $R(p; M, \Gamma, J)$ has a mass M, width Γ, and spin J, where p corresponds to the kinematic location in $B^- \to DK_S^0\pi^-$ phase space. The parameters a_{ij}^k are the respective amplitudes and δ_{ij}^k the strong phase differences.

The ratio of the squares of the magnitude of the various components is equal to the relative branching fractions in the limit of no interference. When estimating the magnitudes of the components, the scenario of no interference is assumed. The only available branching fraction measurement [10] is:

$$\mathcal{B}(B^+ \to \overline{D}^0 K^*(892)^+) \times \mathcal{B}(K^*(892)^+ \to K_S^0\pi^+) = 1.8 \times 10^{-4} \ .$$

It is assumed that the different resonant K^{*+} modes are produced with the same branching fraction as the $K^*(892)^+$ mode, e.g. $\mathcal{B}(B^+ \to \overline{D}^0 K^*(892)^+) = \mathcal{B}(B^+ \to \overline{D}^0 K^*(1430)^+)$. The branching fractions of different resonant K^{*+} modes to the $K_S^0\pi^+$ final state are also taken into account, namely $\mathcal{B}(K^*(892)^+ \to K_S^0\pi^+) = \frac{1}{3}$ and $\mathcal{B}(K_0^*(1430)^+ \to K_S^0\pi^+) = 0.31$ [10].

The branching fraction of the non-resonant decay $\mathcal{B}$ $(B^+ \to \overline{D}^0 K_S^0\pi^+)$ is not known. Therefore, assuming

$$\frac{\mathcal{B}(B^0 \to D^- K^0\pi^+)}{\mathcal{B}(B^0 \to D^- \overline{K}^0 K^+)} = \frac{\mathcal{B}(B^+ \to \overline{D}^0 K^0\pi^+)}{\mathcal{B}(B^+ \to \overline{D}^0 \overline{K}^0 K^+)} \ ,$$

and using measurements and upper limits for the other branching fractions [10], the value of $\mathcal{B}\,(B^+ \to \overline{D}^0 K^0_{\rm S}\pi^+)$ is estimated to have an upper limit of $(5.2 \pm 0.3) \times 10^{-4}$, which is used in the model.

When generating an amplitude model, only the *relative* amplitudes and phases of the various components are required; therefore the $K^*(892)^+$ is fixed to have an amplitude of 1 and phase of 0. The relative amplitude r_B is assumed to be 0.1. Using the estimates for the various branching ratios, the values of the squares of the amplitudes a_{ub} and a_{cb} of the model components are estimated from the ratio of these branching fractions relative to the $B^- \to DK^*(892)^+(K^0_{\rm S}\pi^+)$ decay,

$$|a_{cb}^{NR}|^2 = \frac{\mathcal{B}(B^+ \to \overline{D}^0 K^0_{\rm S}\pi^+)}{\mathcal{B}(B^- \to DK^*(892)^+(K^0_{\rm S}\pi^+))} = \frac{5.2 \times 10^{-4}}{1.8 \times 10^{-4}} = 2.4\ ,$$
$$|a_{cb}^{K_0^*(1430)^+}|^2 = \frac{\mathcal{B}(B^- \to DK_0^*(1430)^+(K^0_{\rm S}\pi^+))}{\mathcal{B}(B^- \to DK^*(892)^+(K^0_{\rm S}\pi^+))} = \frac{1/3 \times 5.4 \times 10^{-4}}{0.31 \times 5.4 \times 10^{-4}} = 0.93\ .$$

For the non-resonant component the branching fraction estimate is an upper limit, whilst for the $K_0^*(1430)^+$ component a conservative range of 60% of the above estimates is assumed. Therefore the squares of the amplitudes a_{ub} and a_{cb} are taken in the ranges:

- $|a_{cb}^{K^*(892)^+}|^2 = 1, \quad$ with $a_{ub}^{K^*(892)^+} = r_B a_{cb}^{K^*(892)^+}$
- $|a_{cb}^{K_0^*(1430)^+}|^2 \in [0.7 \times 0.93, 1.3 \times 0.93], \quad$ with $a_{ub}^{K_0^*(1430)^+} = r_B a_{cb}^{K_0^*(1430)^+}$
- $|a_{cb}^{NR}|^2 \in [0.0, 2.4], \quad$ with $a_{ub}^{NR} = r_B a_{cb}^{NR}$.

Figure 6.1 shows an example of the amplitude model described. The K^* selection requirements of this analysis in K^* mass and $K^0_{\rm S}$ helicity angle are represented by dashed lines in this plot.

6.1.2 Estimation of the coherence factor, κ

One thousand variants of the amplitude model, described in Sec. 6.1.1, are generated, which differ in the amplitudes and phases of the components. For different variants of the amplitude model, the amplitudes and phases of the different resonances are varied randomly within limits; the limits for the amplitudes are given in Sec. 6.1.1

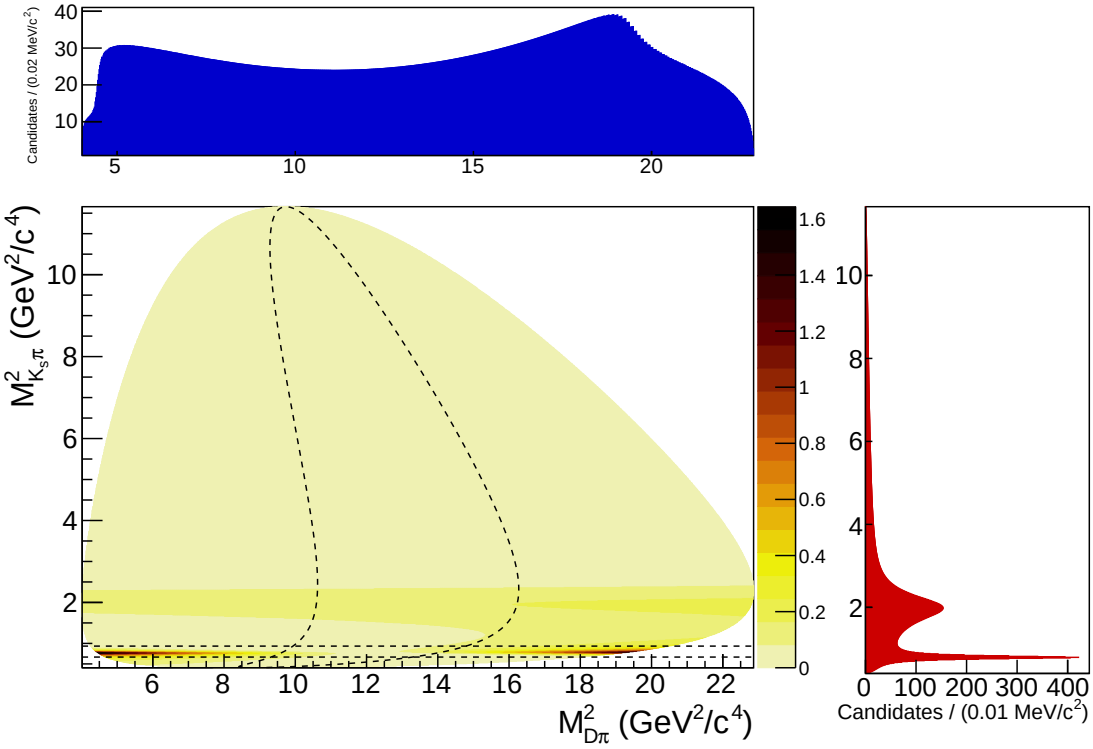

Figure 6.1: An example amplitude model used in the estimate of κ. The horizontal axis labelled $M^2_{D\pi}$ is defined as $(p_D + p_\pi)^2$, where p_X is the four-momentum of particle X. Similarly, the vertical axis, labelled $M^2_{K_s\pi}$, is defined as $(p_{K_s} + p_\pi)^2$. The projections in these two coordinates are shown. The $K^*(892)^+$ and $K^*(1430)^+$ resonances can be clearly seen in the red projection on the right hand side of the figure. The dashed lines on the plot represent the K^* mass and K^0_S helicity angle selection used in this analysis.

and all phases are generated randomly according to a uniform distribution between $-\pi$ and π. The masses and widths of the resonances are kept constant at their central values, given in Table 6.1.

For each model, κ is computed according to the magnitude of the expression in Eq. 2.24. This results in a distribution of κ values estimated by the model, shown in Fig. 6.2. The mean and standard deviation of the resulting distribution provides an estimate of the central value and uncertainty of κ, 0.95 ± 0.04. However, it is considered necessary to increase the uncertainty of this estimate in order to account for the skewness of the distribution, therefore a final value of $\kappa = 0.95 \pm 0.06$ is used in this thesis to extract the physics parameters of interest.

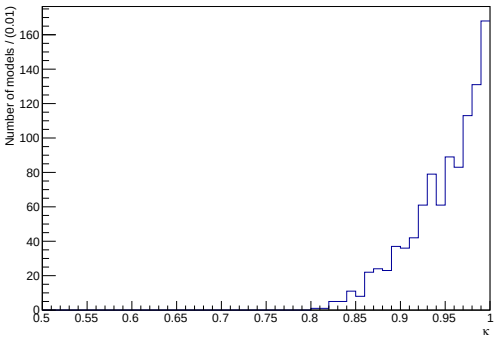

Figure 6.2: Distribution of the values of κ from 1000 samples generated according to the amplitude model described in the text.

6.2 Four-body phase space acceptance variations

For multibody $D^0 \to K^{\mp}\pi^{\pm}\pi^{\mp}\pi^{\pm}$ and $D^0 \to \pi^+\pi^-\pi^+\pi^-$ decays, some regions of phase space may exhibit larger *CP* violation than other regions. In this thesis, an inclusive analysis over phase space is performed. Therefore only the global *CP* violation is elicited, and it may result in a loss of information of regional variation. The parameters $R_{K3\pi}$, $\delta_D^{K3\pi}$ and $F_{4\pi}$ allow the phase space to be treated inclusively, so that global asymmetries can be interpreted in a manner similar to the two-body D^0 decays.

The parameter $F_{4\pi}$ has been measured using data from CLEO-c [24], while the values for $\delta_D^{K3\pi}$ and $R_{K3\pi}$ are taken from combining results from LHCb and CLEO-c data [29–31]. These measurements have been corrected for a uniform efficiency across all phase space. When making measurements at LHCb, the LHCb acceptance leads to small non-uniformities in efficiency, which could enhance or diminish asymmetry in certain regions of phase space. In order to use the measurements of $F_{4\pi}$, $\delta_D^{K3\pi}$ and $R_{K3\pi}$ in this analysis these effects must be assessed and accounted for. This can be achieved either by correcting for the LHCb yields under a scenario of uniform efficiency or by adjusting the $F_{4\pi}$, $\delta_D^{K3\pi}$ and $R_{K3\pi}$ parameters to match the LHCb efficiency variation. The efficiencies calculated in Sec. 5.2.2 assume an average efficiency across the phase space. In order to correct for the LHCb yields, event-wise efficiency corrections would have to be performed, which is not practical due to the large numbers of simulated events,

and the computing power required. Therefore, consideration is given to whether the parameters $F_{4\pi}$, $\delta_D^{K3\pi}$ and $R_{K3\pi}$ require adjustment.

Figures 6.3 and 6.4 show projections of the four-body phase space distributions for $B^- \to D(K^-\pi^+\pi^-\pi^+)K^{*-}$ and $B^- \to D(\pi^-\pi^+\pi^-\pi^+)K^{*-}$ modes respectively. These plots are comparisons of distributions using simulated generator-level signal events without any acceptance effects, and fully-reconstructed simulated signal events used in this analysis. It can be seen that the distributions are very similar, suggesting that any differences due to LHCb acceptance effects are very small. This implies that $R_{K3\pi}$, $\delta_D^{K3\pi}$ and $F_{4\pi}$ can be used directly in the interpretation of LHCb results.

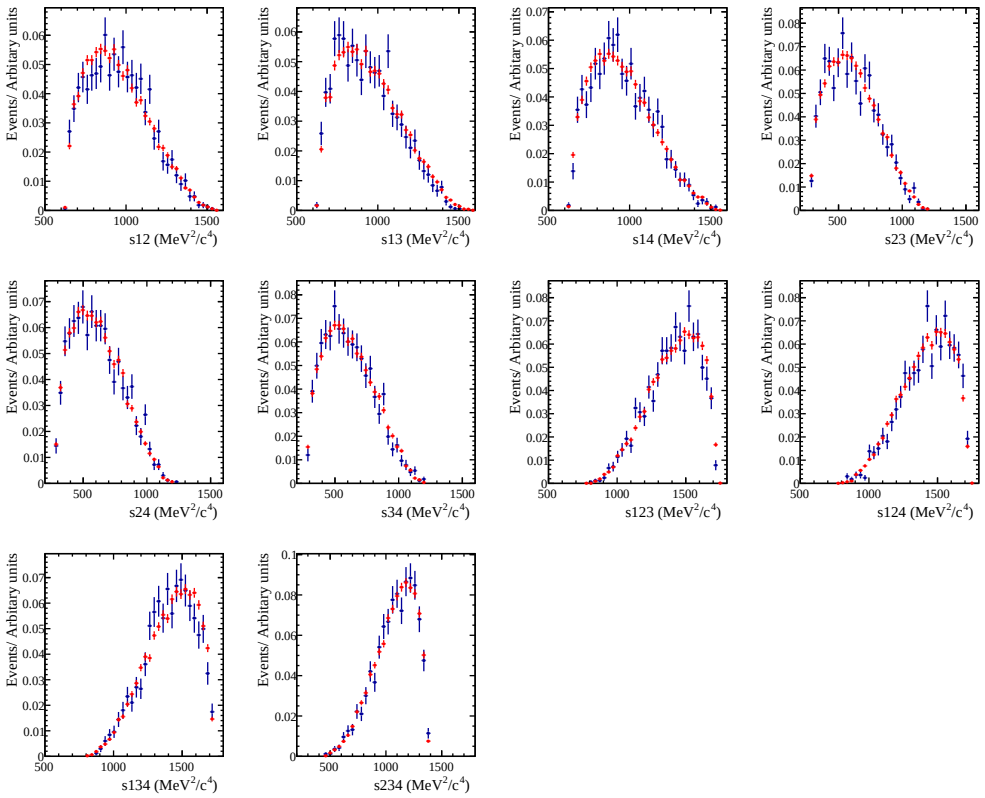

Figure 6.3: Distributions of invariant mass squared for all combinations of two- and three-particles from the four D^0 daughters with simulated generator level events (blue) and fully reconstructed and selected events (red) in the $B^- \to D(K^-\pi^+\pi^-\pi^+)K^{*-}$ mode. The variable sXY is defined as $(p_X + p_Y)^2$, where X and Y represent labels that refer to a specific daughter of the D^0 meson, and p_X is the four-momentum of particle X. The D^0 daughter labels are defined by: $B^- \to D(K_1^-\pi_2^+\pi_3^-\pi_4^+)K^{*-}$.

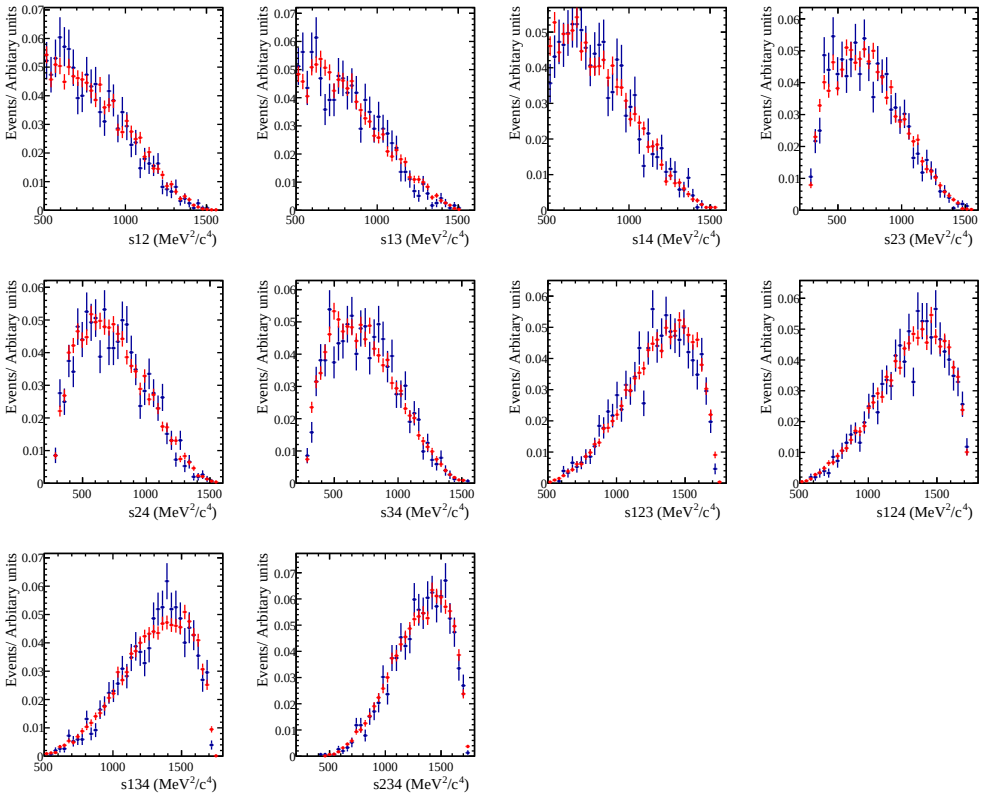

Figure 6.4: Distributions of invariant mass squared for all combinations of two- and three-particles from the four D^0 daughters with simulated generator level events (blue) and fully reconstructed and selected events (red) in the $B^- \to D(\pi^-\pi^+\pi^-\pi^+)K^{*-}$ mode. The variable sXY is defined as $(p_X + p_Y)^2$, where X and Y represent labels that refer to a specific daughter of the D^0 meson, and p_X is the four-momentum of particle X. The D^0 daughter labels are defined by: $B^- \to D(\pi_1^-\pi_2^+\pi_3^-\pi_4^+)K^{*-}$.

To verify the above implication, further studies are performed to assess whether the values of the parameters $R_{K3\pi}$ and $\delta_D^{K3\pi}$ require any corrections for the determination of the physics parameters. To assess the effects of any small variations in the four-body phase space for $B^- \to D(K^-\pi^+\pi^-\pi^+)K^{*-}$ decays, the coherence factor and strong phase are calculated from a preliminary version of the $D^0 \to K^-\pi^+\pi^-\pi^+$ amplitude model described in Ref. [78], both under the assumptions of uniform acceptance and including LHCb acceptance corrections. This study was possible as the $D^0 \to K^-\pi^+\pi^-\pi^+$ amplitude model was already being developed for a different purpose. The differences between the two scenarios give an estimate of the corrections that should be applied to $R_{K3\pi}$ and $\delta_D^{K3\pi}$. The corresponding differences are calculated to be 0.002 for the coherence factor and 0.7° for the

strong phase difference, compared to the input values of $R_{K3\pi} = 0.43^{+0.17}_{-0.13}$ and $\delta_D^{K3\pi} = \left(128^{+28}_{-17}\right)$. Therefore, the size of the corrections due to the LHCb phase space acceptance are negligible in comparison to the CLEO-c/LHCb uncertainties. Hence no further corrections are made.

A similar study for $D^0 \to \pi^-\pi^+\pi^-\pi^+$ was not possible as a reliable model was unavailable at the time. [1] Therefore, the value of $F_{4\pi}$ is taken directly from the CLEO-c measurement, 0.734 ± 0.028 [24], assuming that any correction would be negligible with respect to the measurement uncertainty as is the case for $R_{K3\pi}$ and $\delta_D^{K3\pi}$.

6.3 Results in terms of r_B, δ_B and γ

The *CP* observables, measured in the *CP* fit and listed in Sec. 5.5, can be used to extract information on the physics parameters of interest: r_B, δ_B and γ, via Eqs. 2.41 - 2.46. The values of the coherence factor κ, estimated in Sec. 6.1, and the parameters $r_D^{K\pi}$, $\delta_D^{K\pi}$, $r_D^{K3\pi}$, $\delta_D^{K3\pi}$, $R_{K3\pi}$ and $F_{4\pi}$, taken from Ref. [24, 28–31], are required as inputs. The set of parameters κ, $r_D^{K\pi}$, $\delta_D^{K\pi}$, $r_D^{K3\pi}$, $\delta_D^{K3\pi}$, $R_{K3\pi}$ and $F_{4\pi}$, here referred to as $\mathbb{P}$, are constrained to the values given in Table 6.2, which is common in the analysis of LHCb measurements. Constraining these parameters, rather than fixing them to their central values, allows the possibility of the *CP* observables providing additional sensitivity[2] for $\mathbb{P}$.

The sensitivity of the data to the set of physics parameters r_B, δ_B and γ is extracted using the χ^2 minimisation procedure described below. The data used are the measured *CP* observables, $\mathbf{x_m}$, along with their combined statistical and systematic covariance matrix V_0. The model, expressed by Eqs. 2.41 - 2.46, is used to calculate *CP* observables, $\mathbf{x}(r_B, \delta_B, \gamma)$, from the set of constrained parameters $\mathbb{P}$ for different values of the physics parameters r_B, δ_B and γ. The χ^2 minimisation

[1] A $D^0 \to \pi^-\pi^+\pi^-\pi^+$ amplitude model based on CLEO-c data has subsequently been published [79].

[2] For the analysis presented in this thesis, the dataset is too small to have an impact on the sensitivity for $\mathbb{P}$.

Fit parameter	Value
κ	0.95 ± 0.06
$r_D^{K\pi}$	0.0591 ± 0.0003
$\delta_D^{K\pi}$	191.8 ± 12.1
$r_D^{K3\pi}$	0.0549 ± 0.0006
$\delta_D^{K3\pi}$	128 ± 28
$R_{K3\pi}$	0.43 ± 0.17
$F_{4\pi}$	0.737 ± 0.028

Table 6.2: Values of the external inputs used as constraints. These values are taken from Ref. [24, 28–30].

procedure is performed, taking correlations into account, with

$$\chi^2(r_B, \delta_B, \gamma) = (\mathbf{x}(r_B, \delta_B, \gamma) - \mathbf{x_m})^T V_0^{-1} (\mathbf{x}(r_B, \delta_B, \gamma) - \mathbf{x_m}) \ . \tag{6.1}$$

The χ^2 is calculated at various points in (r_B, δ_B, γ) space, and the position of the global minimum, $\chi^2_{\rm min}$, represents the point corresponding to the best estimates for the central values of these parameters. The difference between the χ^2 value at each point and that of the global minimum value, $\Delta\chi^2(r_B, \delta_B, \gamma) = \chi^2(r_B, \delta_B, \gamma) - \chi^2_{\rm min}$, can quantify the confidence in the global minimum, and the gradient of $\Delta\chi^2$ in the direction of a given parameter reveals the sensitivity of the data to that parameter. The χ^2 value at the global minimum is 3.0 with 9 degrees of freedom. The confidence level for any pair of parameters is calculated assuming that these are normally distributed, which enables the $\Delta\chi^2 = 2.30,\ 6.18,$ and 11.8 contours to be drawn, corresponding to 68.3%, 95.5%, and 99.7% confidence levels respectively.

Figures 6.5 and 6.6 depict 2D contour plots of r_B versus γ and δ_B versus γ. Figure 6.5 shows the contour plots using the *CP* observables from the two-body modes only and Fig. 6.6 shows the contour plots using the *CP* observables from both the two- and four-body decays. The addition of the four-body modes improves the constraints on the physics parameters and provides additional distinction between the two minima.

The data are consistent with the value of γ indicated by previous measurements [12, 15], $\sim 70°$. The values of r_B, δ_B and γ are determined at the point where the global minimum value of χ^2 is found. The value of r_B is calculated to be

$r_B = 0.113^{+0.017}_{-0.019}$. The parameter δ_B has a measured central value of 43° with a 1σ confidence interval of $[24, 62]°$, and 2σ confidence intervals of $[9, 84]°$ and $[103, 173]°$. The central value of γ is measured to be 41° with a 1σ confidence interval of $[25, 58]°$, and 2σ confidence intervals of $[10, 87]°$ and $[97, 167]°$. No value of γ or δ_B is excluded at the 3σ level. These results provide the current best sensitivity to the hadronic parameters of the B^- decay, r_B and δ_B.

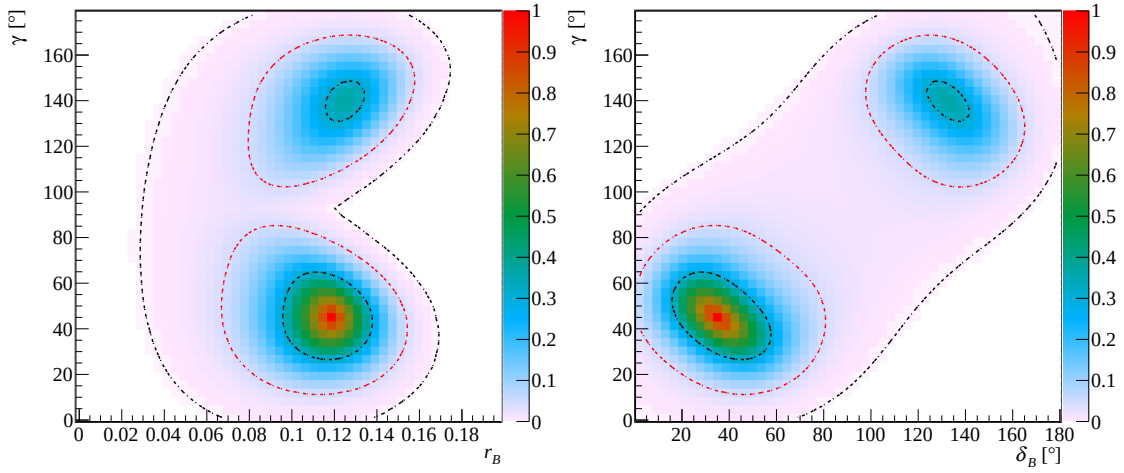

(a) r_B versus γ **(b)** δ_B versus γ

Figure 6.5: Contour plots showing 2D scans of the physics parameters using the two-body D^0 decay modes only. The dashed lines represent the $\Delta\chi^2 = 2.30,\ 6.18,$ and 11.8 contours, corresponding to 68.3%, 95.5%, and 99.7% confidence levels (CL), respectively. The colour scale represents $(1 - \text{CL})$.

6.4 Expected future sensitivity to r_B, δ_B and γ using $B^- \to DK^{*-}$ decays

In this thesis, the $B^- \to DK^{*-}$ mode has shown an increase of three times the yield per unit integrated luminosity from Run 1 to Run 2, mainly due to the increase in centre of mass energy of the pp collisions from 7 and 8 TeV to 13 TeV. As previously stated, the data used in this analysis were collected in 2011 and 2012, forming the Run 1 dataset, and 2015 and 2016, forming part of the Run 2 dataset. The current

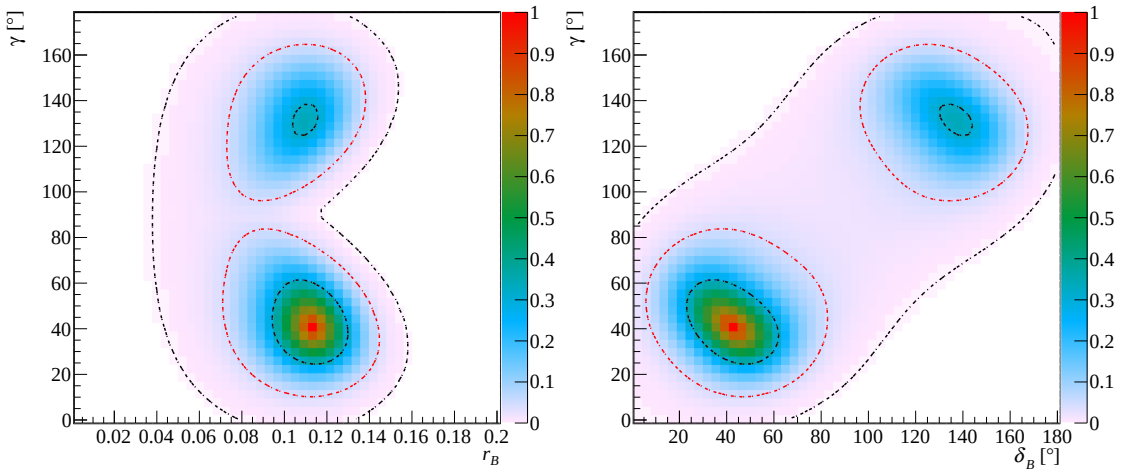

(a) r_B versus γ **(b)** δ_B versus γ

Figure 6.6: Contour plots showing 2D scans of the physics parameters using both the two- and four-body D^0 decay modes. The dashed lines represent the $\Delta\chi^2 = 2.30$, 6.18, and 11.8 contours, corresponding to 68.3%, 95.5%, and 99.7% CL, respectively. The colour scale represents $(1 - \text{CL})$.

running period of the LHC, namely Run 2, is ongoing until the end of 2018. Run 3, the next running period, is planned to take place between 2021 and 2023.

The projected final yields for Run 2 and Run 3 are estimated using the forecasts for the integrated luminosity and expected improvements in the detector performance during these data-taking periods. The projections of the integrated luminosities can be found in Table 6.3. It is assumed that the yield per unit integrated luminosity remains the same for the duration of Run 2 since no significant changes to the detector or running conditions are expected. Between Run 2 and Run 3 the detector will undergo an upgrade to improve detector performance, its trigger and event reconstruction. This will include moving to a fully software-based trigger [80] and the rebuilding of many detector components, which will allow the experiment to run at an instantaneous luminosity of 2×10^{33} cm^{-2}s^{-1}, a five-fold increase on the current conditions [80]. Therefore, Run 3 is expected to produce a minimum of 5 fb^{-1} per year for three years [80]. Additionally, the centre of mass energy is expected to increase to 14 TeV. The upgrade to a fully software-based trigger also improves the trigger efficiencies for the fully hadronic modes by about a factor of

Year	Integrated Luminosity	$B^- \to D(K^-\pi^+)K^{*-}$ yield	Yield per fb^{-1}
Run 1	3 fb^{-1}	725	242
Run 2 (up to 2016)	1.8 fb^{-1}	1390	771
Run 2 (after 2016)	**3.2 fb^{-1}**	**2466**	**771**
Run 3	**15 fb^{-1}**	**23130**	**1542**

Table 6.3: Yields and projected yields for the data-taking periods of the LHC. The entries in bold are projected yields, whereas the other entries refer to data used in this thesis. Projected results are justified in the text, with information taken from Ref. [80].

two compared to Run 1 [80]. Overall, yields of B meson decay modes in Run 3 are expected to increase by a factor of ∼32 compared to Run 1, even before any potential improvements in the analysis procedure. The result of these assumptions are shown in the projected yield estimates in Table 6.3.

Using the results of Table 6.3, the projected sensitivity to the physics parameters r_B, δ_B and γ are estimated, assuming conservatively that the systematic uncertainties remain the same. Figure 6.7 gives the projected results at the end of Run 2 as 2D contour plots of r_B versus γ and δ_B versus γ. The equivalent plots for the end of Run 3 are shown in Fig. 6.8.

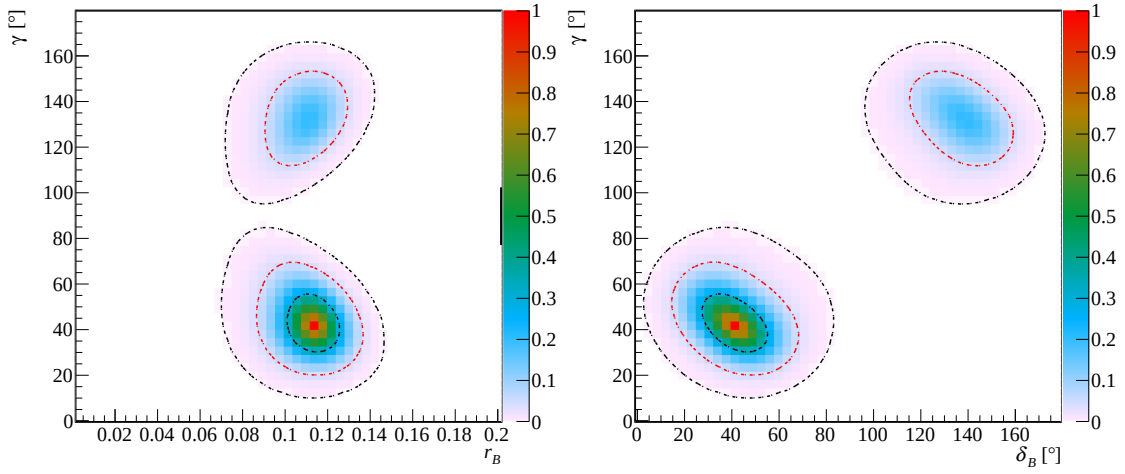

(a) r_B versus γ **(b)** δ_B versus γ

Figure 6.7: Contour plots showing projected 2D scans of the physics parameters measured in $B^- \to DK^{*-}$ decays at the end of full Run 2 data-taking, assuming the central values remain the same. The dashed lines represent the $\Delta\chi^2 = 2.30,\ 6.18,$ and 11.8 contours, corresponding to 68.3%, 95.5%, and 99.7% CL, respectively. The colour scale represents $(1 - \text{CL})$.

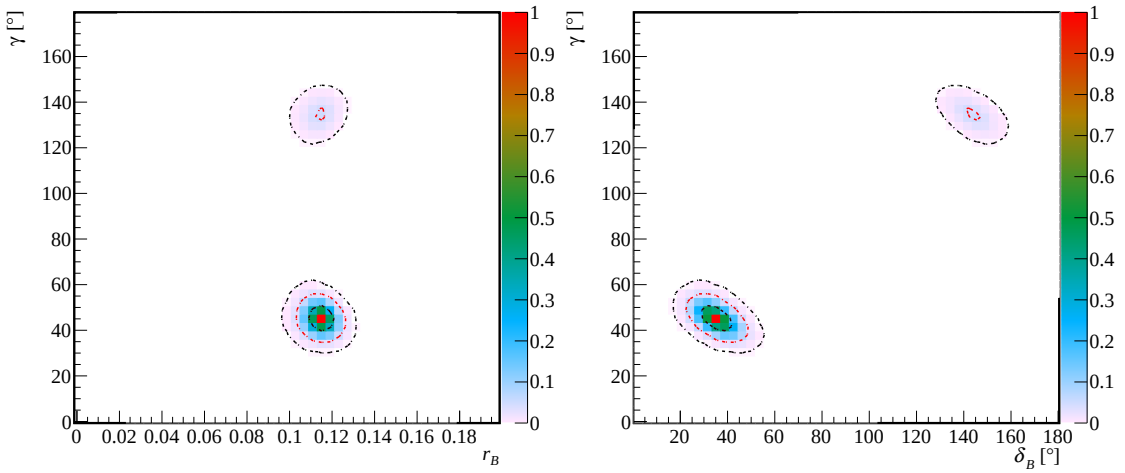

(a) r_B versus γ **(b)** δ_B versus γ

Figure 6.8: Contour plots showing projected 2D scans of the physics parameters measured in $B^- \to DK^{*-}$ decays at the end of Run 3, assuming the central values remain the same. The dashed lines represent the $\Delta\chi^2 = 2.30,\ 6.18,$ and 11.8 contours, corresponding to 68.3%, 95.5%, and 99.7% CL, respectively. The colour scale represents $(1 - \text{CL})$.

It can be seen that the sensitivity of r_B, δ_B and γ continues to improve significantly with more data since the uncertainties are dominated by statistical uncertainty; therefore the $B^- \to DK^{*-}$ channel will continue to benefit from the increased dataset in Run 3 and beyond. At the end of Run 3 the uncertainty on γ, from $B^- \to DK^{*-}$ decays as investigated in this thesis, is expected to reduce to about 5°. Uncertainties in the measurements of the hadronic parameters in $B^- \to DK^{*-}$ decays, r_B and δ_B, will also reduce significantly to about 0.006 and 7° respectively. However, Fig. 6.8 demonstrates that even with these additional data, multiple solutions will exist. This problem of multiple solutions can be resolved by investigating alternative decays of the D^0 meson via the GGSZ method [81], which involves analysing D^0 decays to $K^0_S\pi^+\pi^-$ and $K^0_S K^+ K^-$ final states [17, 82].

This thesis has presented the first $B^- \to DK^{*-}$ measurement at LHCb and one of the first *CP* violation measurements at LHCb with Run 2 data. Additionally, the current world's best sensitivity to the hadronic parameters of the B^- decay, r_B and δ_B, has been reported. There has been significant growth in understanding and interest with respect to amplitude analyses of B decays. Independent information

such as the measurements presented in this thesis, particularly on phases, is a significant asset to developing amplitude models. Further studies into $B^- \to DK^{*-}$ decays, subsequently leading to the development of an amplitude model for $B^- \to DK^0_S\pi^-$ decays, would provide a greater understanding of resonant structures present in the $K^0_S\pi^-$ system. Such an investigation would benefit greatly from the parameters r_B and δ_B as constraints in the model, which can only be provided by studies of $B^- \to DK^{*-}$ decays as presented in this thesis.

The suite of γ measurements is dominated, and will continue to be dominated, by $B^- \to DK^-$ measurements [83]. However, the analysis of the $B^- \to DK^-$ mode requires the modelling of several challenging backgrounds, most notably the misidentification background from $B^- \to D\pi^-$ decays and also partially reconstructed background, which both overlap with the signal region. Therefore, all $B^- \to DK^-$ measurements are accompanied by systematic uncertainties relating to these sources. Expanding the field of γ-sensitive measurements to include other B^- decays, namely $B^- \to DK^{*-}$ decays, which contains relatively few challenging background components, provides an invaluable cross-check for the γ measurements made with $B^- \to DK^-$ decays. Hence future measurements of $B^- \to DK^{*-}$ decay modes are anticipated with significant interest.

The global strategy to measure γ in a wide variety of B and D decay modes is central to achieving the best precision of this parameter. The latest combination of results from a variety of γ-sensitive analyses at LHCb gives a measurement of $\left(76.8^{+5.1}_{-5.7}\right)^\circ$ [83], which includes preliminary results from the work in this thesis. Different methods have been developed to investigate a range of decays modes of the D^0 meson using the $B^- \to DK^-$ channel. The work presented in this thesis leads the way for a completely new, though physically similar, $B^- \to DK^{*-}$ channel to be exploited using the many different D decay modes developed for the $B^- \to DK^-$ channel. This work opens the door for a whole new range of γ-sensitive analyses to be developed. Furthermore, the work in this thesis can be further expanded by considering $B^- \to DK^{*-}$ decays, where the K^{*-} meson is reconstructed as $K^-\pi^0$. The inclusion of this alternative mode would result in a

gain in γ-sensitivity from the additional data. However, as mentioned previously, this mode is significantly more difficult to reconstruct.

Measurements of γ will continue in the future, using as much data and as many B and D modes as possible, in order to reduce the statistical uncertainty. The expected sensitivity of γ at the end of Run 2 is 4° [84]. The upgrade of Run 3 and beyond is estimated to provide a luminosity of 50 fb^{-1} by the end of 2030, and achieve a significant increase in signal efficiency for B meson decays, resulting in a predicted sensitivity to γ of 0.9° [84]. Additionally, the Belle II experiment, which is expecting to collect a data sample corresponding to an integrated luminosity of 50 ab^{-1} between 2018 and 2026, predicts a determination of γ to 1.6° [85]. The $B^- \to DK^{*-}(K^0_S\pi^-)$ decay mode will have a relatively higher power for measuring γ at Belle II as the K^0_S reconstruction efficiency will be much improved compared to LHCb. By continuing to measure γ in many different B and D modes, benefiting from the $B^- \to DK^{*-}$ channel introduced in this thesis and making full use of the increasing amount of data available, the Standard Model will be probed to unprecedented levels of precision. Through these multitude of measurements, it is hoped that signs of New Physics will begin to emerge.

7 Conclusion

A study of *CP* violation in the $B^- \to DK^{*-}$ mode has been performed, with the D meson decaying to $K^+\pi^-$, K^+K^-, $\pi^+\pi^-$, $K^+\pi^-\pi^+\pi^-$ and $\pi^+\pi^-\pi^+\pi^-$ final states. The data analysed in this study were collected in proton-proton collisions by the LHCb detector at the Large Hadron Collider (LHC) between 2011 and 2016. The study used $1\,\text{fb}^{-1}$ and $2\,\text{fb}^{-1}$ of data at centre of mass energies of $\sqrt{s} = 7\,\text{TeV}$ and $8\,\text{TeV}$ collected in 2011 and 2012 respectively, and $1.8\,\text{fb}^{-1}$ at $\sqrt{s} = 13\,\text{TeV}$ collected in 2015 and 2016.

The world's most precise measurement of *CP* violation in $B^- \to DK^{*-}$ decays has been made, using approximately 3660 signal events across all D^0 decay modes. The major results from this analysis are the *CP* observables relating to the yield ratios and asymmetries, which are:

$$
\begin{aligned}
A_{K\pi} &= -0.004 \pm 0.023 \pm 0.008 & A_{K\pi\pi\pi} &= -0.013 \pm 0.031 \pm 0.009 \\
A_{KK} &= 0.06 \pm 0.07 \pm 0.01 & A_{\pi\pi\pi\pi} &= 0.02 \pm 0.11 \pm 0.01 \\
A_{\pi\pi} &= 0.15 \pm 0.13 \pm 0.02 & R_{\pi\pi\pi\pi} &= 1.08 \pm 0.13 \pm 0.03 \\
R_{KK} &= 1.22 \pm 0.09 \pm 0.01 & R^{+}_{K\pi\pi\pi} &= 0.016 \pm 0.007 \pm 0.003 \\
R_{\pi\pi} &= 1.08 \pm 0.14 \pm 0.03 & R^{-}_{K\pi\pi\pi} &= 0.006 \pm 0.006 \pm 0.004 \\
R^{+}_{K\pi} &= 0.020 \pm 0.006 \pm 0.001 & & \\
R^{-}_{K\pi} &= 0.002 \pm 0.004 \pm 0.001 & &
\end{aligned}
$$

where the first uncertainty is statistical and the second is systematic. These measurements are found to be consistent with and more precise than the previous measurements from BaBar [44]. The first evidence of the two-body ADS mode, $B^- \to D(\pi^- K^+)K^{*-}$, was obtained with a statistical significance of 4.2σ. The sensitivity to the unitary triangle angle γ was extracted, obtaining a central value of 41° with a 1σ confidence interval of $[25, 58]^\circ$, and 2σ confidence intervals of $[10, 87]^\circ$ and $[97, 167]^\circ$. Also, the current best sensitivity to the hadronic parameters of the B^- decay, namely r_B and δ_B, has been presented.

The work presented in this thesis provides a significant contribution to the measurement of γ, representing a parameterisation of *CP* violation in the Standard Model. Inconsistencies between direct and indirect measurements of γ could indicate new *CP* violation effects beyond the Standard Model and, if found, could give an insight into the flavour structure of New Physics. This would ultimately help generate a deeper understanding of the large matter-antimatter asymmetry observed in the Universe.

Appendices

A

Distributions of BDT input variables

Figures A.1 and A.2 show the distributions of the four-body BDT input variables in the signal and background training samples.

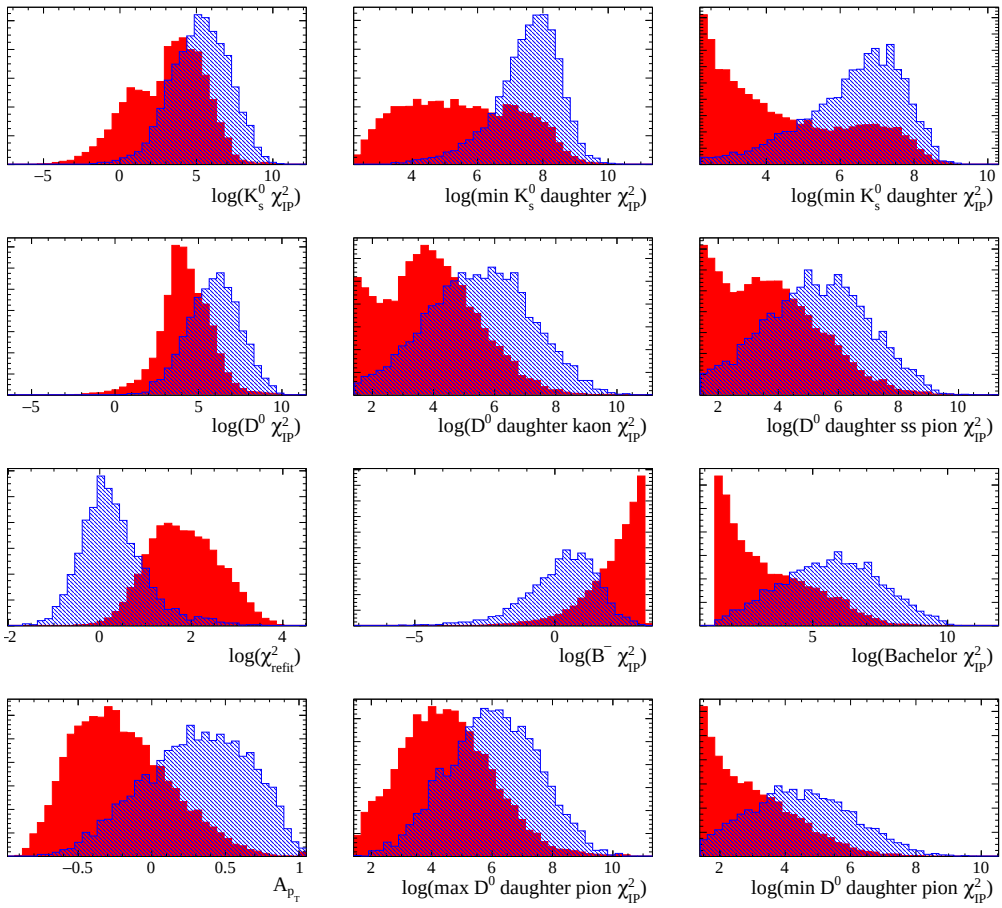

Figure A.1: Distributions of the input variables using the signal (blue) and background (red) training samples for the four-body LL BDT. The variable A_{p_T} represents the p_T asymmetry as defined in Eq. 4.4 and "max (min) K^0_S daughter χ^2_{IP}" refers to the χ^2_{IP} of the K^0_S daughter which has the largest (smallest) χ^2_{IP}. The particle name "D daughter ss" refers to the pion from the D^0 meson which has the same sign as the kaon. All distributions have been normalised to unity in order to easily compare their shape, therefore the vertical axis is not labelled as it is not of interest here.

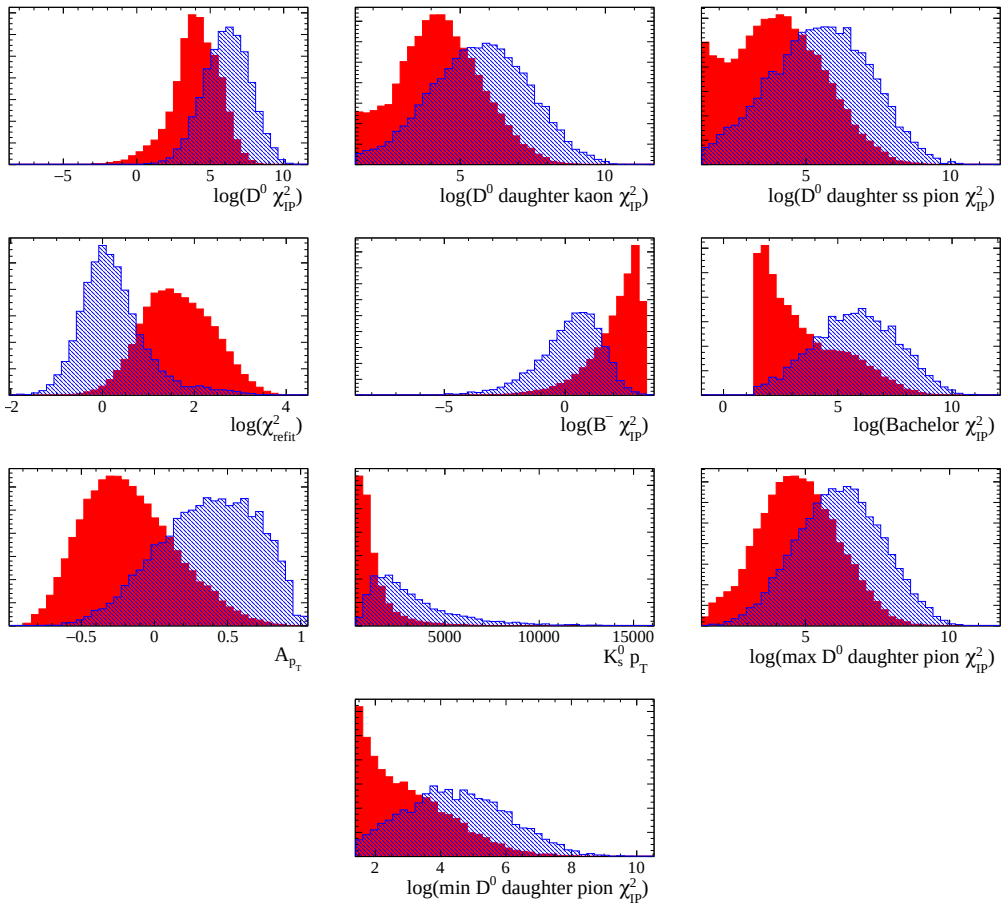

Figure A.2: Distributions of the input variables using the signal (blue) and background (red) training samples for the four-body DD BDT. The variable $A_{p_{\mathrm{T}}}$ represents the p_{T} asymmetry as defined in Eq. 4.4. The particle name "D daughter ss" refers to the pion from the D^0 meson which has the same sign as the kaon. All distributions have been normalised to unity in order to easily compare their shape, therefore the vertical axis is not labelled as it is not of interest here.

References

[1] R. Aaij et al. "Measurement of *CP* observables in $B^{\pm} \to DK^{*\pm}$ decays using two- and four-body D-meson final states". In: *JHEP* 11 (2017), p. 156. arXiv: 1709.05855 [hep-ex].

[2] D. Hanneke, S. Fogwell, and G. Gabrielse. "New Measurement of the Electron Magnetic Moment and the Fine Structure Constant". In: *Phys. Rev. Lett.* 100 (12 Mar. 2008), p. 120801. URL: https://link.aps.org/doi/10.1103/PhysRevLett.100.120801.

[3] R. Aaij et al. "Observation of $J/\psi p$ Resonances Consistent with Pentaquark States in $\Lambda_b^0 \to J/\psi K^- p$ Decays". In: *Phys. Rev. Lett.* 115 (7 Aug. 2015), p. 072001. URL: https://link.aps.org/doi/10.1103/PhysRevLett.115.072001.

[4] M. Ablikim et al. "Observation of a Charged Charmoniumlike Structure in $e^+e^- \to \pi^+\pi^- J/\psi$ at $\sqrt{s}$=4.26 GeV". In: *Phys. Rev. Lett.* 110 (25 June 2013), p. 252001. URL: https://link.aps.org/doi/10.1103/PhysRevLett.110.252001.

[5] R. Aaij et al. "Observation of the Resonant Character of the $Z(4430)^-$ State". In: *Phys. Rev. Lett.* 112 (22 June 2014), p. 222002. URL: https://link.aps.org/doi/10.1103/PhysRevLett.112.222002.

[6] C. L. Bennett et al. "Nine-year Wilkinson Microwave Anisotropy Probe (WMAP) Observations: Final Maps and Results". In: *The Astrophysical Journal Supplement Series* 208.2 (2013), p. 20. URL: http://stacks.iop.org/0067-0049/208/i=2/a=20.

[7] Andrei D Sakharov. "Violation of CP invariance, C asymmetry, and baryon asymmetry of the universe". In: *Soviet Physics Uspekhi* 34.5 (1991), p. 392. URL: http://stacks.iop.org/0038-5670/34/i=5/a=A08.

[8] M.B. Gavela et al. "Standard model CP-violation and baryon asymmetry (I). Zero temperature". In: *Nuclear Physics B* 430.2 (1994), pp. 345–381. URL: http://www.sciencedirect.com/science/article/pii/0550321394004099.

[9] Antonio Masiero and Oscar Vives. "NEW PHYSICS IN CP VIOLATION EXPERIMENTS". In: *Annual Review of Nuclear and Particle Science* 51.1 (2001), pp. 161–187. eprint: https://doi.org/10.1146/annurev.nucl.51.101701.132338. URL: https://doi.org/10.1146/annurev.nucl.51.101701.132338.

[10] C. Patrignani et al. "Review of particle physics". In: *Chin. Phys.* C40 (2016), p. 100001.

[11] C. Jarlskog. "Commutator of the quark mass matrices in the standard electroweak model and a measure of maximal *CP* nonconservation". In: *Phys. Rev. Lett.* 55 (10 Sept. 1985), pp. 1039–1042. URL: https://link.aps.org/doi/10.1103/PhysRevLett.55.1039.

[12] R. Aaij et al. "Measurement of the CKM angle γ from a combination of LHCb results". In: *JHEP* 12 (2016), p. 087. arXiv: 1611.03076 [hep-ex].

[13] J. P. Lees et al. "Observation of direct CP violation in the measurement of the Cabibbo-Kobayashi-Maskawa angle γ with $B^{\pm} \to D^{(*)}K^{(*)\pm}$ decays". In: *Phys. Rev. D* 87 (5 Mar. 2013), p. 052015. URL: https://link.aps.org/doi/10.1103/PhysRevD.87.052015.

[14] Karim Trabelsi et al. "Study of direct CP in charmed B decays and measurement of the CKM angle gamma at Belle". In: *arXiv preprint arXiv:1301.2033* (2013).

[15] J. Charles et al. "CP violation and the CKM matrix: Assessing the impact of the asymmetric B factories". In: *Eur.Phys.J.* C41 (2005). updated results and plots available at: http://ckmfitter.in2p3.fr, pp. 1–131. arXiv: hep-ph/0406184 [hep-ph].

[16] R. Aaij et al. "Measurement of *CP* observables in $B^{\pm} \to DK^{\pm}$ and $B^{\pm} \to D\pi^{\pm}$ with two- and four-body D decays". In: *Phys. Lett.* B760 (2016), p. 117. arXiv: 1603.08993 [hep-ex].

[17] R. Aaij et al. "Measurement of the CKM angle γ using $B^{\pm} \to DK^{\pm}$ with $D \to K^0_S\pi^+\pi^-$, $K^0_S K^+K^-$ decays". In: *JHEP* 10 (2014), p. 097. arXiv: 1408.2748 [hep-ex].

[18] R. Aaij et al. "A study of *CP* violation in $B^{\mp} \to Dh^{\mp}$ ($h = K, \pi$) with the modes $D \to K^{\mp}\pi^{\pm}\pi^0$, $D \to \pi^+\pi^-\pi^0$ and $D \to K^+K^-\pi^0$". In: *Phys. Rev.* D91 (2015), p. 112014. arXiv: 1504.05442 [hep-ex].

[19] Wei Wang. "*CP* violation effects on the measurement of the Cabibbo-Kobayashi-Maskawa angle γ from $B \to DK$". In: *Phys. Rev. Lett.* 110 (6 Feb. 2013), p. 061802. arXiv: 1211.4539. URL: https://link.aps.org/doi/10.1103/PhysRevLett.110.061802.

[20] Matteo Rama. "Effect of $D - \bar{D}$ mixing in the extraction of γ with $B^- \to D^0K^-$ and $B^- \to D^0\pi^-$ decays". In: *Phys. Rev.* D89 (1 Jan. 2014), p. 014021. arXiv: 1307.4384. URL: https://link.aps.org/doi/10.1103/PhysRevD.89.014021.

[21] Michael Gronau and David London. "How to determine all the angles of the unitarity triangle from $B^0_d \to DK_S$ and $B^0_s \to D\phi$". In: *Phys. Lett.* B253 (1991), pp. 483–488. URL: http://www.sciencedirect.com/science/article/pii/037026939191756L.

[22] Michael Gronau and Daniel Wyler. "On determining a weak phase from charged B decay asymmetries ". In: *Phys. Lett.* B265 (1991), pp. 172–176. URL: http://www.sciencedirect.com/science/article/pii/037026939190034N.

[23] M. Nayak et al. "First determination of the CP content of $D \to \pi^+\pi^-\pi^0$ and $D \to K^+K^-\pi^0$". In: *Physics Letters B* 740 (2015), pp. 1–7. URL: http://www.sciencedirect.com/science/article/pii/S0370269314008247.

[24] S. Malde et al. "First determination of the CP content of $D \to \pi^+\pi^-\pi^+\pi^-$ and updated determination of the CP contents of $D \to \pi^+\pi^-\pi^0$ and $D \to K^+K^-\pi^0$". In: *Phys. Lett.* B747 (2015), pp. 9–17. arXiv: 1504.05878. URL: http://www.sciencedirect.com/science/article/pii/S0370269315003809.

[25] David Atwood, Isard Dunietz, and Amarjit Soni. "Enhanced *CP* violation with $B \to KD^0(\overline{D}^0)$ modes and extraction of the Cabibbo-Kobayashi-Maskawa angle γ". In: *Phys. Rev. Lett.* 78 (17 Apr. 1997), pp. 3257–3260. URL: http://link.aps.org/doi/10.1103/PhysRevLett.78.3257.

[26] David Atwood, Isard Dunietz, and Amarjit Soni. "Improved methods for observing *CP* violation in $B^\pm \to KD$ and measuring the CKM phase γ". In: *Phys. Rev.* D63 (3 Jan. 2001), p. 036005. arXiv: hep-ph/0008090. URL: http://link.aps.org/doi/10.1103/PhysRevD.63.036005.

[27] D. M. Asner et al. "Updated measurement of the strong phase in $D^0 \to K^+\pi^-$ decay using quantum correlations in $e^+e^- \to D^0\overline{D}^0$ at CLEO". In: *Phys. Rev. D* 86 (11 Dec. 2012), p. 112001. URL: https://link.aps.org/doi/10.1103/PhysRevD.86.112001.

[28] Y. Amhis et al. "Averages of b-hadron, c-hadron, and τ-lepton properties as of summer 2016". In: (2016). updated results and plots available at http://www.slac.stanford.edu/xorg/hflav/. arXiv: 1612.07233 [hep-ex].

[29] T. Evans et al. "Improved determination of the $D \to K^+\pi^-\pi^+\pi^-$ coherence factor and associated hadronic parameters from a combination of $e^+e^- \to \Upsilon(3770) \to c\bar{c}$ and $pp \to c\bar{c}X$ data". In: *Phys. Lett.* B757 (2016), pp. 520–527. arXiv: 1602.07430. URL: http://www.sciencedirect.com/science/article/pii/S0370269316301101.

[30] T. Evans et al. "Corrigendum to: "Improved determination of the $D \to K^+\pi^-\pi^+\pi^-$ coherence factor and associated hadronic parameters from a combination of $e^+e^- \to \Upsilon(3770) \to c\bar{c}$ and $pp \to c\bar{c}X$ data" [Phys. Lett. B 757 (2016) 520]". In: *Physics Letters B* 765 (2017), pp. 402–403. URL: http://www.sciencedirect.com/science/article/pii/S0370269316306840.

[31] R. Aaij et al. "First observation of $D^0 - \overline{D}^0$ oscillations in $D^0 \to K^+\pi^+\pi^-\pi^-$ decays and a measurement of the associated coherence parameters". In: *Phys. Rev. Lett.* 116 (2016), p. 241801. arXiv: 1602.07224 [hep-ex].

[32] R. Aaij et al. "Measurement of *CP* observables in $B^\pm \to D^{(*)}K^\pm$ and $B^\pm \to D^{(*)}\pi^\pm$ decays". In: *Phys. Lett.* B777 (2017), p. 16. arXiv: 1708.06370 [hep-ex].

[33] R. Aaij et al. "A study of *CP* violation in $B^\pm \to DK^\pm$ and $B^\pm \to D\pi^\pm$ decays with $D \to K^0_S K^\pm\pi^\mp$ final states". In: *Phys. Lett.* B733 (2014), p. 36. arXiv: 1402.2982 [hep-ex].

[34] R. Aaij et al. "Model-independent measurement of the CKM angle γ using $B^0 \to DK^{*0}$ decays with $D \to K^0_S\pi^+\pi^-$ and $K^0_S K^+K^-$". In: *JHEP* 06 (2016), p. 131. arXiv: 1604.01525 [hep-ex].

[35] R. Aaij et al. "Measurement of *CP* asymmetry in $B^0_s \to D^\mp_s K^\pm$ decays". In: *JHEP* 11 (2014), p. 060. arXiv: 1407.6127 [hep-ex].

[36] P. del Amo Sanchez et al. "Measurement of CP observables in $B^{\pm} \to D_{CP}K^{\pm}$ decays and constraints on the CKM angle γ". In: *Phys. Rev.* D82 (2010), p. 072004. arXiv: 1007.0504 [hep-ex].

[37] P. del Amo Sanchez et al. "Search for $b \to u$ transitions in $B^- \to DK^-$ and $B^- \to D^*K^-$ decays". In: *Phys. Rev.* D82 (2010), p. 072006. arXiv: 1006.4241 [hep-ex].

[38] J.P. Lees et al. "Observation of direct CP violation in the measurement of the Cabibbo-Kobayashi-Maskawa angle gamma with $B^{\pm} \to D^{(*)}K^{(*)\pm}$ decays". In: *Phys.Rev.* D87.5 (2013), p. 052015. arXiv: 1301.1029 [hep-ex].

[39] B. Aubert et al. "Improved measurement of the CKM angle γ in $B^{\mp} \to D^{(*)}K^{(*)\mp}$ decays with a Dalitz plot analysis of D decays to $K^0_S\pi^+\pi^-$ and $K^0_SK^+K^-$". In: *Phys. Rev.* D78 (3 Aug. 2008), p. 034023. arXiv: 0804.2089. URL: http://link.aps.org/doi/10.1103/PhysRevD.78.034023.

[40] B. Aubert et al. "Constraints on the CKM angle γ in $B^0 \to \overline{D}^0K^{*0}$ and $B^0 \to D^0K^{*0}$ from a Dalitz analysis of D^0 and $\overline{D}^0$ decays to $K_S\pi^+\pi^-$". In: *Phys. Rev. D* 79 (7 Apr. 2009), p. 072003. URL: https://link.aps.org/doi/10.1103/PhysRevD.79.072003.

[41] K. Abe et al. "Study of $B^{\pm} \to D_{CP}K^{\pm}$ and $D^*_{CP}K^{\pm}$ decays". In: *Phys. Rev.* D73 (2006), p. 051106. arXiv: hep-ex/0601032.

[42] Y. Horii et al. "Evidence for the suppressed decay $B^- \to DK^-, D \to K^+\pi^-$". In: *Phys. Rev. Lett.* 106 (2011), p. 231803. arXiv: 1103.5951 [hep-ex].

[43] A. Poluektov et al. "Measurement of ϕ_3 with a Dalitz plot analysis of $B^+ \to D^{(*)}K^{(*)+}$ decay". In: *Phys. Rev.* D73 (11 June 2006), p. 112009. eprint: hep-ex/0604054. URL: http://link.aps.org/doi/10.1103/PhysRevD.73.112009.

[44] B. Aubert et al. "Measurement of *CP* violation observables and parameters for the decays $B^{\pm} \to DK^{*\pm}$". In: *Phys. Rev.* D80 (9 Nov. 2009), p. 092001. arXiv: 0909.3981. URL: http://link.aps.org/doi/10.1103/PhysRevD.80.092001.

[45] A. A. Alves Jr. et al. "The LHCb detector at the LHC". In: *JINST* 3 (2008), S08005.

[46] R. Aaij et al. "LHCb detector performance". In: *Int. J. Mod. Phys.* A30 (2015), p. 1530022. arXiv: 1412.6352 [hep-ex].

[47] R. Aaij et al. "Performance of the LHCb Vertex Locator". In: *JINST* 9 (2014), P09007. arXiv: 1405.7808 [physics.ins-det].

[48] The LHCb Collaboration et al. "The LHCb Detector at the LHC". In: *Journal of Instrumentation* 3.08 (2008), S08005. URL: http://stacks.iop.org/1748-0221/3/i=08/a=S08005.

[49] R. Aaij et al. "Measurement of the track reconstruction efficiency at LHCb". In: *JINST* 10 (2015), P02007. arXiv: 1408.1251 [hep-ex].

[50] M. Adinolfi et al. "Performance of the LHCb RICH detector at the LHC". In: *Eur. Phys. J.* C73 (2013), p. 2431. arXiv: 1211.6759 [physics.ins-det].

[51] Antonis Papanestis and Carmelo D'Ambrosio. *Performance of the LHCb RICH detectors during the LHC Run II. Performance of the LHCb RICH detectors during the LHC Run II.* Tech. rep. LHCB-PUB-2017-012. CERN-LHCb-PUB-2017-012. Updated authors' details and DOI. Geneva: CERN, Mar. 2017. URL: https://cds.cern.ch/record/2255885.

[52] R. Aaij et al. "Performance of the LHCb calorimeters". In: (2014). in preparation.

[53] Yu. Guz. "The LHCb Calorimeter system: design, performance and upgrade". In: *Journal of Instrumentation* 12.07 (2017), p. C07024. URL: http://stacks.iop.org/1748-0221/12/i=07/a=C07024.

[54] F. Archilli et al. "Performance of the muon identification at LHCb". In: *JINST* 8 (2013), P10020. arXiv: 1306.0249 [physics.ins-det].

[55] A A Alves Jr. et al. "Performance of the LHCb muon system". In: *JINST* 8 (2013), P02022. arXiv: 1211.1346 [physics.ins-det].

[56] R. Aaij et al. "The LHCb trigger and its performance in 2011". In: *JINST* 8 (2013), P04022. arXiv: 1211.3055 [hep-ex].

[57] T Head. "The LHCb trigger system". In: *Journal of Instrumentation* 9.09 (2014), p. C09015. URL: http://stacks.iop.org/1748-0221/9/i=09/a=C09015.

[58] M Clemencic et al. "The LHCb simulation application, Gauss: Design, evolution and experience". In: *J. Phys. Conf. Ser.* 331 (2011), p. 032023.

[59] R Antunes-Nobrega et al. *LHCb computing: Technical Design Report.* Technical Design Report LHCb. Submitted on 11 May 2005. Geneva: CERN, 2005. URL: https://cds.cern.ch/record/835156.

[60] Torbjörn Sjöstrand, Stephen Mrenna, and Peter" Skands. "A brief introduction to PYTHIA 8.1". In: *Comput. Phys. Commun.* 178 (2008), pp. 852–867. arXiv: 0710.3820 [hep-ph].

[61] D. J. Lange. "The EvtGen particle decay simulation package". In: *Nucl. Instrum. Meth.* A462 (2001), pp. 152–155.

[62] Piotr Golonka and Zbigniew Was. "PHOTOS Monte Carlo: A precision tool for QED corrections in Z and W decays". In: *Eur. Phys. J.* C45 (2006), pp. 97–107. arXiv: hep-ph/0506026 [hep-ph].

[63] Wouter D. Hulsbergen. "Decay chain fitting with a Kalman filter". In: *Nucl. Instrum. Meth.* A552 (2005), pp. 566–575. arXiv: physics/0503191 [physics].

[64] F. Dettori. "Production measurements at LHCb with the first data". In: (2009). arXiv: 0909.5596.

[65] L. Breiman et al. *Classification and regression trees.* Belmont, California, USA: Wadsworth international group, 1984.

[66] Andreas Hoecker et al. "TMVA: Toolkit for Multivariate Data Analysis". In: *PoS* ACAT (2017), p. 040. arXiv: physics/0703039.

[67] Louis Lyons, Wade W.M. Allison, and Jaime Pañella Comellas. "Maximum likelihood or extended maximum likelihood? An example from high energy physics". In: *Nuclear Instruments and Methods in Physics Research Section A: Accelerators, Spectrometers, Detectors and Associated Equipment* 245.2 (1986), pp. 530–534. URL: http://www.sciencedirect.com/science/article/pii/0168900286912933.

[68] Roger Barlow. "Extended maximum likelihood". In: *Nuclear Instruments and Methods in Physics Research Section A: Accelerators, Spectrometers, Detectors and Associated Equipment* 297.3 (1990), pp. 496–506. URL: http://www.sciencedirect.com/science/article/pii/0168900290913348.

[69] M. Fisher and D. Sachs. "An Object-Oriented Minimization Package for HEP". In: *CHEP03 Computers in High Energy Physics, San Diego, CA* (2003). arXiv: hep-ph/0306054. URL: http://lss.fnal.gov/archive/2003/conf/Conf-03-160.pdf.

[70] Tomasz Skwarnicki. "A study of the radiative cascade transitions between the Upsilon-prime and Upsilon resonances". DESY-F31-86-02. PhD thesis. Institute of Nuclear Physics, Krakow, 1986.

[71] R. Aaij et al. "Measurement of the $B^{\pm}$ production asymmetry and the *CP* asymmetry in $B^{\pm} \to J/\psi K^{\pm}$ decays". In: *Phys. Rev.* D95 (2017), p. 052005. arXiv: 1701.05501 [hep-ex].

[72] R Aaij et al. "Measurement of the D_S^+ - D_S^- production asymmetry in 7 TeV *pp* collisions". In: *Phys. Lett.* B713 (2012), p. 186.

[73] R Aaij et al. "Measurement of CP asymmetry in $D^0 \to K^-K^+$ and $D^0 \to \pi^-\pi^-$ decays". In: *Journal of High Energy Physics* 2014.7 (2014), p. 41. arXiv: 1405.2797. URL: http://dx.doi.org/10.1007/JHEP07(2014)041.

[74] N. L. Johnson. "Systems of frequency curves derived from the first law of Laplace". In: (5 1954), pp. 283–291.

[75] S. S. Wilks. "The large-sample distribution of the likelihood ratio for testing composite hypotheses". In: *Ann. Math.Stat.* 9 (1938), pp. 60–62.

[76] D. Aston et al. "A study of $K^-\pi^+$ scattering in the reaction $K^-p \to K^-\pi^+n$ at 11 GeV/c". In: *Nucl. Phys.* B296 (1988), pp. 493–526. URL: http://www.sciencedirect.com/science/article/pii/0550321388900284.

[77] G. Breit and E. Wigner. "Capture of Slow Neutrons". In: *Phys. Rev.* 49 (7 Apr. 1936), pp. 519–531. URL: https://link.aps.org/doi/10.1103/PhysRev.49.519.

[78] R. Aaij et al. "Studies of the resonance structure in $D^0 \to K^{\mp}\pi^{\pm}\pi^+\pi^-$ decays". In: (2017). submitted to EPJC. arXiv: 1712.08609 [hep-ex].

[79] P. d'Argent et al. "Amplitude analyses of $D^0 \to \pi^+\pi^-\pi^+\pi^-$ and $D^0 \to K^+K^-\pi^+\pi^-$ decays". In: *Journal of High Energy Physics* 2017.5 (May 29, 2017), p. 143. URL: https://doi.org/10.1007/JHEP05(2017)143.

[80] *LHCb Trigger and Online Upgrade Technical Design Report*. Tech. rep. CERN-LHCC-2014-016. LHCB-TDR-016. May 2014. URL: https://cds.cern.ch/record/1701361.

[81] Anjan Giri et al. "Determining γ using $B^{\pm} \to DK^{\pm}$ with multibody D decays". In: *Phys. Rev. D* 68 (5 Sept. 2003), p. 054018. URL: https://link.aps.org/doi/10.1103/PhysRevD.68.054018.

[82] R. Aaij et al. "A model-independent Dalitz plot analysis of $B^{\pm} \to DK^{\pm}$ with $D \to K^0_S h^+h^-$ ($h = \pi, K$) decays and constraints on the CKM angle γ". In: *Phys. Lett.* B718 (2012), pp. 43–55. arXiv: 1209.5869 [hep-ex].

[83] *Measurement of the CKM angle γ from a combination of $B \to DK$ analyses.* https://cds.cern.ch/record/2275866/files/LHCb-CONF-2017-004.pdf. Jul 2017.

[84] R. Aaij *et al.*, and A. Bharucha et al. “Implications of LHCb measurements and future prospects”. In: *Eur. Phys. J.* C73 (2013), p. 2373. arXiv: 1208.3355 [hep-ex].

[85] Hulya Atmacan. “Measurement of the gamma CKM angle with Belle II”. In: *PANIC2017* (Sept. 2017). 15 + 5 min.